



**A University of Sussex PhD thesis**

Available online via Sussex Research Online:

<http://sro.sussex.ac.uk/>

This thesis is protected by copyright which belongs to the author.

This thesis cannot be reproduced or quoted extensively from without first obtaining permission in writing from the Author

The content must not be changed in any way or sold commercially in any format or medium without the formal permission of the Author

When referring to this work, full bibliographic details including the author, title, awarding institution and date of the thesis must be given

Please visit Sussex Research Online for more information and further details



**Improved sensitivity to  $\Delta m_{21}^2$  by  
classification of the  $^{13}\text{C}(\alpha, n)^{16}\text{O}$   
background in the SNO+ antineutrino  
analysis**

Charlie Mills

Submitted for the degree of Doctor of Philosophy  
University of Sussex  
August 2022

# **Declaration**

I hereby declare that this thesis has not been and will not be, submitted in whole or in part to another University for the award of any other degree.

Signature:

Charlie Mills

## ABSTRACT

The SNO+ experiment is a large scale liquid scintillator detector that is designed to undertake a large programme of neutrino physics. This thesis is concerned with the detection of reactor antineutrinos produced from nearby nuclear reactor cores via inverse beta decay (IBD). A maximum likelihood analysis to extract the neutrino oscillation parameters  $\Delta m_{21}^2$  and  $\theta_{12}$  from SNO+ data is presented.

The dominant background in this analysis are  $^{13}\text{C}(\alpha, n)^{16}\text{O}$  events that mimic IBD events. A method to distinguish the signal from background using PMT timing information is introduced. In the partially filled phase, it is shown that  $69.46 \pm 18.75\%$  of  $^{13}\text{C}(\alpha, n)^{16}\text{O}$  events can be removed for a  $6.60 \pm 0.05\%$  signal sacrifice. The event classification is validated using a small sample of IBD candidates identified in SNO+ data.

Finally, the impact of this background suppression technique is evaluated for the future data collection period of SNO+. It is shown that the world leading sensitivity for  $\Delta m_{21}^2$  is surpassed after 2.6 years of data taking using the event classification technique. In comparison, the world leading sensitivity is surpassed in 3.2 years if the background suppression method is not used.

# Acknowledgements

First and foremost I would like to thank my supervisor, Elisabeth Falk, for her immense support throughout the years that we have worked together. Without her guidance this thesis would not exist. I will be forever grateful for her ability to help me achieve my best.

A huge thank you must go towards the Sussex SNO+ group, past and present: Simon Peeters, Martti Nirko, Sammy Valder, Michal Rigan, James Page and Anthony Earle. Thank you for all the discussions, advice and support over the years. I'm not sure that I'll miss debugging TELLIE for hours on end, but I'll definitely miss the fun times we had along the way. I would also like to thank members of the EPP group who made moving to a new university way more fun: Aran Borkum, Iker de Icaza, Alex Booth, Marco Aparo, Daniela Köck, Nicolò Tuccori and Pierre Lasorak.

The SNO+ collaboration has been such a welcoming place to spend my time and it would be impossible to list all the members who have helped me along the way. I would like to thank Logan Lebanowski and Sofia Andringa for their ever present support over the last few years. Thanks to Erica Caden for thinking of all of the fun ways to improve run selection, working on this was one of my most enjoyable experiences in SNO+. A final thanks must go to Mark Ward for his patience when I underwent my training to become a DAQ expert.

A special thank you to all those that made Sudbury such a fun place to be (really). Spending hours and hours underground would have been nowhere near as fun without Benjamin Tam, Stephanie Walton, Ana Sofia Inácio, Lorna Nolan, Rachel Richardson, Cindy Lin and Matt Depatie. You are the best.

Last, but certainly not least, I would like to thank my family for their unconditional love and support throughout my entire life. Mum, Dad, Kate, Annie, Jordan, thank you so much for always believing in me, this thesis would not have been possible without you.

# Contents

<b>List of Tables</b>	<b>x</b>
<b>List of Figures</b>	<b>xiv</b>
<b>Preface</b>	<b>xv</b>
<b>1 Introduction</b>	<b>1</b>
<b>2 Neutrino Physics</b>	<b>3</b>
2.1 Introduction . . . . .	3
2.2 Neutrino oscillation . . . . .	5
2.2.1 Neutrino oscillation in a vacuum . . . . .	5
2.2.2 Oscillation in matter . . . . .	8
2.3 Measurement of oscillation parameters . . . . .	12
2.3.1 Reactor antineutrinos . . . . .	13
2.3.2 Atmospheric and solar neutrinos . . . . .	16
2.3.3 Accelerator neutrinos . . . . .	17
2.4 Neutrino mass . . . . .	18
2.4.1 Mass mechanisms . . . . .	18
2.4.2 $0\nu\beta\beta$ . . . . .	19
2.5 Future neutrino experiments . . . . .	23
2.6 Conclusion . . . . .	24
<b>3 The SNO+ Experiment</b>	<b>25</b>
3.1 Introduction . . . . .	25
3.2 General overview . . . . .	25
3.3 Phases of SNO+ . . . . .	27
3.3.1 Water phase . . . . .	27
3.3.2 Partial fill phase . . . . .	28

<b>CONTENTS</b>	<b>vi</b>
3.3.3 Pure liquid scintillator phase . . . . .	28
3.3.4 Tellurium loaded liquid scintillator phase . . . . .	29
3.4 Readout and data acquisition . . . . .	29
3.4.1 PMTs . . . . .	29
3.4.2 DAQ chain . . . . .	31
3.5 Data quality . . . . .	33
3.6 Software . . . . .	34
3.7 Reconstruction . . . . .	34
3.7.1 Event position and time . . . . .	34
3.7.2 Event energy . . . . .	35
<b>4 Calibration</b>	<b>37</b>
4.1 Introduction . . . . .	37
4.2 Calibration sources . . . . .	38
4.2.1 ELLIE . . . . .	38
4.3 Energy calibration with the $^{241}\text{Am}^9\text{Be}$ source . . . . .	39
4.4 Timing calibration . . . . .	41
4.4.1 TELLIE . . . . .	41
4.5 Optical calibration by light injection . . . . .	43
4.5.1 SMELLIE . . . . .	43
4.5.2 AMELLIE . . . . .	44
4.6 Monitoring optical attenuation . . . . .	46
4.6.1 Injection points . . . . .	46
4.6.2 Beam profile tuning . . . . .	47
4.6.3 Optical attenuation . . . . .	50
4.6.4 Further improvements . . . . .	55
4.7 Conclusion . . . . .	55
<b>5 Reactor antineutrinos at SNO+</b>	<b>56</b>
5.1 Introduction . . . . .	56
5.2 Sources of reactor antineutrinos . . . . .	57
5.3 Backgrounds . . . . .	58
5.3.1 Geoneutrinos . . . . .	59
5.3.2 $^{13}\text{C}(\alpha, n)^{16}\text{O}$ . . . . .	60
5.4 Detection . . . . .	62

---

<b>6 Prediction and selection of reactor IBD and <math>^{13}\text{C}(\alpha, n)^{16}\text{O}</math> events</b>	<b>65</b>
6.1 Introduction . . . . .	65
6.2 Prediction and simulation . . . . .	65
6.2.1 Reactor antineutrinos . . . . .	66
6.2.2 Geoneutrinos . . . . .	74
6.2.3 $^{13}\text{C}(\alpha, n)^{16}\text{O}$ . . . . .	76
6.3 Signal selection . . . . .	78
6.3.1 Analysis cuts . . . . .	78
6.4 Prediction . . . . .	80
6.4.1 Partially filled phase . . . . .	80
6.4.2 Fully filled scintillator phase . . . . .	81
6.5 Conclusion . . . . .	82
<b>7 Reactor antineutrino oscillation</b>	<b>83</b>
7.1 Introduction . . . . .	83
7.2 Oscillation parameter extraction . . . . .	83
7.2.1 PDFs of components . . . . .	84
7.2.2 Constraints . . . . .	87
7.2.3 Results in partial fill . . . . .	89
7.3 Conclusion . . . . .	92
<b>8 Improved sensitivity via identification of <math>^{13}\text{C}(\alpha, n)^{16}\text{O}</math> events</b>	<b>93</b>
8.1 Introduction . . . . .	93
8.2 $^{13}\text{C}(\alpha, n)^{16}\text{O}$ prompt event topology . . . . .	93
8.2.1 Interactions in simulation . . . . .	94
8.2.2 Proton timing calibration . . . . .	95
8.3 Discrimination of IBD and $^{13}\text{C}(\alpha, n)^{16}\text{O}$ events . . . . .	102
8.3.1 Partially filled phase . . . . .	103
8.3.2 Scintillator phase . . . . .	103
8.4 Impact on reactor sensitivity . . . . .	105
8.4.1 Partial fill . . . . .	105
8.4.2 Future sensitivity for SNO+ . . . . .	115
8.5 Conclusion . . . . .	118
<b>9 Conclusion</b>	<b>119</b>

<b>Bibliography</b>	<b>121</b>
<b>A List of acronyms</b>	<b>132</b>
<b>B Run selection</b>	<b>134</b>
B.1 Checks . . . . .	134
B.1.1 Run state . . . . .	135
B.1.2 Detector State . . . . .	135
B.1.3 DQHL . . . . .	135
B.1.4 Ping Crates . . . . .	136
B.1.5 Trigger Clock Jumps . . . . .	136
B.1.6 Channel Flags . . . . .	137
B.1.7 Muons . . . . .	137
B.1.8 Deck activity . . . . .	137
B.2 Monitoring . . . . .	137
<b>C Reactor core information</b>	<b>141</b>
<b>D Analysis blindness</b>	<b>142</b>
D.1 Introduction . . . . .	142
D.2 Methodology . . . . .	142
D.2.1 Removing Bruce . . . . .	143
D.2.2 Removing Ontario reactors . . . . .	143
D.3 Proposal . . . . .	144

# List of Tables

2.1	The best global fit of the oscillation parameters.	13
4.1	The various calibration sources available to be used in the SNO+ detector.	39
4.2	The deviation between the estimated and fitted beam spot centre for each AMELLIE fibre.	48
6.1	The relative contribution from each isotope in the fuel of the three modelled reactor designs.	67
6.2	The components and uncertainties for the IBD cross section normalisation constant.	73
6.3	The predicted geoneutrino flux for three different geological models.	75
6.4	The analysis cuts used to select IBD candidate event pairs.	79
6.5	The expected number of events in the partial fill phase.	80
6.6	The expected number of events in the scintillator phase.	82
7.1	The uncertainties of the components in the oscillation analysis.	88
8.1	The $\alpha$ and $\beta$ scintillation time constants in the partially filled phase.	96
8.2	The analysis cuts used to select $^{241}\text{Am}^9\text{Be}$ candidate event pairs.	101
8.3	The impact of applying the classifier to MC events that have been produced with different scintillator time constants for protons.	108
8.4	The gradients of the straight line fits used in the classifier systematic calculation.	109
8.5	The expected number of events in the partial fill phase after event classification.	110
B.1	The run state checks.	135
B.2	The detector state checks.	139
B.3	The alarm checks.	140

**LIST OF TABLES**

---

**x**

- C.1 Information for the reactor cores located within 1000 km of SNO+ . . . . . 141

# List of Figures

2.1	The effective mixing angle in matter as a function of neutrino energy. . . . .	11
2.2	The effective mixing angle in matter as a function of electron density. . . . .	12
2.3	The $\bar{\nu}_e$ survival probability as a function of oscillation baseline. . . . .	14
2.4	The $\bar{\nu}_e$ survival probability as a function of energy. . . . .	16
2.5	The Feynman diagrams for $2\nu\beta\beta$ and $0\nu\beta\beta$ . . . . .	20
2.6	The effective Majorana mass as a function of the lightest neutrino mass. . .	22
2.7	The experimental signature of $0\nu\beta\beta$ . . . . .	22
3.1	A drawing of the SNO+ detector. . . . .	26
3.2	A photo of the SNO+ detector during the partial fill. . . . .	28
3.3	Cartoon of the SNO+ readout and DAQ system describing the major components. . . . .	30
3.4	A photo of a SNO+ PMT concentrator. . . . .	30
3.5	The total efficiency of the PMTs used in SNO+, as measured by the SNO collaboration. . . . .	31
3.6	The $N_{\text{hits}}$ and reconstructed energy of $^{13}\text{C}(\alpha, n)^{16}\text{O}$ prompt events simulated in the SNO+ detector. . . . .	36
4.1	A schematic of the different ELLIE systems. . . . .	40
4.2	A photo of the TELLIE rack in the DCR. . . . .	42
4.3	A photo of the inside of a box containing the electronics for 8 AMELLIE channels. . . . .	43
4.4	Drawings of the PMT hex cell and AMELLIE mounting plates. . . . .	45
4.5	A PMT hit map for an AMELLIE run with a fit for the beamspot centre. .	47
4.6	The distributions that are sampled when generating photons in the AMELLIE simulation. . . . .	49
4.7	The AMELLIE beam profiles before and after the angular distribution tuning. .	50

---

4.8	The ratio of fits to AMELLIE beam profiles. . . . .	51
4.9	The absorption and scattering lengths of the liquid scintillator cocktail. . . . .	51
4.10	The residual hit time and PMT position phase space for a typical AMELLIE run. . . . .	52
4.11	The residual hit time and PMT position phase space for simulated AMELLIE MC, separated by optical path. . . . .	53
4.12	The figures of merit used to measure the change in optical properties. . . . .	54
5.1	The uranium decay chain. . . . .	61
5.2	Cartoon of an IBD interaction. . . . .	62
5.3	Cartoon of the processes in an $^{13}\text{C}(\alpha, n)^{16}\text{O}$ interaction. . . . .	63
6.1	The antineutrino spectra of the four contributing isotopes in nuclear reactor fuels. . . . .	67
6.2	Comparison of the load factors given by the IAEA and calculated using data from the IESO for a typical reactor core. . . . .	69
6.3	Evolution of the load factor over one year for a typical Bruce reactor core. .	70
6.4	The antineutrino flux intensity of nuclear reactors close to SNO+. . . . .	71
6.5	The expected reactor antineutrino flux at SNO+. . . . .	72
6.6	The geoneutrino energy spectrum for U and Th chains. . . . .	75
6.7	The total $^{13}\text{C}(\alpha, n)^{16}\text{O}$ cross section. . . . .	77
6.8	The $\Delta T$ and $\Delta R$ distributions for reactor IBD and $^{13}\text{C}(\alpha, n)^{16}\text{O}$ MC events.	80
6.9	The predicted prompt event energy spectrum in the partial fill. . . . .	81
6.10	The predicted prompt event energy spectrum in the scintillator phase. . . . .	82
7.1	The PDF used in the likelihood fitting routine for the Pickering reactor complex. . . . .	85
7.2	The three PDFs used in the likelihood fitting routine for the $^{13}\text{C}(\alpha, n)^{16}\text{O}$ events. . . . .	86
7.3	The likelihood phase space for $\Delta m_{21}^2$ and $\theta_{12}$ for an Asimov data set in the partially filled phase. . . . .	90
7.4	The likelihood space for $\Delta m_{21}^2$ with $\theta_{12}$ fixed in the partially filled phase. .	90
7.5	The likelihood space for $\Delta m_{21}^2$ with varying rate of $^{13}\text{C}(\alpha, n)^{16}\text{O}$ events. .	91
7.6	The oscillation fit result for the observed IBD candidates in the partially filled phase. . . . .	92

---

8.1	The fraction of photons in $^{13}\text{C}(\alpha, n)^{16}\text{O}$ prompt events by origin particle. . . . .	94
8.2	The number of scattered protons in low energy $^{13}\text{C}(\alpha, n)^{16}\text{O}$ events. . . . .	95
8.3	The time at which protons are scattered in MC $^{13}\text{C}(\alpha, n)^{16}\text{O}$ events. . . . .	96
8.4	The scintillation time profiles of $\alpha$ and $\beta$ particles in the partially filled detector. . . . .	97
8.5	The time residual profiles of $^{13}\text{C}(\alpha, n)^{16}\text{O}$ data and MC events in the partially filled detector with $\beta$ time constants. . . . .	98
8.6	The time residual profiles of $^{13}\text{C}(\alpha, n)^{16}\text{O}$ data and MC events in the partially filled detector with $\alpha$ time constants. . . . .	99
8.7	The peak of the time residual profiles of $^{13}\text{C}(\alpha, n)^{16}\text{O}$ data and MC events in the partially filled detector. . . . .	100
8.8	The $N_{\text{hits}}$ distribution of events during the $^{241}\text{Am}^9\text{Be}$ source deployment. . . . .	101
8.9	The time residual profiles of $^{241}\text{Am}^9\text{Be}$ data and MC events in the partially filled detector. . . . .	102
8.10	The PDFs used for event discrimination in the partially filled phase. . . . .	103
8.11	The likelihood ratio for IBD and $^{13}\text{C}(\alpha, n)^{16}\text{O}$ MC events in the partially filled phase. . . . .	104
8.12	The PDFs used for event discrimination in the full scintillator phase. . . . .	104
8.13	The likelihood ratio for IBD and $^{13}\text{C}(\alpha, n)^{16}\text{O}$ MC events in the full scintillator phase. . . . .	105
8.14	The classifier cut optimisation curves in the partially filled phase. . . . .	106
8.15	The classifier cut optimisation curves in the partially filled phase for different $^{13}\text{C}(\alpha, n)^{16}\text{O}$ rates. . . . .	107
8.16	The likelihood space for $\Delta m_{21}^2$ and $\theta_{12}$ after using the prompt event classifier for an Asimov MC data set. . . . .	111
8.17	The likelihood space for $\Delta m_{21}^2$ after using the prompt event classifier for an Asimov MC data set. . . . .	112
8.18	The prompt energy spectra in the partially filled phase for data and MC before and after applying the event classification. . . . .	112
8.19	The likelihood ratio distributions in data and MC. . . . .	113
8.20	The likelihood space for $\Delta m_{21}^2$ and $\theta_{12}$ after using the prompt event classifier. . . . .	114
8.21	The likelihood space for $\Delta m_{21}^2$ after using the prompt event classifier. . . . .	114
8.22	The optimised classifier cut value as a function of data taking livetime. . . . .	116

8.23 The sensitivity of SNO+ to $\Delta m_{21}^2$ as a function of livetime in the scintillator phase. . . . .	117
8.24 The sensitivity of SNO+ to $\Delta m_{21}^2$ as a function of livetime in the scintillator phase. . . . .	117
B.1 The run selection results for a typical week of data collection. . . . .	138
D.1 The result of the oscillation fit for Asimov data sets corresponding to one year of live time. When Bruce is turned off, the "missing" events are redistributed to other reactor cores. . . . .	144
D.2 The result of the oscillation fit for Asimov data sets corresponding to one year of live time in the full scintillator phase assuming $\Delta m_{21}^2 = 7.53 \times 10^{-5}$ eV <sup>2</sup> . The fraction quoted in the legend is a reflection of how "on" the reactor is. . . . .	145

# Preface

This preface serves to outline the author’s contributions for the topics and analysis introduced in this thesis. It will also acknowledge contributions from colleagues where appropriate.

The second chapter is a summary of the physics that is relevant to the topics of later chapters. As such the content in this chapter is drawn from textbooks, publications and lecture material from a variety of sources. The third chapter is an overview of the SNO+ detector and utilises material from technical design notes, publications and internal documentation. The author contributed to the loading of the liquid scintillator into the detector, made significant contributions to the data quality processes described in Appendix B and undertook training to become a DAQ expert, ensuring that the experiment was able to collect high quality data for use in analyses.

The fourth chapter introduces the methods by which the detector is calibrated. All sections regarding the analysis using AMELLIE is the author’s own work. The author also contributed to data collection campaigns for TELLIE and hardware maintenance of TELLIE and AMELLIE, along with the SNO+ group at the University of Sussex. The fifth chapter introduces the wider topic of reactor antineutrinos and as such contains information sourced from textbooks, publications and outreach material.

The sixth chapter describes the simulation and prediction of signal and background events in the analysis. It uses information sourced from internal documents, textbooks and publications. The author implemented a re-expressed inverse beta decay cross section calculation, based on work by Vogel et al., and the scaling of reactor fluxes by their actual operating power. The author assisted in the determination of the analysis cuts that are used in the SNO+ antineutrino analyses, whereby publications are in preparation.

The seventh chapter outlines an analysis to extract oscillation parameters using reactor antineutrinos identified in SNO+. The analysis presented is the author’s own work. The small sample of inverse beta decay candidates were identified by Iwan Morton-Blake and Thiago Bezerra, while the small sample of pure  $^{13}\text{C}(\alpha, n)^{16}\text{O}$  events were identified by

Matthew Cox. The analysis reported using these event samples is the author's own work. The final chapter describes the improvements made by the author to enhance the power of the analysis described in the seventh chapter.

# Chapter 1

## Introduction

Since the confirmation of neutrino oscillation in 2001 by the Nobel prize winning SNO [1] and Super-Kamiokande experiments [2], neutrino physics has quickly moved into the precision era. Most of the constants of nature that govern neutrino oscillation are known with small uncertainties and efforts are focused on producing even more precise measurements of these parameters.

At the same time, the number of unanswered questions in neutrino physics seems larger than ever. What is the absolute mass scale of neutrinos? What is the sign of  $\Delta m_{32}^2$  and thus the neutrino mass hierarchy? Are neutrinos Dirac or Majorana in nature? Are there sterile neutrinos? Do neutrinos violate CP symmetry? Many of these questions will be answered in the coming years by next generation neutrino experiments such as DUNE [3] and Hyper-Kamiokande [4].

While the majority of the neutrino oscillation parameters are known with good precision, there still remains some tension in the measured value of  $\Delta m_{21}^2$ . Experiments that measure this parameter via detection of solar neutrinos, such as Super-Kamiokande, disagree with experiments that determine this parameter by detecting reactor antineutrinos, such as KamLAND [5]. The tension is on the order of  $2.15\sigma$ .

This thesis introduces a method to improve the sensitivity of the SNO+ experiment to the oscillation parameter  $\Delta m_{21}^2$ . This will enhance the potential contribution to understanding the aforementioned tension. This is achieved by developing analysis techniques to characterise and reduce the largest background in the reactor antineutrino analysis. This analysis measures the flux of antineutrinos at SNO+ that are produced in nuclear reactor cores to extract the neutrino oscillation parameters. Suppressing the background through analysis techniques allows for a measurement to be made with a shorter experimental live time.

Chapter 2 introduces neutrino physics and describes the origin of neutrino oscillation. The current status of experimental neutrino physics is also discussed. A brief overview of the SNO+ detector is given in Chapter 3. The calibration of the detector is discussed in Chapter 4, with particular focus given to optical calibration. This chapter outlines the progress made for the monitoring of optical attenuation in the detector.

Chapter 5 introduces and motivates the reactor antineutrino analysis within SNO+ in the context of the general neutrino landscape. Chapter 6 describes how the reactor antineutrino flux is predicted and simulated in the SNO+ detector. The same processes are also described for the main backgrounds present in this analysis. Finally, this chapter outlines how these events are selected in the SNO+ data.

Chapter 7 describes an oscillation analysis to extract  $\Delta m_{21}^2$  and  $\theta_{12}$  from the SNO+ data, applicable to both real and MC generated data. Chapter 8 introduces a method to calibrate the scintillation time profile of protons in the SNO+ detector and results given for the partially filled phase of SNO+. A technique to distinguish between reactor antineutrinos and the major background,  $^{13}\text{C}(\alpha, n)^{16}\text{O}$  events, is described with the systematic uncertainties associated with such a technique discussed. Finally, the result of applying this technique on data and MC generated data is shown, along with the outlook for the future of this analysis within SNO+.

Finally, Chapter 9 outlines the main conclusions of this thesis.

## Chapter 2

# Neutrino Physics

### 2.1 Introduction

The neutrino was first proposed in 1930 by Wolfgang Pauli in order to conserve energy and momentum in  $\beta$  decay, where the electrons were observed to be emitted with a range of energies [6]. Pauli had suggested that such a particle would have no electric charge and therefore could be called a neutron, but the discovery of the heavy neutral particle within the nucleus by James Chadwick [7] led to the need for a new name. Enrico Fermi started using the name “neutrino” for Pauli’s small neutral particle and consolidated the theoretical basis for its existence in his theory of  $\beta$  decay [8].

The first experimental hint for the existence of neutrinos was published in 1938 when H. R. Crane and J. Halpern studied the nuclear recoil of particles in a cloud chamber. Their findings indicated that there should be another particle (the neutrino) present in the interactions [9]. The first direct detection of neutrinos came in 1956 courtesy of the experiment devised by C. Cowan and F. Reines [10]. In this experiment, antineutrinos from a nuclear reactor were detected by the inverse beta decay (IBD) interaction, proceeding as

$$\bar{\nu}_e + p \rightarrow n + e^+. \quad (2.1)$$

The positron will annihilate with an electron very quickly, while the neutron will undergo a capture on an atomic nucleus some time later. This leads to a clear coincident signal with a distinctive experimental signature. The IBD process will be discussed in more detail in later chapters.

Following the work of C. N. Yang and R. Mills to explain the existence of strong interactions [11], parity conservation violation by C-S. Wu [12], the formulation of electroweak

theory by S. Glashow [13] and the subsequent incorporation of the Higgs mechanism [14] by S. Weinberg [15] and A. Salam [16] forms much of the Standard Model of Particle Physics (SM). The SM organises fundamental particles into two categories: force carriers and matter particles. The force carrier particles are bosons with spin 1. There is a boson for three of the four fundamental forces: the weak force, the strong force and the electromagnetic force. The SM does not account for gravity. Matter particles interact with each other through the fundamental forces via exchange of bosons. The photon mediates the electromagnetic force, the gluons mediate the strong force while the W and Z bosons mediate the weak force. Furthermore weak interactions can be charged-current (via exchange of  $W^+$  or  $W^-$  bosons) or neutral-current ( $Z^0$ ) interactions. Finally, the Higgs boson has spin 0 and arises due to an excitation of the Higgs field [14]. A brief introduction to the Higgs mechanism is given in Section 2.4.1

The matter particles are fermions with spin  $\frac{1}{2}$  and are split into two families: quarks and leptons. Each fermion has a corresponding antifermion with opposite electric charge. The quarks are particles which participate in strong interactions while leptons do not feel the strong force and instead undergo weak interactions. There are three flavours of charged lepton: the electron  $e$ , the muon  $\mu$  and the tau  $\tau$ . Each generation of lepton have the same electric charge but increasing mass, that is,  $m_e < m_\mu < m_\tau$ . For each charged lepton there is a corresponding neutrino: the electron neutrino  $\nu_e$ , the muon neutrino  $\nu_\mu$  and the tau neutrino  $\nu_\tau$ . The neutrino that Cowan and Reines detected was the electron antineutrino, while the muon neutrino was detected in 1962 by L. Lederman et al. [17]. The tau neutrino was not detected until 2000 by the DONUT collaboration [18].

The SM provides an explanation for how particles acquire mass via the Higgs mechanism [14]. This mechanism requires a particle to have two types of helicity, or handedness, to gain mass. By observing electron capture interactions M. Goldhaber, L. Grodzins and A. W. Sunyar discovered that neutrinos have negative helicity, that is, they are left-handed [19]. The lack of a right-handed component for neutrinos led to the assumption within the SM that neutrinos are massless particles.

The confirmation of neutrino oscillation by the SNO and Super-Kamiokande experiments was experimental proof that neutrinos are in fact not massless [1], [2]. This was the first measurement of beyond the standard model (BSM) physics. SNO solved the longstanding Solar Neutrino Problem, first reported by the Homestake experiment [20]. The amount of electron neutrinos detected on Earth that were produced in the nuclear fusion reactions taking place in the Sun's core was inconsistent with solar models. The

SNO detector was able to detect all three flavours of neutrinos and subsequently found the total neutrino flux to be consistent with solar models, thus proving that neutrinos can oscillate between flavours. Oscillation is only possible if neutrinos are not massless.

An introduction to the theory of neutrino oscillation is provided in this chapter. An overview of oscillation in a vacuum is then followed by an extension of oscillation for neutrinos travelling through matter. The techniques employed to measure the parameters that govern neutrino oscillation are discussed along with the status of current neutrino experiments. The questions surrounding neutrino mass and the search for neutrinoless double beta decay is introduced before finally looking towards the future of neutrino physics. The derivations of neutrino oscillations in vacuum and matter draw on those given by Giunti and Kim [21] and are supported by those given in [22], [23].

## 2.2 Neutrino oscillation

### 2.2.1 Neutrino oscillation in a vacuum

The process of neutrino oscillation involves the change in flavour of neutrinos as they propagate through space. Practically this means that an electron neutrino created at a source may manifest as a muon or tau neutrino when it is detected. Such a change in flavour is allowed as the three flavour eigenstates ( $|\nu_{e,\mu,\tau}\rangle$ ) are a superposition of three mass eigenstates ( $|\nu_{1,2,3}\rangle$ ). The transformation between the flavour,  $|\nu_\alpha\rangle$ , and mass,  $|\nu_x\rangle$ , eigenstates are written as

$$|\nu_\alpha\rangle = \sum_x U_{\alpha,x}^* |\nu_x\rangle \quad (2.2)$$

and

$$|\nu_x\rangle = \sum_\alpha U_{\alpha,x} |\nu_\alpha\rangle, \quad (2.3)$$

where  $U$  is the Pontecorvo-Maki-Nakagawa-Sakata (PMNS) matrix [24], [25]. In the full description of three-flavour neutrino oscillation the PMNS matrix is a 3x3 matrix of the form

$$U = \begin{pmatrix} U_{e,1} & U_{e,2} & U_{e,3} \\ U_{\mu,1} & U_{\mu,2} & U_{\mu,3} \\ U_{\tau,1} & U_{\tau,2} & U_{\tau,3} \end{pmatrix}. \quad (2.4)$$

The neutrino mass states are eigenstates of the Hamiltonian,  $\mathcal{H}_0$ , with energy eigenvalues

$$E_x = \sqrt{p^2 + m_x^2}. \quad (2.5)$$

As with many quantum mechanical systems it is useful to consider the evolution of the mass states over time with the time dependent Schrödinger equation as

$$i\frac{d}{dt}|\nu_x(t)\rangle = \mathcal{H}_0|\nu_x(t)\rangle \quad (2.6)$$

with solutions of the form

$$|\nu_x(t)\rangle = e^{-iE_xt}|\nu_x\rangle. \quad (2.7)$$

Now considering a neutrino created at time  $t = 0$  with a definite flavour,  $\alpha$ , while substituting Equations 2.2 and 2.3 into Equation 2.7, the evolution of the flavour state is

$$|\nu_\alpha(t)\rangle = \sum_{\beta} \left( \sum_x U_{\alpha,x}^* e^{-iE_xt} U_{\beta,x} \right) |\nu_\beta\rangle, \quad (2.8)$$

where  $\beta = e, \mu, \tau$ . Equation 2.8 shows that a neutrino created at  $t = 0$  with a pure flavour state is a superposition of the other flavour states at  $t > 0$  if the PMNS matrix is not diagonal. Furthermore, the amplitude of the transition from flavour state  $\alpha$  to  $\beta$  is

$$\langle \nu_\beta | \nu_\alpha(t) \rangle = \sum_x U_{\alpha,x}^* U_{\beta,x} e^{-iE_xt}. \quad (2.9)$$

Finally, the probability of transition is

$$P_{\nu_\alpha \rightarrow \nu_\beta}(t) = |\langle \nu_\beta | \nu_\alpha(t) \rangle|^2 = \sum_{x,y} U_{\alpha,x}^* U_{\beta,x} U_{\alpha,y} U_{\beta,y}^* e^{-i(E_x - E_y)t}. \quad (2.10)$$

The probability of transition given by Equation 2.10 can be simplified by considering that neutrinos are ultrarelativistic particles. Using the assumption that  $m \ll p$  and applying a Taylor expansion to Equation 2.5, the energy of a mass state can be approximated as

$$E_x \simeq E + \frac{m_x^2}{2E}. \quad (2.11)$$

Using this approximation the energy difference between two mass states can be expressed as

$$E_x - E_y \simeq \frac{m_x^2 - m_y^2}{2E} = \frac{\Delta m_{xy}^2}{2E}. \quad (2.12)$$

When considering the experimental detection of neutrinos, the time since the neutrino was created is unknown. The known quantity is the distance,  $L$ , from the neutrino source to the detector. Since the neutrinos are ultrarelativistic, an approximation that  $t \approx L$  is made. With this approximation and substituting Equation 2.12 into Equation 2.10, the probability of transition is reexpressed as

$$P_{\nu_\alpha \rightarrow \nu_\beta}(L, E) = \sum_{x,y} U_{\alpha,x}^* U_{\beta,x} U_{\alpha,y} U_{\beta,y}^* e^{-i \frac{\Delta m_{xy}^2 L}{2E}}. \quad (2.13)$$

Equation 2.13 shows how neutrino oscillation experiments are able to probe elements of the PMNS matrix and the squared difference of the mass states.  $L$  and  $E$  are known quantities when neutrinos are detected and therefore if the flux of neutrinos of a given flavour at the detector is compared to that of the source then the oscillation probability can be inferred. This allows the values of the  $\Delta m_{xy}^2$  and elements of  $U$  to be measured. Detectors are usually built in one position and thus  $L$  is fixed. Detecting neutrinos with a range of energies is therefore required to probe the oscillation parameters. It is important to note that oscillation experiments do not probe the absolute neutrino masses, rather the squared difference of the mass states. Therefore other experiments must be designed to determine the absolute mass, an example of which is the KATRIN experiment [26].

The PMNS matrix described in Equation 2.4 is actually the product of two matrices as

$$U = U^D U^M, \quad (2.14)$$

where  $U^D$  is the Dirac matrix and  $U^M$  is the Majorana matrix.  $U^M$  is a diagonal matrix with terms 1,  $e^{-i\eta_1}$  and  $e^{-i\eta_2}$ , where  $\eta_1$  and  $\eta_2$  are the Majorana phase terms [27]. The Majorana phase terms are non-zero if neutrinos are described as Majorana particles. The Dirac or Majorana nature of neutrinos is a very active area of research and experiments such as SNO+ are aiming to answer this question [28], [29], [30]. Even if the Majorana phases are non-zero there is no effect on the neutrino oscillation probability [31].

The elements of  $U^D$  contain the constants of nature that govern neutrino oscillation. This matrix is commonly expressed as

$$U^D = \begin{pmatrix} 1 & 0 & 0 \\ 0 & c_{23} & s_{23} \\ 0 & -s_{23} & c_{23} \end{pmatrix} \begin{pmatrix} c_{13} & 0 & s_{13}e^{-i\delta} \\ 0 & 1 & 0 \\ -s_{13}e^{i\delta} & 0 & c_{13} \end{pmatrix} \begin{pmatrix} c_{12} & s_{12} & 0 \\ -s_{12} & c_{12} & 0 \\ 0 & 0 & 1 \end{pmatrix} \quad (2.15)$$

using the notation  $c_{xy} = \cos(\theta_{xy})$  and  $s_{xy} = \sin(\theta_{xy})$ .  $\delta$  is a phase term quantifying

the level of CP violation present in neutrino mixing. Therefore the constants that govern neutrino oscillation are the three mixing angles, three mass splittings and the CP violating phase term. These parameters are probed by various neutrino oscillation experiments. Practically, only  $\Delta m_{21}^2$  and  $\Delta m_{23}^2$  are measured, since  $\Delta m_{31}^2$  can be inferred by the sum of the three mass splittings being equal to zero.

### 2.2.2 Oscillation in matter

The oscillation described in Section 2.2.1 is valid for neutrinos travelling in a vacuum. Neutrinos that are not in a vacuum will feel a potential due to elastic forward scattering off electrons and nucleons present in matter. It is commonly described as analogous to the refractive index of a material affecting the propagation of photons. The scattering can be mediated by the W boson or the Z boson. Exchange of a W boson is a charged current interaction that is only available to electron flavour neutrinos. Exchange of a Z boson is a neutral current interaction and is available to all flavours of neutrinos.

The Hamiltonian is modified to include an extra term corresponding to the matter such that

$$\mathcal{H} = \mathcal{H}_0 + \mathcal{H}_1, \quad (2.16)$$

where  $\mathcal{H}_0$  is the vacuum oscillation Hamiltonian described in Section 2.2.1 and  $\mathcal{H}_1|\nu_\alpha\rangle = V_\alpha|\nu_\alpha\rangle$ . Here,  $V_\alpha$  is the potential energy of a neutrino of  $\alpha$  flavour that is propagating through the matter. This potential energy is constructed by considering both the neutral current and charged current interactions, as

$$V_\alpha = V_{CC}\delta_{\alpha,e} + V_{NC}. \quad (2.17)$$

The terms in Equation 2.18 are given by

$$V_{CC} = \pm\sqrt{2}G_F N_e \text{ and } V_{NC} = \mp\frac{1}{2}\sqrt{2}G_F N_n. \quad (2.18)$$

$N_e$  and  $N_n$  are the electron and neutron number densities, while  $G_F$  is the Fermi coupling constant. The sign change is required when considering the propagation of antineutrinos. It can be seen in the neutral current channel that the potentials of the protons and electrons cancel, leaving only the contribution from neutrons.

As with vacuum oscillations, the time dependent Schrödinger equation can be used to evaluate the evolution of the flavour states. The equation can be simplified by once again using the ultrarelativistic approximations introduced in Section 2.2.1. Additionally, a

phase shift can be introduced that removes one of the terms of the equation. Of particular importance is the loss of dependence on  $V_{NC}$  as a result of the phase shift, leaving only a dependence on  $V_{CC}$ . The equation is finally expressed as

$$i \frac{d}{dt} \langle \nu_\beta | \nu_\alpha(t) \rangle = \sum_\eta \left( \sum_x U_{\beta,x} \frac{\Delta m_{x,1}^2}{2E} U_{\eta,x}^* + \delta_{\beta,e} \delta_{\eta,e} V_{CC} \right) \langle \nu_\alpha | \nu_\eta(t) \rangle. \quad (2.19)$$

It is also possible to express Equation 2.19 in matrix form, as

$$i \frac{d}{dt} \phi_\alpha = \mathcal{H}_F \phi_\alpha \quad (2.20)$$

whereby  $\mathcal{H}_F$  is an effective Hamiltonian of the form

$$\mathcal{H}_F = \frac{1}{2E} (U \mathbb{M}^2 U^\dagger + \mathbb{A}). \quad (2.21)$$

The matrices in Equations 2.20 and 2.21 are

$$\phi_\alpha = \begin{pmatrix} \langle \nu_e | \nu_\alpha(t) \rangle \\ \langle \nu_\mu | \nu_\alpha(t) \rangle \\ \langle \nu_\tau | \nu_\alpha(t) \rangle \end{pmatrix}, \mathbb{M}^2 = \begin{pmatrix} 0 & 0 & 0 \\ 0 & \Delta m_{21}^2 & 0 \\ 0 & 0 & \Delta m_{31}^2 \end{pmatrix}, \mathbb{A} = \begin{pmatrix} A_{CC} & 0 & 0 \\ 0 & 0 & 0 \\ 0 & 0 & 0 \end{pmatrix} \quad (2.22)$$

where

$$A_{CC} = 2EV_{CC} = 2\sqrt{2}EG_F N_e. \quad (2.23)$$

### 2.2.2.1 The MSW effect

The Mikheyev-Smirnov-Wolfenstein (MSW) effect is the emergence of a resonance in the effective neutrino mixing angle when the electron density in matter is a specific value [32], [33], [34]. For simplicity, the case of two neutrino mixing between  $\nu_e$  and  $\nu_\mu$  is assumed, whereby the PMNS matrix (Equation 2.15) simplifies to

$$U = \begin{pmatrix} \cos(\theta) & \sin(\theta) \\ -\sin(\theta) & \cos(\theta) \end{pmatrix}. \quad (2.24)$$

As there are only two neutrinos there is one mixing angle,  $\theta$ , and one mass splitting,  $\Delta m^2$ .

Using this simplified PMNS matrix, the effective Hamiltonian (Equation 2.21) is

$$\mathcal{H}_F = \frac{1}{4E} \begin{pmatrix} -\Delta m^2 \cos(2\theta) & \Delta m^2 \sin(2\theta) \\ \Delta m^2 \sin(2\theta) & \Delta m^2 \cos(2\theta) \end{pmatrix} \quad (2.25)$$

and the matter potential matrix,  $\mathbb{A}$ , is expressed as

$$\mathbb{A} = \begin{pmatrix} \frac{A_{CC}}{2} & 0 \\ 0 & \frac{A_{CC}}{2} \end{pmatrix}, \quad (2.26)$$

as this term is proportional to the identity matrix. That is to say, the potential impacts both neutrino flavours equally and therefore it does not change the oscillation probability. The new Hamiltonian described in Equation 2.25 can be inserted into Equation 2.20, giving

$$i \frac{d}{dt} \begin{pmatrix} \phi_{ee} \\ \phi_{e\mu} \end{pmatrix} = \frac{1}{4E} \begin{pmatrix} -\Delta m^2 \cos(2\theta) & \Delta m^2 \sin(2\theta) \\ \Delta m^2 \sin(2\theta) & \Delta m^2 \cos(2\theta) \end{pmatrix} \begin{pmatrix} \phi_{ee} \\ \phi_{e\mu} \end{pmatrix}. \quad (2.27)$$

It is possible to diagonalise the Hamiltonian described in Equation 2.25 such that the effective Hamiltonian in the mass basis is

$$\mathcal{H}_M = U_M^T \mathcal{H}_F U_M = \frac{1}{4E} \begin{pmatrix} -\Delta m_M^2 & 0 \\ 0 & \Delta m_M^2 \end{pmatrix}. \quad (2.28)$$

The new effective mixing matrix is defined as

$$U = \begin{pmatrix} \cos(\theta_M) & \sin(\theta_M) \\ -\sin(\theta_M) & \cos(\theta_M) \end{pmatrix} \quad (2.29)$$

with the effective mass splitting now

$$\Delta m_M^2 = \sqrt{(\Delta m^2 \cos(2\theta) - A_{CC})^2 + (\Delta m^2 \sin(2\theta))^2}. \quad (2.30)$$

Furthermore, the effective mixing angle,  $\theta_M$ , is defined by

$$\cos(2\theta_M) = \frac{\Delta m^2 \cos(2\theta) - A_{CC}}{\Delta m_M^2} \text{ and } \sin(2\theta_M) = \frac{\Delta m^2 \sin(2\theta)}{\Delta m_M^2}, \quad (2.31)$$

leading to the final definition of  $\theta_M$  as

$$\tan(2\theta_M) = \frac{\tan(2\theta)}{1 - \frac{A_{CC}}{\Delta m^2 \cos(2\theta)}}. \quad (2.32)$$

The MSW effect is the realisation that there is a resonance in the effective mixing angle for the case when

$$A_{CC}^R = \Delta m^2 \cos(2\theta), \quad (2.33)$$

which can be expressed in terms of the electron number density (Equation 2.23),

$$N_e^R = \frac{\Delta m^2 \cos(2\theta)}{2\sqrt{2}EG_F}. \quad (2.34)$$

When this resonance condition is satisfied the effective mixing angle is equal to  $\frac{\pi}{4}$  and the mixing is maximal, that is, it is possible for a pure electron neutrino flavour to transition to a pure muon neutrino flavour.

Figure 2.1 demonstrates the relationship between the neutrino energy,  $E$ , and the effective mixing angle,  $\theta_M$ , for a constant electron density. The figure also shows this relationship for various values of  $\theta$ . It is clear to see the resonance peak arises for all values of  $\theta$ , leading to large probabilities of transmission even with small mixing angles. The resonance peak is wider for larger  $\theta$ , enhancing the transition probability further. Figure 2.1 was generated using an electron density that was calculated by assuming a mass density of  $3 \text{ g/cm}^3$ . This is a good estimate for the density in the Earth's crust [35] and this corresponds to an electron density of  $9 \times 10^{23} \text{ cm}^{-3}$ . The resonance peak appears at neutrino energies of the order of GeV and this energy is well within the range of neutrino beam experiments. Reactor antineutrinos are emitted with energies of the order of MeV where  $\theta_M \approx \theta$ . Therefore it is assumed that matter effects have a negligible impact on reactor antineutrino oscillation analyses.

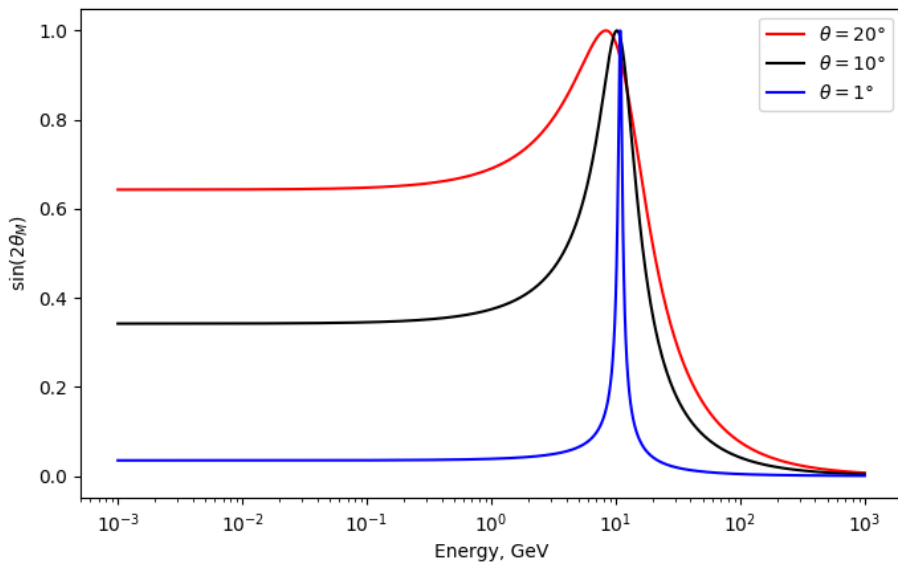


Figure 2.1: The effective mixing angle in matter as a function of neutrino energy. The mass density used in the calculation is  $3 \text{ g/cm}^3$  and  $\Delta m^2 = 2.5 \times 10^{-3} \text{ eV}^2$ . The resonance peak for the effective mixing angle arises for neutrinos with energy of the order of GeV.

Figure 2.2 shows the how the effective mixing angle varies as a function of the electron density in the medium the neutrino is travelling through. The figure shows this relationship for two given neutrino energies corresponding to the typical energy for reactor antineutrinos and neutrinos produced by a neutrino beam such as NuMI. This plot further confirms the assumption that matter effects are negligible for a reactor antineutrino analysis.

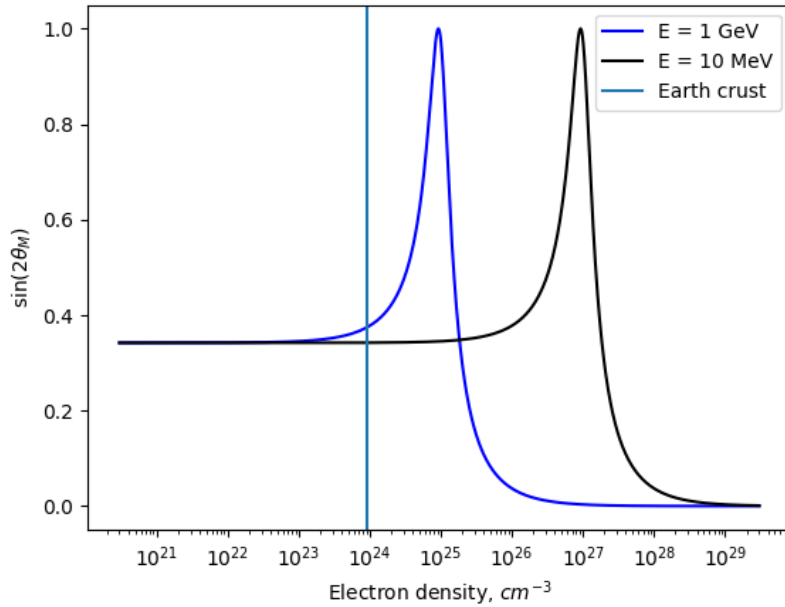


Figure 2.2: The effective mixing angle in matter as a function of the electron density. The mass difference in the calculation is  $\Delta m^2 = 2.5 \times 10^{-3} \text{ eV}^2$ . The effective mixing angle is not enhanced for neutrinos with energies on the order of MeV.

## 2.3 Measurement of oscillation parameters

The form of the Dirac PMNS matrix,  $U^D$ , as in Equation 2.15 is such that the parameters are separated by the type of experiment and neutrino source which are most sensitive to them. It will be seen in this section that  $\theta_{12}$  and  $\Delta m_{21}^2$  are primarily determined by the observation of solar neutrinos. These are neutrinos created during the fusion process within the Sun. It is also possible to measure these parameters using long baseline reactor antineutrinos. KamLAND has thus far produced the best measurement of  $\Delta m_{21}^2$  [36] and SNO+ will also make a competitive measurement. Accelerator experiments such as NOvA and T2K can probe these two parameters, as well as  $\delta_{CP}$ ,  $\theta_{13}$ ,  $\theta_{23}$  and  $\Delta m_{32}^2$ .  $\theta_{23}$  and  $\Delta m_{32}^2$  are determined by observing atmospheric neutrinos. These neutrinos

Table 2.1: The best global fit values of the oscillation parameters, as quoted by the PDG [37] assuming the normal hierarchy.

Oscillation Parameter	Value $\pm 1\sigma$
$\Delta m_{21}^2 \times 10^{-5}\text{eV}^2$	$7.53 \pm 0.18$
$\Delta m_{32}^2 \times 10^{-3}\text{eV}^2$	$2.453 \pm 0.033$
$\sin^2(\theta_{12})$	$0.307 \pm 0.013$
$\sin^2(\theta_{13})$	$2.20 \pm 0.07 \times 10^{-2}$
$\sin^2(\theta_{23})$	$0.546 \pm 0.021$
$\theta_{12}$ °	$33.647 \pm 0.014$
$\theta_{13}$ °	$8.530 \pm 0.002$
$\theta_{23}$ °	$47.639 \pm 0.021$
$\delta_{CP}$ °	$244.8^{+36.0}_{-28.8}$

are created when cosmic rays interact with atomic nuclei in the Earth's atmosphere. Accelerator experiments also measure these two parameters. The sign of  $\Delta m_{32}^2$  is not yet known, leading to two possible mass hierarchies:  $m_1 < m_2 < m_3$  (normal hierarchy) or  $m_3 < m_1 < m_2$  (inverted hierarchy).  $\theta_{13}$  is determined by using short baseline reactor antineutrino experiments. Table 2.1 outlines the current best global fit results quoted by the particle data group (PDG), assuming the normal hierarchy [37].

### 2.3.1 Reactor antineutrinos

Nuclear reactors have existed on Earth since 1942 when the Chicago Pile-1 reactor was built by Enrico Fermi. These reactors are designed to generate huge amounts of energy but they are useful to the particle physics community as they emit large quantities of antineutrinos. The antineutrinos are the product of nuclear fission reactions that take place inside the reactor core. This mechanism is described in more detail in Chapter 6.

Nuclear reactors act as a consistent antineutrino source with a fixed location. The antineutrinos are initially produced with pure electron flavour and thus disappearance analyses can be developed to measure the oscillation parameters. The electron antineutrino survival probability can be evaluated using Equation 2.13 to give

$$P_{\bar{\nu}_e \rightarrow \bar{\nu}_e} = 1 - \cos^4(\theta_{13}) \sin^2(2\theta_{12}) \sin^2\left(\frac{\Delta m_{21}^2 L}{4E}\right) \\ - \sin^2(2\theta_{13})(\cos^2(\theta_{12}) \sin^2\left(\frac{\Delta m_{31}^2 L}{4E}\right) + \sin^2(\theta_{12}) \sin^2\left(\frac{\Delta m_{32}^2 L}{4E}\right)). \quad (2.35)$$

Figure 2.3 shows the survival probability described in Equation 2.35 evaluated as a function of the baseline,  $L$ , for antineutrinos with an energy of 1.8 MeV. Outlined in the figure are the contributions from the two terms in Equation 2.35, informing the desired distances away from the reactor core for short baseline and long baseline reactor antineutrino experiments.

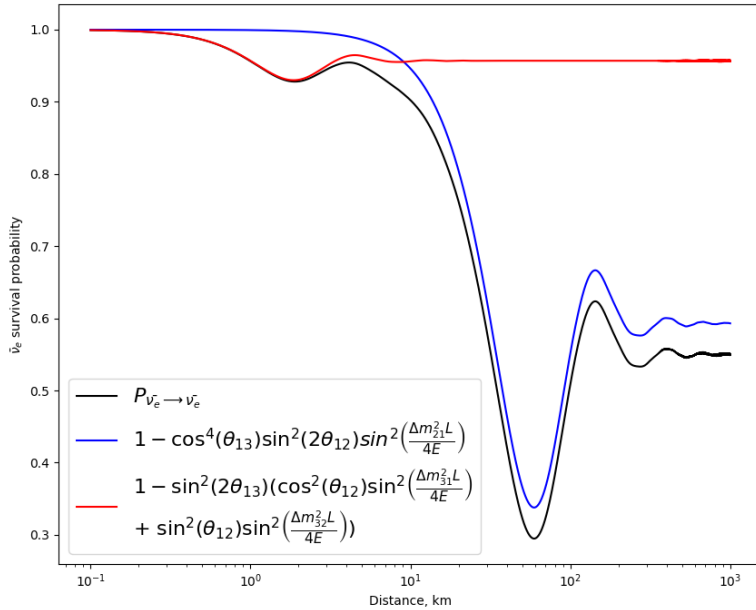


Figure 2.3: The  $\bar{\nu}_e$  survival probability as a function of oscillation baseline. The oscillation parameters as shown in Table 2.1 are used while the probability is integrated over an energy range corresponding to reactor antineutrino energies. The two terms in Equation 2.35 are also shown.

### 2.3.1.1 Short baseline reactor experiments

Reactor antineutrino experiments that aim to measure the first oscillation minimum are the short baseline reactor antineutrino experiments. These detectors are typically placed at distances of 1-2 km away from the nuclear reactor core and are best placed to measure  $\theta_{13}$ . At these baselines and with neutrinos with energies on the MeV scale the observation

that  $\frac{\Delta m_{21}^2 L}{4E} \ll 1$  is made leading to Equation 2.35 being dominated by the  $\sin^2(2\theta_{13})$  term, as shown in Figure 2.3. The antineutrino flux can be measured as a function of  $\frac{L}{E}$  and  $\sin^2(2\theta_{13})$  extracted. At the time of writing, the Daya Bay experiment reports the most precise measurement of  $\sin^2(2\theta_{13}) = 0.0856 \pm 0.0029$  [38].

### 2.3.1.2 Long baseline reactor experiments

Experiments that measure the second (and subsequent) oscillation minimum are the long baseline reactor experiments. These experiments are typically located at baselines of the order of 100 km. Figure 2.3 shows that at these longer baselines the first term in Equation 2.35 dominates and as such these experiments are most sensitive to  $\Delta m_{21}^2$  and, to a lesser extent,  $\theta_{12}$ . The KamLAND experiment currently has the most precise measurement of  $\Delta m_{21}^2 = 7.54^{+0.21}_{-0.20} \times 10^{-5} \text{ eV}^2$  [36].

SNO+ will make a competitive measurement of  $\Delta m_{21}^2$  using reactor antineutrinos, as described in later chapters of this thesis. The analysis is performed by measuring the energy of detected antineutrino events and extracting the value of  $\Delta m_{21}^2$  that best describes the data using Equation 2.35. Experiments such as SNO+ are statistically limited and also do not have sufficient energy resolution to fully resolve the fast oscillation features in Equation 2.35, caused by the  $\Delta m_{3x}^2$  terms. Therefore, these sine terms can be averaged over to give an approximated  $\bar{\nu}_e$  survival probability

$$P_{\bar{\nu}_e \rightarrow \bar{\nu}_e} \approx 1 - \frac{1}{2} \sin^2(2\theta_{13}) - \cos^4(\theta_{13}) \sin^2(2\theta_{12}) \sin^2 \left( \frac{\Delta m_{21}^2 L}{4E} \right). \quad (2.36)$$

Figure 2.4 shows the  $\bar{\nu}_e$  survival probability as calculated by Equations 2.35 and 2.36 as a function of  $\bar{\nu}_e$  energy for a baseline of 240 km. It is clear that Equation 2.36 correctly approximates the slow oscillation, dominated by  $\Delta m_{21}^2$ , while smoothing out the fast oscillation that is not resolvable in SNO+.

### 2.3.1.3 Average oscillation probability

As was seen in Section 2.2 the oscillation probability of a neutrino is dependent on the distance,  $L$ , that the neutrino has travelled. The distance travelled is well known for the case of neutrinos produced by a known source, as shown for those produced in nuclear reactors. However, not all neutrino sources are at a fixed location. Geoneutrinos are the product of radioactive decay in the Earth's mantle and crust and can be produced anywhere inside these two regions of the Earth.

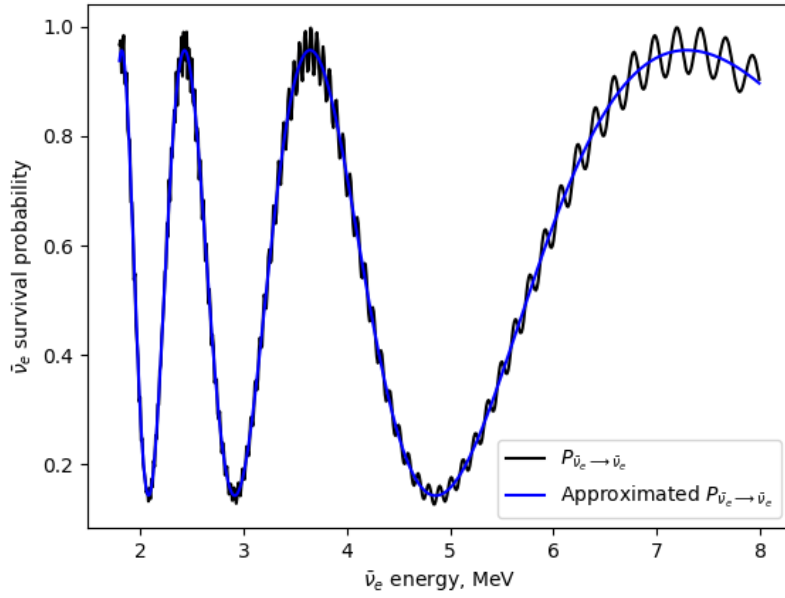


Figure 2.4: The  $\bar{\nu}_e$  survival probability as a function of  $\bar{\nu}_e$  energy. The oscillation baseline is 240 km. The complete probability as described in Equation 2.35 is shown alongside the approximated probability as described in Equation 2.36. The terms involving  $\Delta m_{3x}^2$  are averaged over to leave only the slow oscillations, dominated by  $\Delta m_{21}^2$ .

The oscillation probability for neutrinos with many unknown baselines can be accounted for by averaging the  $\sin^2\left(\frac{\Delta m_{xy}^2 L}{4E}\right)$  terms. This leads to an average survival probability

$$\langle P_{\bar{\nu}_e \rightarrow \bar{\nu}_e} \rangle \approx 1 - \frac{1}{2}(\cos^4(\theta_{13}) \sin^2(2\theta_{12}) + \sin^2(2\theta_{13})), \quad (2.37)$$

which has no dependence on any  $\Delta m_{xy}^2$  terms.

### 2.3.2 Atmospheric and solar neutrinos

While nuclear reactors are an example of a human-made antineutrino source, there are many natural sources of neutrinos. Stars, such as our own Sun, produce energy via nuclear fusion reactions. These reactions also serve as a source of pure electron neutrinos and antineutrinos. The neutrinos then travel from the Sun to the Earth where they can be detected. The oscillation of neutrinos produced in the solar core as they travel towards the surface of the Sun are heavily impacted by matter effects due to the large and varying electron density.

The distance from the Earth to the Sun is approximately  $1.5 \times 10^6$  km. At this

large baseline for neutrinos with energies of the order of MeV, the electron antineutrino survival probability is dominated by terms involving  $\Delta m_{21}^2$  and  $\theta_{12}$ . Therefore experiments detecting solar neutrinos are complementary to long baseline reactor experiments. A joint fit combining results from KamLAND and solar neutrino experiments results in the precise measurement of  $\sin^2(\theta_{12}) = 0.307^{+0.013}_{-0.012}$  [39].

Another important source of naturally generated neutrinos are those produced in the Earth's atmosphere. These atmospheric neutrinos are the result of interactions between cosmic rays and nuclei in the atmosphere. Cosmic rays are typically made up of protons which produce hadronic showers when they interact with the atmospheric nuclei. Of particular importance in these hadronic showers (and subsequent decays) are the production of a large amount of pions. The pions will decay into muons and muon neutrinos with the muons in turn decaying to electrons and electron neutrinos as

$$\begin{aligned}\pi^- &\rightarrow \mu^- + \bar{\nu}_\mu, & \pi^+ &\rightarrow \mu^+ + \nu_\mu, \\ \mu^- &\rightarrow e^- + \bar{\nu}_e + \nu_\mu, & \mu^+ &\rightarrow e^+ + \nu_e + \bar{\nu}_\mu.\end{aligned}\tag{2.38}$$

The neutrinos produced by the interactions in 2.38 have energies in the range of 100 MeV to 100 GeV [40]. It can be seen from the interactions that the ratio  $\nu_\mu : \nu_e$  is approximately 2 : 1 and thus neutrino oscillation is inferred by experiments that observe a different ratio. The energy and baselines associated with atmospheric neutrinos lead to sensitivity to  $\Delta m_{32}^2$  and  $\theta_{23}$ . Super-Kamiokande currently reports the most precise measurement of  $\Delta m_{32}^2 = 2.50^{+0.13}_{-0.20} \times 10^{-3} \text{ eV}^2$  and  $\sin^2(\theta_{23}) = 0.588^{+0.031}_{-0.064}$  for the normal hierarchy via detection of atmospheric neutrinos [41].

### 2.3.3 Accelerator neutrinos

The distance over which a neutrino travels from the source to detection is a key parameter in any oscillation analysis. For this reason, multiple human-made neutrino beams are in use around the world. These neutrino beams are produced by first generating a proton beam and directing this beam on to a target that is normally made of a material such as graphite [42]. This creates a hadronic shower and neutrinos are produced in the decays of pions and muons, as in 2.38. Artificial beams are advantageous when compared to atmospheric neutrinos as magnetic fields can be used to select muons and pions with a given charge leading to almost pure beams (at source) of neutrinos or antineutrinos.

Accelerator based experiments usually involve two detectors: a detector near the source and a detector far away from the source. This allows for a flux measurement at the

two detectors, each with their own distance from the source, and oscillation parameters extracted. The far detectors are typically placed at distances of 100 - 1000 km from the neutrino beam source with neutrino energies in the GeV range. This leads to accelerator based experiments having sensitivity to  $\Delta m_{32}^2$  and  $\theta_{23}$ . The T2K experiment has the most precise measurement of  $\Delta m_{32}^2 = (2.45 \pm 0.07) \times 10^{-3}\text{eV}^2$  and  $\sin^2(\theta_{23}) = 0.53^{+0.03}_{-0.04}$  [43], providing better sensitivity than atmospheric neutrino experiments.

The ability to run a neutrino beam in either neutrino or antineutrino mode means that accelerator based experiments can measure  $\delta_{CP}$ . A non zero value of  $\delta_{CP}$  may enhance neutrino or antineutrino oscillation and therefore the detection of both particles from the same source allows for a measurement to be made. The most precise measurement is courtesy of the T2K experiment with  $\delta_{CP} = 1.40^{+0.22}_{-0.18} \text{ rad}$  [43].

## 2.4 Neutrino mass

Two of the major unanswered questions in neutrino physics are the origin and absolute scale of the neutrino mass. It was shown in Section 2.2 that neutrino oscillation is governed by the difference of the square of the masses and therefore the neutrino mass cannot be discerned from oscillation experiments alone. Furthermore, the exact mechanism by which neutrinos gain their mass is not well understood.

### 2.4.1 Mass mechanisms

The SM describes the way in which fermions gain mass using the Higgs mechanism [14]. Particles gain mass when their left-handed and right-handed chiral components interact with the Higgs field. In the SM Lagrangian, the general mass term for a particle field  $\Phi$  is

$$\mathcal{L}_m^D = -m_D(\bar{\Phi}_R\Phi_L + \bar{\Phi}_L\Phi_R), \quad (2.39)$$

where  $L$  and  $R$  denote the left and right chiral components of the particle field. The mass of the particle,  $m_D$ , is given by a measure of coupling to the Higgs field for the particle,  $g$ , and the vacuum expectation of the Higgs field,  $v$ , as

$$m_D = \frac{gv}{\sqrt{2}}. \quad (2.40)$$

Equation 2.39 shows that there must be both left-handed and right-handed chiral states of a particle for it to gain mass via this mechanism. This is incompatible with the knowledge that only left-handed neutrinos couple to the weak force. A small extension to the SM can

be made to introduce right-handed neutrinos which only interact via gravity [44]. This extension would allow neutrinos to get their mass via the Higgs mechanism and provides an explanation for why right-handed neutrinos have not been observed.

This extension to the SM treats neutrinos as “Dirac” particles, that is, the neutrino and antineutrino are distinct particles. However, this is not the only possible explanation for the origin of neutrino mass. Ettore Majorana proposed that some particles may obey

$$\begin{aligned}\Phi^c &= \Phi \\ \Phi^c &= -i\gamma^2\Phi^*\end{aligned}\tag{2.41}$$

where  $\Phi^c$  is the charge conjugate of the particle field and  $\gamma^2$  is a  $\gamma$  matrix. Since  $\Phi^*$  and  $\Phi$  have opposite charge, Equation 2.41 is only valid for neutral particles. The neutrino is therefore a good candidate for a Majorana particle as it is the only neutral fermion. It can be shown that  $\Phi^c$  has opposite chirality to  $\Phi$ , that is,  $\Phi_R = (\Phi_L)^c$  [21].

Applying the Majorana condition in Equation 2.41 to the SM Lagrangian defined in Equation 2.39 yields

$$\mathcal{L}_m^L = -m_L(\bar{\Phi}_L^c\Phi_L + \bar{\Phi}_L\Phi_L^c).\tag{2.42}$$

In this equation  $m_L$  is the Majorana mass of the left-handed neutrino. The consequence of Equation 2.42 is that there is no longer a requirement for additional right-handed neutrinos to exist. This is because the neutrino and antineutrino are not distinct in this mechanism, the neutrino is its own antiparticle, and this leads to left-handed/right-handed coupling as required for mass generation.

#### 2.4.2 $0\nu\beta\beta$

Current generation neutrino experiments are embarking on searches for the neutrinoless double beta decay ( $0\nu\beta\beta$ ) process as a method to determine if neutrinos are Majorana in nature. In a standard  $\beta$  decay, a neutron (proton) is converted into a proton (neutron) inside an atomic nucleus with a electron (positron) and electron antineutrino (neutrino) emitted. This can be summarised for  $\beta^-$  decay in terms of the atomic mass,  $A$ , and atomic number,  $Z$ , as



It is possible for some atomic nuclei to undergo a double beta decay ( $2\nu\beta\beta$ ), in the case where a single beta decay is energetically forbidden. This can occur if the masses of the daughter nucleus and electron is larger than that of the parent nucleus. A double beta decay is summarised as

$${}^A_Z X \rightarrow {}^A_{Z+2} X + 2e^- + 2\bar{\nu}_e. \quad (2.44)$$

Such a process was first proposed by M. Goeppert-Mayer [45] and it has been observed in fourteen different isotopes [46].  $2\nu\beta\beta$  is an incredibly rare process and typically has a half life that is of the order of  $10^{18} - 10^{21}$  years.

It was proposed by W. H. Furry that it would be possible to have a double beta decay whereby no neutrinos are emitted if the neutrino is a Majorana particle [47]. This process is known as neutrinoless double beta decay ( $0\nu\beta\beta$ ) and summarised in the same form as 2.43 and 2.44 is

$${}^A_Z X \rightarrow {}^A_{Z+2} X + 2e^- . \quad (2.45)$$

This is a lepton number violating process and as such would be another indication of BSM physics. The Feynman diagrams for  $2\nu\beta\beta$  and  $0\nu\beta\beta$  are shown in Figure 2.5. In  $0\nu\beta\beta$  the two electrons are produced via the exchange of a light Majorana neutrino.

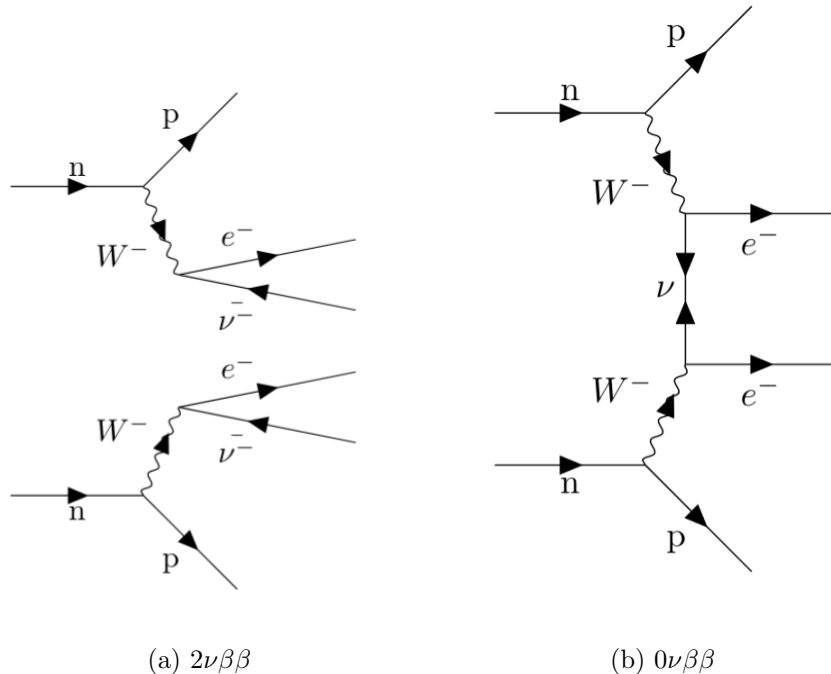


Figure 2.5: The Feynman diagrams for  $2\nu\beta\beta$  and  $0\nu\beta\beta$ .  $0\nu\beta\beta$  proceeds by exchange of a light Majorana neutrino.

The half-life of  $0\nu\beta\beta$  is directly proportional to the effective Majorana mass,  $\langle m_{\beta\beta} \rangle$ . For the case of light Majorana neutrino exchange, the half-life is

$$(\tau_{\frac{1}{2}}^{0\nu\beta\beta})^{-1} = G_{0\nu} |M_{0\nu}|^2 \langle m_{\beta\beta} \rangle^2, \quad (2.46)$$

where  $G_{0\nu}$  is a phase space factor and  $M_{0\nu}$  is the nuclear matrix element, specific to the given  $0\nu\beta\beta$  isotope [48]. The effective Majorana mass for electron neutrinos is

$$m_{\beta\beta} = \sum_{i=1}^3 U_{ei}^2 m_i, \quad (2.47)$$

where  $U_{ei}$  are elements of the PMNS matrix defined in Equation 2.4.

Equation 2.46 shows that if neutrinos are Majorana particles and  $0\nu\beta\beta$  is observed then the effective Majorana mass can be measured. It is important to note that the nuclear matrix element is a large source of uncertainty when determining the  $0\nu\beta\beta$  half life due to its difficult calculation. There are multiple methods that vary significantly [49] and therefore it is vital that any  $0\nu\beta\beta$  results specify the matrix element used. Another source of uncertainty is the unknown neutrino mass hierarchy. The impact of the mass hierarchy can be seen in Figure 2.6, where the effective Majorana mass is shown as a function of the lightest neutrino mass. It is clear that the allowed phase space takes a different form depending on the neutrino mass hierarchy. Also shown in Figure 2.6 are the current best limits on  $m_{\beta\beta}$ , set by the KamLAND-Zen 800 experiment [29]. The results are shown as a band reflecting the use of various matrix elements. KamLAND-Zen 800 uses  $^{136}\text{Xe}$  as the candidate isotope, the CUORE experiment has the best limit on  $m_{\beta\beta}$  for  $^{130}\text{Te}$  [30].

The experimental signature for  $0\nu\beta\beta$  is the observation of two electrons with the sum of their energies equal to the double beta decay endpoint. As there are no neutrinos emitted in this decay, there is no missing energy and all of the available energy is carried by the electrons. The main irreducible background to this search is the  $2\nu\beta\beta$  events as this is the dominant decay process. Figure 2.7 shows the predicted energy spectrum for  $2\nu\beta\beta$  and  $0\nu\beta\beta$  events. The  $2\nu\beta\beta$  events form a continuous energy spectrum, like that of single beta decay, due to the neutrinos carrying away some of the available energy.  $0\nu\beta\beta$  events manifest as a  $\delta$  peak at the isotope's endpoint (Q value). Experimentally the peak is not  $\delta$  like but a narrow peak due to the energy resolution of a detector.

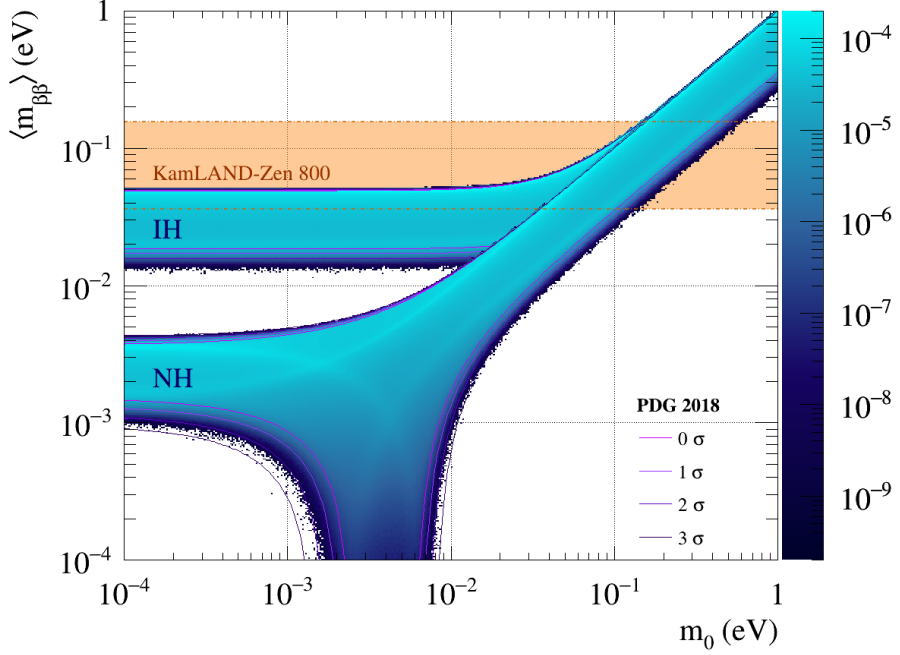


Figure 2.6: The effective Majorana mass as a function of the lightest neutrino mass. The phase space differs for the normal hierarchy (NH) and inverted hierarchy (IH). The orange band represents the current best limits on  $m_{\beta\beta}$  from KamLAND-Zen 800 [29], reflecting the uncertainty in the nuclear matrix element. This plot is generated using code written by M. Nirkko.

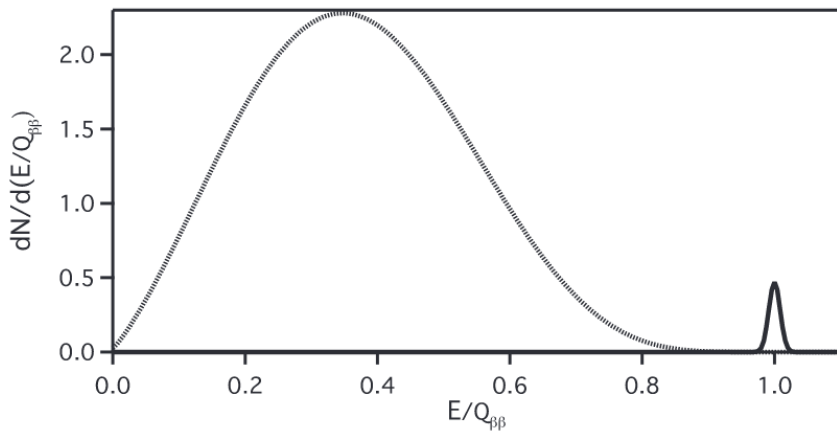


Figure 2.7: The experimental signature of  $0\nu\beta\beta$ . The  $0\nu\beta\beta$  events form a narrow peak at the Q value of the isotope of choice. The large spectrum below the Q value is the  $2\nu\beta\beta$  background. Figure taken from [48].

## 2.5 Future neutrino experiments

The current generation of neutrino experiments have provided good insights into the parameters that govern neutrino oscillation as described in Section 2.3. The neutrino physics community is rapidly refocusing its efforts into the design, construction and commissioning of next generation neutrino experiments. These experiments are intended to measure the oscillation parameters, including the CP violating phase term, more precisely than ever before. These experiments also aim to answer some of the questions surrounding the neutrino mass such as resolving the neutrino mass ordering.

The Hyper-Kamiokande experiment is the successor to the Super-Kamiokande detector. It will be a 260 kton water Cherenkov detector viewed by approximately 40,000 photomultiplier tubes (PMTs) [4]. Additionally the neutrino beam located at J-PARC, which currently serves the T2K experiment, will be upgraded [50]. This will allow Hyper-Kamiokande to make a precise measurement of  $\delta_{CP}$  and is expected to prove or disprove CP asymmetry in neutrino mixing. Hyper-Kamiokande will also make precision measurements of the atmospheric neutrino parameters,  $\Delta m_{32}^2$  and  $\theta_{23}$ . On the other side of the Earth, DUNE is a large liquid argon time-projection chamber that is in the path of neutrinos generated at Fermilab [3]. Like Hyper-Kamiokande, DUNE will make a measurement of  $\delta_{CP}$  and also aim to resolve the neutrino mass hierarchy problem.

When considering  $0\nu\beta\beta$  experiments the accepted method of increasing the sensitivity is to increase the amount of the candidate isotope present in a detector. This is logical as the half-life of a decay is a statistical measure and therefore a larger number of atoms that can potentially undergo the decay allows for longer half-lives to be probed. There are two philosophies for achieving this: increasing candidate isotope concentration in existing detectors or building larger detectors. Experiments such as SNO+ and KamLAND-Zen take the increasing concentration approach, with KamLAND2-Zen [51] and SNO+ Phase II [52] using the same experimental hardware but with an increased loading concentration in the scintillator. Conversely, the LEGEND collaboration plans to build a larger detector and is in the transition from LEGEND-200 to LEGEND-1000 [53]. SNO+ Phase II, KamLAND2-Zen and LEGEND-1000 are projected to reach  $m_{\beta\beta}$  limits of approximately 20 meV [54].

Finally, JUNO is an example of a next generation long baseline reactor antineutrino experiment. JUNO will be a 20 kton liquid scintillator detector viewed by approximately 50,000 PMTs. Its colossal size means that even with a baseline of 53 km to the nearest

nuclear reactor it will be able to measure  $\theta_{12}$ ,  $\Delta m_{21}^2$  and  $\Delta m_{32}^2$  with a precision of at least 0.6% [55].

## 2.6 Conclusion

The detection of neutrinos with varying energy or distance through which they have travelled allows the parameters that govern neutrino oscillation to be measured. In the case of antineutrinos produced in the cores of nuclear reactors it has been shown that a detector placed of the order of 100 km away, such as SNO+, is sensitive to  $\Delta m_{21}^2$  and  $\theta_{12}$ . Additionally, the enhanced mixing of neutrinos travelling through matter is negligible for reactor antineutrinos travelling through the Earth.

## Chapter 3

# The SNO+ Experiment

### 3.1 Introduction

The SNO+ detector is a multipurpose kilo-tonne scale liquid scintillator neutrino detector. SNO+ is situated in a cavern within SNOLAB, 2 km underground in the Creighton mine outside of Sudbury, Ontario, Canada. The detector inherits much of the hardware from the Nobel prize winning experiment SNO, the predecessor to SNO+ [56]. SNO+ has a programme of four distinct phases, catagorised by the detection medium, each with broadly different physics goals. The primary purpose of the experiment is the search for  $0\nu\beta\beta$ . This search will be undertaken by loading  $^{130}\text{Te}$  into a liquid scintillator cocktail. SNO+ is also sensitive to wide range of neutrino physics including, but not limited to, the detection of reactor antineutrinos, solar neutrinos and supernova neutrinos. This chapter describes the detector hardware, data acquisition systems, event reconstruction software and an overview of the distinct phases of the experiment.

### 3.2 General overview

A drawing of the detector is shown in Figure 3.1. The detector consists of a spherical acrylic vessel (AV) with a radius of 6 m and thickness of 5.6 cm. The volume of the AV is the volume of interest for all SNO+ analyses and it is surrounded by approximately 9500 PMTs which are mounted on an icosahedral structure (PSUP) with a radius of 9 m. There is a volume of ultra-pure water (UPW) between the AV and the PSUP to reduce backgrounds from the PSUP and the PMTs themselves. The AV is supported by a net of hold-down and hold-up ropes, necessary to counteract buoyant forces due to the density of liquid scintillator. The hold up ropes were required for SNO and are installed in “belly plates” around the equator of the detector. These plates are approximately twice

as thick as the rest of the acrylic. The whole structure is submerged in a large cavity that is also filled with UPW which acts as a shield from background events produced in the surrounding rock. Above the cavity is an area known as the SNO+ deck. The deck houses critical electronics, mechanical instruments and calibration hardware. There is a clean room located on the deck (DCR) in order to provide extra cleanliness for hardware directly connected to the detector volume.

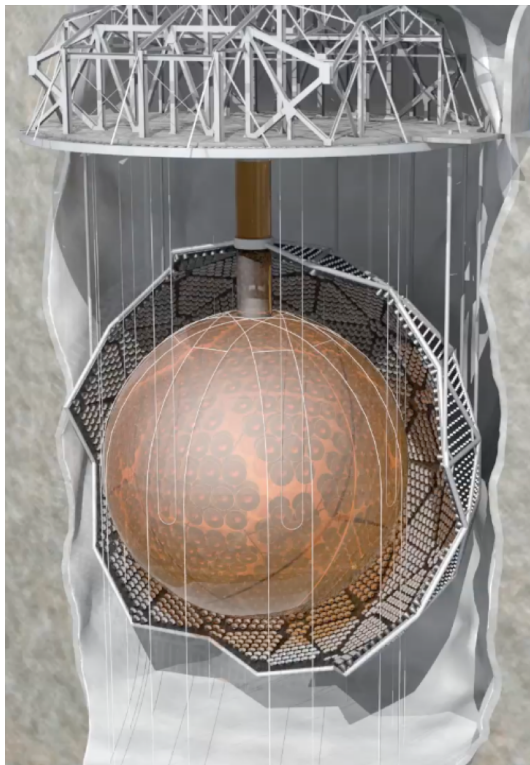


Figure 3.1: A drawing of the SNO+ detector. Taken from [28].

The AV is filled with approximately 790 tonnes of liquid scintillator. The liquid scintillator is linear alkylbenzene (LAB) and is mixed with 2,5-Diphenyloxazole (PPO) with a concentration of 2 g/L. PPO is used in the SNO+ scintillator cocktail to increase the light yield and consequently increase the number of scintillation photons per unit of energy deposited in the scintillator. The scintillator cocktail will also contain the wavelength shifter 1,4-bis(2-methylstyryl)benzene (bis-MSB), in order to produce scintillation photons that correspond to the wavelength of maximal PMT quantum efficiency. The scintillator cocktail is described in more detail in [57].

The SNO+ liquid scintillator will be loaded with approximately 4 tonnes of natural tellurium. The  $0\nu\beta\beta$  candidate isotope is  $^{130}\text{Te}$ . This isotope was chosen for its high natural abundance (34%), eliminating the need for enrichment, as well as the accessible end point of the  $0\nu\beta\beta$  decay (2.5 MeV) [58], well within the detection capabilities of SNO+.

The end point of the decay is also above many of the natural radioactive backgrounds that are present in SNO+.

### 3.3 Phases of SNO+

The experiment has four distinct running phases. The phases are catagorised by the material that is inside the AV. The first phase was the water phase, running from May 2017 to October 2018. The second phase was the partial fill phase, running from March 2020 to October 2020. The third phase is the pure liquid scintillator phase. The fourth and final phase is the tellurium loaded liquid scintillator phase.

#### 3.3.1 Water phase

The water phase was the first phase of SNO+. In this phase the AV was filled with 905 tonnes of UPW. The early period of the water phase was used to commission the data acquisition (DAQ) system and electronics. There were two main physics analyses performed in the water phase: the measurement of the  $^8\text{B}$  solar neutrino flux [59] and the search for invisible nucleon decay modes [60].

The water phase served as an opportunity to measure backgrounds from the AV, the hold-down ropes, the external water and the PMTs [60]. The optical properties of the AV and the external water were measured, as well as the PMT response [61]. The thermal neutron-proton capture cross section was also measured using a  $^{241}\text{Am}^9\text{Be}$  calibration source. The cross section was measured to be  $336.3_{-1.5}^{+1.2}$  mb with a neutron capture detection efficiency of 49% [62]. This cross section result feeds directly into the reactor antineutrino analysis in later phases of SNO+.

As SNO+ operated as a water Cerenkov detector in this phase the directional information of events was preserved and therefore a flux measurement of  $^8\text{B}$  solar neutrinos could be performed. This measurement demonstrated very low backgrounds inside the detector volume and the result was consistent with measurements performed by similar experiments [63], [64]. Invisible nucleon decay is a theorised process in which protons or neutrons can decay while depositing no visible energy in a detector like that of SNO+ [65]. The lower limit on the lifetime of protons is measured to be  $9.6 \times 10^{29}$  yr and the lifetime of bound neutrons is measured to be  $9.0 \times 10^{29}$  yr [60].

### 3.3.2 Partial fill phase

The completion of the water phase marked the beginning of a transition period where the UPW in the AV was replaced with liquid scintillator. This process was intended to run continuously until the complete volume of UPW in the AV was replaced by liquid scintillator, resulting in no planned long term periods of stable detector conditions which are necessary for physics analyses.

The COVID-19 pandemic caused the suspension of the filling activities for 7 months between March 2020 and October 2020<sup>1</sup>. The SNO+ detector took data in a configuration where the AV contained 365 tonnes of liquid scintillator which sat on top of 480 tonnes of UPW, as shown in Figure 3.2.



Figure 3.2: A photo of the SNO+ detector during the partial fill. Here the interface between the liquid scintillator and UPW is visible.

This opportunistic phase was used to refine analysis techniques used to determine important backgrounds for the  $0\nu\beta\beta$  search, as will be discussed in more detail in Section 3.3.3. A demonstration of the SNO+ antineutrino oscillation analysis was performed, as well as a demonstration of preserving directional information in liquid scintillator neutrino events [66].

### 3.3.3 Pure liquid scintillator phase

SNO+ is currently in its third major phase, the pure liquid scintillator phase. The primary objective of the pure liquid scintillator phase is to evaluate important backgrounds for the tellurium loaded phase. A crucial component of the sensitivity of a search for  $0\nu\beta\beta$  is the concentration of radioactive elements from the uranium and thorium decay chains present

---

<sup>1</sup>This setback pales in comparison when considering the devastating death toll and consequences across the world as a result of the pandemic.

in the detector. The Borexino experiment has measured background concentrations of less than  $10^{-17}$  g/g for both the  $^{238}\text{U}$  and  $^{232}\text{Th}$  decay chains [67] and SNO+ is targeting these levels or better. The optical model and detector response will be validated in this phase, using the calibration sources that are described in more detail in Chapter 4.

The pure liquid scintillator phase provides opportunities for impactful physics analyses. The physics goals include the detection of reactor antineutrinos and thus the measurement of  $\Delta m_{21}^2$  and  $\theta_{12}$ , the detection of geoneutrinos, the observation of low energy solar neutrinos and the potential observation of neutrinos from supernovae. The detection of reactor antineutrinos and the subsequent oscillation analysis will aim to resolve the current tension in the measurement of  $\Delta m_{21}^2$  by solar and reactor neutrino experiments.

### 3.3.4 Tellurium loaded liquid scintillator phase

The fourth and final major phase will begin when the natural tellurium has been loaded into the liquid scintillator. The process of adding the tellurium to the liquid scintillator will involve recirculating the existing scintillator from the AV through a tellurium processing plant, located underground at SNOLAB, which will introduce the tellurium into the scintillator in the form of telluric acid, before flowing back into the AV.

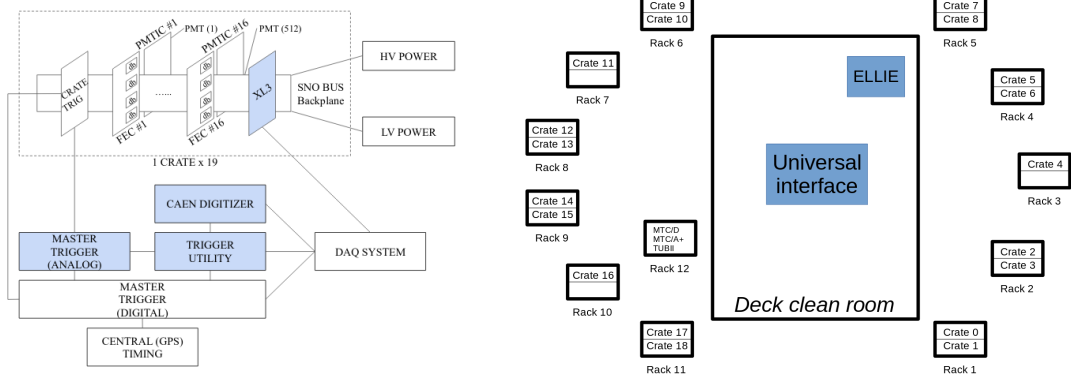
The primary objective during this fourth and final phase is the search for  $0\nu\beta\beta$ . The physics goals that were discussed in Section 3.3.3 are also applicable in this phase and will also be pursued.

## 3.4 Readout and data acquisition

The major hardware described in Section 3.2 is accompanied by the DAQ hardware. A physics event that occurs inside the detector will go through the DAQ systems such that the data is accessible for analysis. The majority of the DAQ hardware sits on the deck above the cavity where the detector is situated. Figure 3.3 outlines the major components of the SNO+ DAQ.

### 3.4.1 PMTs

The first stage of the readout are the PMTs themselves. SNO+ uses the Hamamatsu R1408 8" PMTs that were originally used in the SNO experiment [56]. During the upgrade between SNO and SNO+ approximately 75% of the PMTs that stopped operating during SNO were removed, repaired and replaced for SNO+ [28]. In the current running period of SNO+ it is observed that a small fraction of PMTs continue to fail at a rate of



(a) The major components of the readout and (b) The location of the DAQ hardware on the SNO+ deck.

Figure 3.3: A cartoon of the SNO+ readout and DAQ system describing the major components. The universal interface and ELLIE rack are used during calibration and are described in more detail in Chapter 4. Figure (a) taken from [28], adapted from [68].

approximately 6.8 per month. There are currently approximately 9200 PMTs mounted on the PSUP and pointing towards the center of the detector that are operating nominally. Additionally there are 91 PMTs that are mounted on the PSUP but facing in the opposite direction, towards the external cavity. These PMTs are used to help veto muons and any other external events that originate outside of the PSUP.

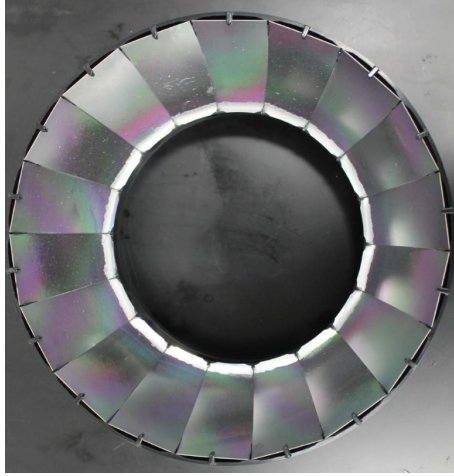


Figure 3.4: A photo of a SNO+ PMT concentrator. Taken from [69].

Each PMT is installed with a 27 cm diameter concentrator that is designed to increase the photocoverage of each PMT. The concentrators are small aluminium petals that surround the PMT, as shown in Figure 3.4. The effect of this is that the photocoverage of the detector is increased to approximately 54%. The efficiency of each PMT is a combination of the quantum efficiency and the photon collection efficiency. The efficiency of the

PMTs was measured by the SNO collaboration and is shown in Figure 3.5. The addition of bis-MSB into the liquid scintillator cocktail is motivated by the wavelength dependence of the total efficiency of the PMTs.

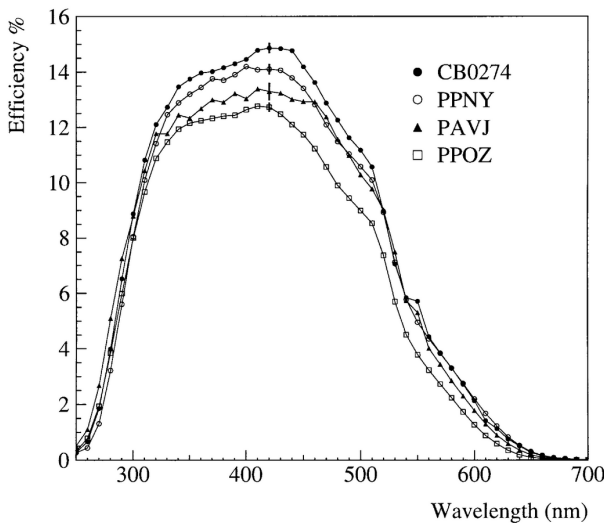


Figure 3.5: The total efficiency of the PMTs used in SNO+, as measured by the SNO collaboration [70].

### 3.4.2 DAQ chain

A signal from a PMT will travel along a 32 m long cable into a PMT Interface Card (PMTIC) located in one of 19 crates on the SNO+ deck. Each PMTIC holds four daughterboards (DBs) which process the signals from 8 PMTs each. The DBs have remotely controllable relays to toggle the PMT high voltage (HV) supply. In the event of a HV breakdown groups of 8 PMTs can be toggled on/off as required to isolate the problematic tube, allowing data collection to continue unimpeded. Each crate contains 16 PMTICs meaning that each crate handles the signals from 512 PMTs.

A DB has a discriminator for each PMT and if the amplitude of the pulse from a PMT is large enough then the discriminator will fire. The discriminator will generate two pulses; one of 100 ns length and another of 20 ns length. These different length pulses correspond to two separate physics triggers; the N100 and N20. The N100 trigger is designed to be the main trigger for SNO+. The time of flight for a photon traveling across the entire detector is approximately 86 ns and therefore all photons produced in an event at any position in the detector are able to contribute to the N100 trigger sum. The N20 trigger is designed to identify events located near the centre of the detector.

The trigger pulses are then sent to the Front End Cards (FECs) in the crate. Each

crate contains 16 FECs, corresponding to the 16 PMTICs. The FECs sum the analog pulses that are generated from each of the 32 channels per PMTIC. Each crate has a single Crate Trigger Card (CTC) which sums the resulting pulses from each of the FECs, resulting in a crate wide trigger sum.

The CTCs send their crate wide trigger sums to the Master Trigger Card / Analog (MTC/A+). There is an MTC/A+ for each physics trigger, therefore the 100 ns summed pulses and the 20 ns summed pulses are sent to different MTC/A+'s. The MTC/A+ takes the trigger sums from each of the 19 crates and sums them into a single detector wide trigger pulse. This pulse has an amplitude that is proportional to the number of PMTs that registered a hit in the 100 ns (20 ns) window. The MTC/A+ has multiple discriminators which have programmable thresholds and so each trigger signal can therefore be split into multiple gain paths. For example the N100 trigger has three distinct gain paths; the N100L, N100M and N100H, where the thresholds might be equivalent to 25, 40 and 70 PMT hits respectively.

If any discriminator threshold is crossed on any of the MTC/A+'s, the discriminator will fire and send a short 20 ns pulse to the Master Trigger Card / Digital (MTC/D). When the MTC/D receives such a pulse a global trigger (GT) is issued. This GT is sent back to all crates and the timing and charge information of each PMT that fired are digitised and stored in first-in-first-out (FIFO) buffers on the FECs. The detector wide trigger sum is also digitised by a CAEN digitiser. The GT is latched to a tick of a 50 MHz clock that is located on the MTC/D, giving a local event time. The GT is also latched to a slower 20 MHz clock which is synchronised with GPS time, to provide a global event time. After a GT is issued there is a period of 420 ns where a subsequent GT cannot be produced, even if a discriminator threshold on one of the MTC/A+'s is crossed.

The final stage of the journey through the DAQ is handled by the XL3's, a custom board designed to send data to the SNO+ data server. Each crate contains an XL3 and this board acts as the bridge between the DAQ hardware and the software. The XL3 will read the timing and charge information of each PMT that are stored on the FECs and will transfer this data to the SNO+ data server. The XL3 contains a commercial evaluation board<sup>2</sup> which utilises an onboard FPGA to read the data from the FECs and an onboard PowerPC processor to push the data to the server via Ethernet. The SNO+ event builder then pulls data from the server and organises the information into zdab files<sup>3</sup> which are available to be prepared for analysis via offline processing. The physics data is separated

---

<sup>2</sup>Xilinx ML403: [https://www.xilinx.com/support/documentation/boards\\_and\\_kits/ug080.pdf](https://www.xilinx.com/support/documentation/boards_and_kits/ug080.pdf)

<sup>3</sup>A native file type inherited from SNO.

into “runs” of hour long lengths. This segmentation is done in order to minimise the livetime lost when performing data quality checks, as discussed in Section 3.5.

### 3.5 Data quality

The data that is collected by SNO+ must be verified to be of sufficient quality to be used for analysis purposes. There are a myriad of electronic effects which can introduce artefacts in the data. All data that is collected is subjected to a set of data quality checks to decide if the data is suitable for analysis. There are approximately 50 individual checks that make up the complete data quality process. A small selection of critical checks are described here, a complete list is provided in Appendix B.

An important check is to simply determine whether all crates are online and supplying voltage to the PMTs. The crates can occasionally be temporarily offline, for example if the crate has a power supply issue. A crate being offline is not necessarily an immediate failure of the data quality checks. An offline crate can cause difficulties with event reconstruction (see Section 3.7) and low threshold analyses relying on events producing a small number of PMT hits may be impacted, but the data is still fundamentally fit for analysis.

As described in Section 3.4 the PMT timing and charge information is stored in FIFO buffers on the FEC before it is read out by the XL3’s. These buffers have 4 MB of storage, more than enough to handle typical event rates in SNO+. Occasionally the event rate can increase to well above the nominal event rate, typically caused by the breakdown of a PMT. This breakdown can either happen at the PMT itself and cause real light to be injected into the detector (wet end breakdown) or this can happen at the PMTIC which produces fake PMT signals leading to fake trigger signals (dry end breakdown). The FIFO buffers can fill up quickly if the event rate is elevated for some time. The XL3’s cannot read out the information in the buffers faster than new information is arriving, leading to a loss in data. A run is deemed unsuitable for analysis if any data is lost in this way.

A similar check is verifying that all data is correctly passed from the XL3’s to the event builder. The data is passed to the machine that runs the event builder through the internal SNO+ network, along Ethernet cables. A small interruption to the network can cause data to not be sent to the event builder, either from all of the XL3’s or only a small number of XL3’s. This means that an event may be missing entirely or may be missing data from one or more crates and thus only be partially complete. Any run during which this occurs is deemed unsuitable for analysis.

The majority of the DAQ hardware is located on the deck above the experiment cavity.

It is not uncommon for people to access the deck in order to perform routine maintenance and other detector related duties. The presence of humans performing noisy or disruptive work can introduce an increased noise rate in the detector while also producing fake events, similar to that of a dry end breakdown. All access to the deck is logged and therefore the potential deck activity can be monitored for each run. Any run where there was activity on deck is closely inspected to determine if the work performed will impact the data. As an example, a person vacuuming on deck is likely to introduce noise, while a person checking the oxygen concentration in the air is unlikely to introduce noise.

## 3.6 Software

SNO+ uses the Reactor Analysis Tool (RAT) framework for both Monte Carlo (MC) simulation and analysis of the SNO+ data [71]. RAT is a framework written in C++ that allows the simulation of the SNO+ detector using Geant4 [72] and GLG4sim [73]. The geometry of the detector including the AV, PSUP, PMTs, hold down ropes, liquid scintillator and external water is defined as a Geant4 model. RAT includes multiple event generators that can simulate a large quantity of particle interactions, such as IBD events, at any position inside the detector and with any rate. Optical photons are generated by both scintillation and Cerenkov processes and their paths through the detector are treated with a complete optical model that includes scattering, absorption and re-emission. The PMTs and DAQ/electronics are also simulated leading to a comprehensive MC simulation from event generation to data readout.

RAT contains tools and utilities to help perform analysis of both data collected by SNO+ and MC simulated data. This includes algorithms for reconstruction and event classification, utilities to extract calibration constants and tools to run data quality checks. RAT also has ROOT [74] integration to provide data management and file structures. This allows RAT to write data as ROOT TTrees that can be read in by RAT.

## 3.7 Reconstruction

### 3.7.1 Event position and time

Fundamentally the raw data collected by SNO+ is the timing and charge information from each PMT. The ability to use this data to reconstruct events accurately is critical to performing meaningful physics analyses with the data recorded by the SNO+ detector. Fiducialisation is a significant way to reject background events in SNO+ data, particularly

in the case of the  $0\nu\beta\beta$  analysis and the reactor antineutrino analysis. The ability to define a fiducial volume is dependent on the position of events within the detector to be well known. The reactor antineutrino analysis depends on identifying a neutron capture with a well known energy deposition. A good set of reconstruction algorithms are essential to estimate the position and energy of events with a small uncertainty.

The algorithms used to reconstruct events in liquid scintillator are contained within RAT. The first two quantities to reconstruct are the position and time of an event vertex, as these are used as inputs into the energy reconstruction algorithm. The position and time reconstruction is performed using a maximum likelihood algorithm, *PositionTime-Likelihood* [75].

In any given event a number of PMTs will register a signal ( $N_{\text{hits}}$ ). For each hit PMT the residual hit time can be calculated, defined as

$$t_{\text{res}} = t_{\text{PMT}} - t_{\text{TOF}} - t_{\text{fit}}, \quad (3.1)$$

where  $t_{\text{PMT}}$  is the hit time recorded by the PMT,  $t_{\text{TOF}}$  is the photon time of flight from the reconstructed event vertex to the PMT and  $t_{\text{fit}}$  is the time that the event occurred.  $t_{\text{PMT}}$  and  $t_{\text{TOF}}$  are values that are PMT specific, while  $t_{\text{fit}}$  is a single global value that applies to all PMTs.  $t_{\text{TOF}}$  is calculated by assuming that photons travel in a straight line from the point at which they are created to the PMT that detects them, accounting for the refractive indices of the scintillator, acrylic and water that the photon travels through.

The *PositionTimeLikelihood* algorithm starts by calculating the residual hit time. For a given starting position and  $t_{\text{fit}}$  the log-likelihood is computed as

$$\log(\mathcal{L}) = \sum_{i=0}^{N_{\text{hits}}} \log(P(t_{\text{res}}^i)), \quad (3.2)$$

where  $P(t_{\text{res}}^i)$  corresponds to the probability of  $t_{\text{res}}$  being reported by PMT  $i$ . The probability is defined by a probability density function (PDF) that exists in the RAT database. The PDF is generated from MC simulated data which includes the modelling of the detector geometry, the optical model and the timing response of the scintillator. The Powell method [76] is then used to find the vertex and event time that maximise the likelihood expression.

### 3.7.2 Event energy

The energy of an event is equally as important a reconstructed quantity as the position as it allows for identification and selection of specific interactions that SNO+ has sensitivity

to. The reconstruction algorithm used to estimate the event energy is *EnergyRThetaFunctional* [77]. When an interaction occurs in the SNO+ liquid scintillator some amount of scintillation photons are produced. The charge information that is recorded by the PMTs is not adequate to determine the number of photoelectrons produced at the cathode of the PMT. To accommodate this the  $N_{\text{hits}}$  of an event is used as an approximation for the number of photoelectrons.  $N_{\text{hits}}$  is the number of PMTs that crossed threshold in an event and subsequently have their time and charge information read out.

The  $N_{\text{hits}}$  of an event is an approximately linear function of energy at low energy but the linearity weakens at higher energies, as shown in Figure 3.6. This is due to the increased probability that PMTs will have multiple photons incident upon them, which cannot be determined using the PMT charge information. *EnergyRThetaFunctional* applies a correction factor to the  $N_{\text{hits}}$ , as a function of position, to correct for the multi-hit PMTs in an event. The corrected  $N_{\text{hits}}$  is then converted to an energy via a factor that is determined from MC, as shown in Figure 3.6. A comprehensive description can be found in [77].

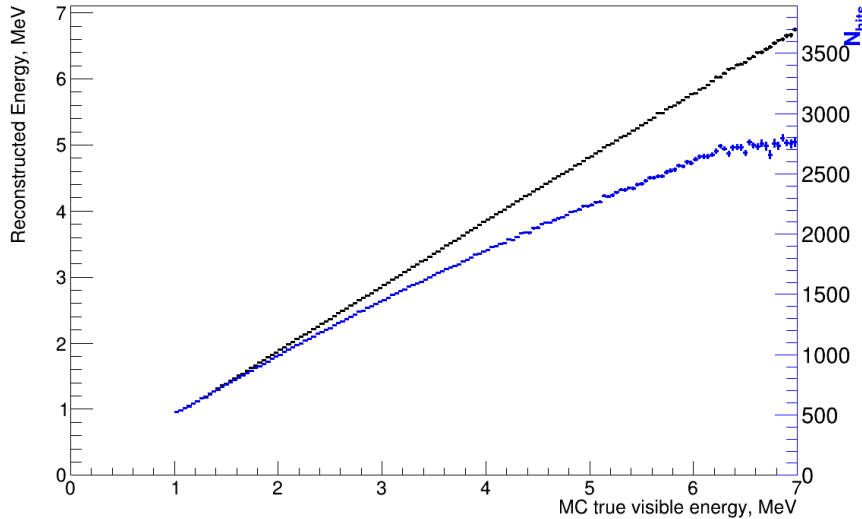


Figure 3.6: The  $N_{\text{hits}}$  and reconstructed energy of  $^{13}\text{C}(\alpha, n)^{16}\text{O}$  prompt events simulated in the SNO+ detector as a function of the MC true energy. The non linearity of the  $N_{\text{hits}}$  of events at higher energies is visible, as is the restoration of linearity in the reconstructed energy.

# Chapter 4

## Calibration

### 4.1 Introduction

Calibration of observable quantities in an experiment such as SNO+ is crucial to the production of meaningful physics results. Calibration of the SNO+ detector is a task which has multiple different inputs. This chapter will give a brief and general overview of the methods and systems designed for optical and energy calibration. Greater depth will be given to the optical calibration of the detector, with particular focus on the monitoring of optical attenuation.

As discussed in Chapter 3 the energy of an event in SNO+ is reconstructed by applying a corrective factor to the  $N_{\text{hits}}$  of the event. This factor is determined by analysis data from the various calibration sources. While all analyses use reconstructed energy as a parameter, it is particularly critical for the  $0\nu\beta\beta$  analysis.  $0\nu\beta\beta$  manifests as an event with an energy corresponding to the  $^{130}\text{Te}$   $0\nu\beta\beta$  endpoint. The energy response of the detector must therefore be well understood and calibrated in order to confidently report any potential  $0\nu\beta\beta$  signal. Accurate energy calibration is also required in spectral analyses, such as the reactor antineutrino oscillation analysis. These analyses use the shape of the prompt energy distribution to extract physical parameters and inaccurate energy calibration significantly reduces the sensitivity of these analyses. Additionally, the antineutrino analysis requires the selection of IBD candidate events using the well known energy of a neutron capture on a free proton. Good energy calibration is therefore crucial to identifying such events.

The position and time of an event is reconstructed by maximising a likelihood function using the residual hit time of the PMTs. As per Equation 3.2 the hit time recorded by each PMT is a parameter in the residual hit time calculation. A PMT that is not calibrated,

or poorly calibrated, may give a hit time that does not accurately reflect the true hit time and impact the accuracy of the position and time reconstruction. It is therefore vital that PMTs are well calibrated when considering their timing.

The optical model of the detector is a fundamental input when simulating the detector. Optical photons that are produced during particle interactions may undergo absorption (and re-emission) or scattering before they reach the PMTs. The photons may also reflect off the AV or the PMTs.

## 4.2 Calibration sources

The SNO+ experiment uses a large range of different calibration sources to fully characterise the detector response. Table 4.1 outlines the main calibration systems that can be used within SNO+. The calibration sources are broadly split into three categories: optical calibration, timing calibration and energy calibration. Optical calibration sources are used to monitor and measure the optical properties of the detector. This includes the attenuation, both absorption and scattering, in the scintillator, acrylic and external water. The sources that are used for these measurements are the in-situ light injection sources (AMELLIE, SMELLIE) and the deployed laserball. Sources such as the laserball and TELLIE are used to characterise the timing response of the PMTs and determine electronic delays.

Radioactive sources are deployed in the scintillator and external water to determine the energy response of the detector by using known decays and their associated energy depositions. The radioactive sources can be grouped into tagged sources and untagged sources. The tagged sources use the isotopes  $^{16}\text{N}$  and  $^{46}\text{Sc}$ . These nuclei undergo  $\beta$  decays which are detected by a PMT located inside the source. The  $\gamma$ s that leave the source and enter the scintillator can be efficiently selected by requiring a coincidence with this external tagged event. The  $^{241}\text{Am}^{9}\text{Be}$  source produces a  $\gamma$  and a neutron which lead to a distinct pair of prompt and delayed signals allowing efficient tagging of  $^{241}\text{Am}^{9}\text{Be}$  events. The  $^{48}\text{Sc}$ ,  $^{137}\text{Cs}$  and  $^{57}\text{Co}$  are  $\gamma$  producers and are untagged sources. The  $\gamma$ s that enter the detector are selected using solely positional and energy constraints.

### 4.2.1 ELLIE

The Embedded LASER/LED Light Injection Entity (ELLIE) is an overall name for three different in-situ light injection systems: AMELLIE (attenuation), SMELLIE (scattering) and TELLIE (timing). ELLIE consists of multiple light injection sites located on the

Table 4.1: The various calibration sources available to be used in the SNO+ detector.

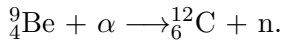
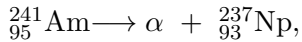
Source	Type	Calibrated quantity	Energy / Wavelength	Particle
$^{241}\text{Am}^9\text{Be}$	Deployed	Energy	2.2, 4.4 MeV	$\gamma$ , neutron
$^{16}\text{N}$	Deployed	Energy	6.1 MeV	$\gamma$
$^{46}\text{Sc}$	Deployed	Energy	2.0 MeV	$\gamma$
$^{48}\text{Sc}$	Deployed	Energy	3.3 MeV	$\gamma$
$^{137}\text{Cs}$	Deployed	Energy	0.66 MeV	$\gamma, \beta$
$^{57}\text{Co}$	Deployed	Energy	0.14 MeV	$\gamma$
AMELLIE	Light injection	Optical attenuation	503 nm	Optical photon
SMELLIE	Light injection	Optical scattering	375-700 nm	Optical photon
TELLIE	Light injection	PMT timing	503 nm	Optical photon
Laserball	Deployed	PMT timing, optical attenuation	337 nm	Optical photon

PSUP providing full detector coverage as shown by Figure 4.1. The systems use optical sources (either LEDs or a laser) that are coupled to optical fibres. These fibres terminate at the injection sites on the PSUP and inject light directly into the detector.

The three distinct modules of ELLIE serve different purposes as calibration sources. AMELLIE and SMELLIE are used to monitor and measure the optical properties of the scintillator while TELLIE is used to calibrate the timing response of the PMTs. AMELLIE and TELLIE utilise LEDs while SMELLIE uses lasers.

### 4.3 Energy calibration with the $^{241}\text{Am}^9\text{Be}$ source

Of particular importance to the detection of antineutrino events is the  $^{241}\text{Am}^9\text{Be}$  (AmBe) source. The  $^{241}\text{Am}$  undergoes an  $\alpha$  decay and the resulting  $\alpha$  particle is absorbed by the  $^9\text{Be}$  to produce a neutron, via the processes:



In approximately 60% of cases the carbon is produced in an excited state and immediately de-excites by emitting a 4.4 MeV  $\gamma$ . The neutron travels into the detector and undergoes capture on hydrogen that emits a 2.2 MeV  $\gamma$ . The 4.4 MeV and 2.2 MeV  $\gamma$ s constitute a prompt and delayed signal respectively. A coincidence search can be performed to reject backgrounds and select a high purity sample of these two energy depositions. The neutron can also capture on carbon and produce a 4.9 MeV  $\gamma$ . The cross section of the

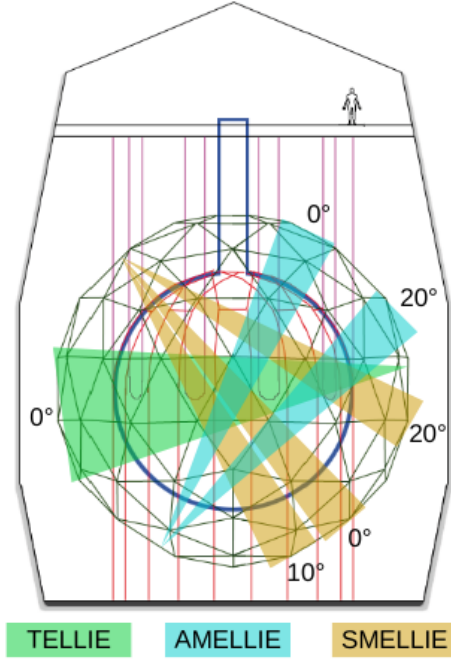


Figure 4.1: A schematic of the different ELLIE systems. The angle of the beams relative to the centre of the detector is shown, that is, a beam with an angle of  $0^\circ$  points at the centre of the detector. Figure taken from [28], adapted from [78].

capture on carbon is much smaller than that of capture on hydrogen and therefore events are typically selected using the delayed  $\gamma$  from neutron capture on hydrogen. Neptunium has a half-life of over 2 million years leading to a negligible contribution to the source activity.

The AmBe source is well suited for energy calibration when considering the antineutrino analyses, as the delayed neutron capture events from the source are exactly like those of the delayed signal for IBD events. The prompt and delayed events from the source provide calibration points at their respective energies. The delayed event is also used to measure the neutron detection efficiency [62] which is used in the prediction of expected number of reactor IBD events.

The source can be deployed and moved around such that it can sit at almost any position inside the detector medium. This allows the energy to be calibrated as a function of position, reducing the systematic uncertainties associated with energy reconstruction. Consequently the neutron detection efficiency can be measured as a function of position, further improving the reactor IBD prediction. The source is deployed in the detector via a system of ropes. There is a single rope controlling the motion of the source in the vertical axis and two side ropes which manipulate the source in the horizontal axes.

## 4.4 Timing calibration

Event reconstruction in SNO+ is performed using the times that individual PMTs are hit. The hit time of a PMT will include electronic and cable delays and these can alter the time reported by a PMT, introducing biases in event reconstruction. Poor event reconstruction results in a diminished sensitivity to  $0\nu\beta\beta$  and reactor antineutrino detection as there are larger uncertainties when considering the fiducial volume used in these analyses. Therefore it is important to calibrate PMT hit times to account for readout delays.

### 4.4.1 TELLIE

TELLIE is the timing module of ELLIE and is used to provide a timing calibration of the PMTs. TELLIE consists of 96 optical fibres that are coupled to LEDs at one end and terminated at different injection points around the PSUP at the other. The fibres are directed towards the centre of the detector and have a wide beam profile (approximately 22° half angle). This serves the purpose of having photon coverage across as many PMTs by each fibre as possible.

TELLIE is designed to provide an in-situ timing calibration for the PMTs. TELLIE data is collected as described in Section 4.5.2.2. The timing calibration is performed by comparing the time that a PMT registers a hit and the time of the injection of light into the detector, accounting for the photon time of flight from the fibre end to the PMT. Using this technique a calibration of the order of 0.1 ns per PMT can be achieved [28], whereby a calibration constant is calculated for each PMT and applied to events at analysis level.

#### 4.4.1.1 Dry end hardware

AMELLIE and TELLIE share the exact same dry end hardware. The majority of the hardware is located in the DCR. The dry end electronics for each channel are situated in a dedicated rack, as in Figure 4.2. The rack contains a power box (top) and a control box (middle). The remaining 13 boxes house the electronics for each channel, with eight channels per box. The AMELLIE channels are located in box 13 at the top of the rack while the remaining 12 boxes house the TELLIE channels.

Each box in the rack contains the electronic hardware for eight channels. Figure 4.3 shows that there are three main components: the driver board, the LED and the PIN board.

Four of the eight LEDs currently installed in AMELLIE have a peak emission wave-



Figure 4.2: A photo of the TELLIE rack in the DCR. The power box, control box and an electronics housing box are identified.

length of 505 nm. The remaining four have recently been replaced with those with a peak emission wavelength of 403 nm. The timing profile is approximately Gaussian distributed with a width of 3 ns. The option remains open to replace the AMELLIE LEDs with those of different wavelengths and the motivation for shorter wavelengths is described in more detail in Section 4.6. In an effort to maximise the optical transmittance between the LED and the optical fibre, the LEDs were hand drilled to provide a 1 mm cavity for the optical fibre to sit. The LEDs are housed inside a brass cone structure to keep the fibre coupling as light tight as possible. TELLIE utilises LEDs with a peak emission wavelength of 505 nm.

The LEDs are powered and controlled by custom driver boards [79]. The design of the driver boards mean that the intensity and pulse frequency of the LEDs are variable parameters which can be chosen at run time. The brass cone housing that contains the LED also contains a PIN diode which can be used to monitor the intensity of the LED. The PIN diode returns a value proportional to the LED intensity. The PIN diodes are calibrated, via potentiometers, such that they are sensitive in the low light intensity regime.

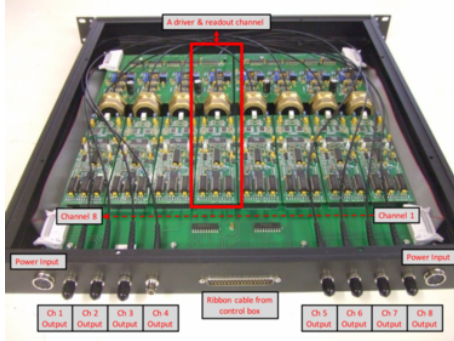


Figure 4.3: A photo of the inside of a box containing the electronics for 8 AMELLIE channels. The driver board, LED housing and PIN board are visible, along with the internal optical fibres.

## 4.5 Optical calibration by light injection

Understanding the optical properties of the scintillator, acrylic and external water are of great importance for accurate reconstruction of events in the SNO+ detector. It is the optical photons that are collected by the PMTs and their transport must be modelled correctly. The accuracy of the position and energy reconstruction can be reduced if the attenuation of photons between their creation vertex and the PMTs is not taken into account. Accurate and reliable measurements and monitoring of the optical properties is therefore critical to all analyses that use data collected by SNO+.

### 4.5.1 SMELLIE

SMELLIE is the scattering module of ELLIE and is designed to provide an accurate measurement of optical scattering in the detector medium. SMELLIE is separate to that of AMELLIE and TELLIE as it does not share any hardware of the latter. The principal difference is that SMELLIE uses laser light as the optical source. Wavelengths between 375 and 700 nm are available for use across 5 different lasers. The lasers are coupled to optical fibres via a fibre switch. SMELLIE has the narrowest beam profile of the three ELLIE systems with a half angle of 3°. There are a total of 15 SMELLIE fibres across 5 different injection sites around the PSUP. There are fibres pointing at angles of 0°, 10° and 20° with respect to the center of the detector at each injection site.

The optical scattering in the detector medium is assumed to be dominated by Rayleigh scattering which has a distinct wavelength and angular dependence. The near monochromatic laser light along with the narrow beam profile allow for a direct in-situ measurement of scattering in the detector medium. The number of PMT hits in the beam spot can be

compared with the number of photons injected into the detector, determined by a monitoring PMT that exists as part of the dry end hardware, to determine the scattering length in the detector medium.

#### 4.5.2 AMELLIE

AMELLIE is the attenuation module of ELLIE. AMELLIE uses eight different injection points at four distinct locations around the detector. The two injection points at each location have a different angle of injection with respect to the centre of the detector:  $0^\circ$  and  $20^\circ$ . The injection angles at each location provide two different optical paths with different path lengths through the scintillator and external water. AMELLIE will monitor the relative change of attenuation in the liquid scintillator over time. As an in-situ source that is quick to run with no cleanliness concerns, AMELLIE is intended to inform the necessity for a dedicated source deployment (e.g laserball).

AMELLIE as a full calibration system can be broadly split into the LEDs (and associated dry end electronics) and the optical fibres. Each AMELLIE channel consists of an LED and optical fibre pair. The system functions by flashing the LED at a given rate, sending photons into the detector. At the same time, the detector DAQ is triggered externally to coincide with the photons entering the detector and the events are saved. A large number of events are recorded using each light injection point to create a complete AMELLIE data set.

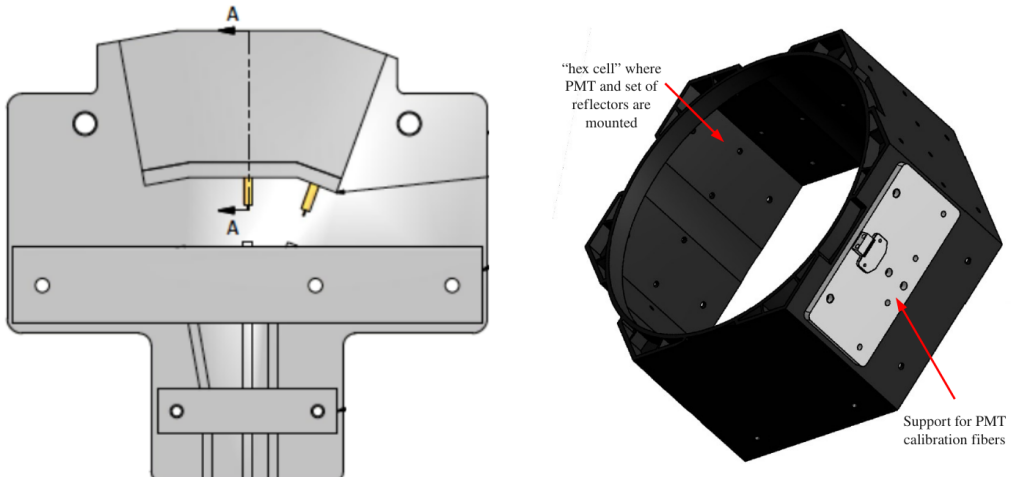
##### 4.5.2.1 Wet end hardware

The fibres that are used by AMELLIE are BFH22-200 multimode step-index fibres produced by Thorlabs<sup>1</sup>. These fibres have a numerical aperture of 0.22 which corresponds to a beam half angle of approximately  $9^\circ$ . The numerical aperture is chosen to minimise the time profiles of the LED/fibre coupled system due to modal dispersion, while still illuminating a sufficient number of PMTs in the beam spot.

The fibres are 45 m in length and run from the ELLIE rack to the PSUP through the external cavity. The fibres are fixed in place by mounting plates, as shown in Figure 4.4. Each of the PMTs are housed in a hexagonal plastic casing (hex cell) which is attached to the PSUP. The mounting plates for the ELLIE fibres are attached to one side of a hex cell. The mounting plates were designed such that there is no shadowing of the PMTs while also providing a clear optical path from the fibre end into the detector.

---

<sup>1</sup>Thorlabs datasheet



- (a) The mounting plates that the optical fibres are fed through. The three positions corresponding to different angles of injection are visible.
- (b) A hex cell that houses a single PMT.

Figure 4.4: Drawings of the AMELLIE fibre mounting plates and the PMT hex cells upon which they are attached. The mounting plates are fixed to one side of a hex cell. The three grooves corresponding to different angles of injection are visible on the mounting plate. Taken from [80]

#### 4.5.2.2 Data collection

Collecting AMELLIE data can be done remotely with minimal downtime to normal physics data taking. The operator configures AMELLIE with the required input settings, notably the intensity of the LED, the pulse frequency and the injection point. In normal circumstances the pulse frequency is chosen to be 1 kHz, to ensure that the DAQ is not overwhelmed whilst avoiding multiple light pulses per event. The intensity of the LED is tuned such that the average number of PMTs registering a hit in an event is a pre-determined value. The operator then runs AMELLIE for a total of 200,000 events in order to obtain adequate statistics. The detector is externally triggered when AMELLIE is running to ensure that the light that is injected is read out by the DAQ. This process is performed for all eight injection points and typically takes around one hour.

AMELLIE is designed to accept external triggers and generate an LED pulse when such a trigger is received. When running in this mode both the signal sent to AMELLIE and the signal sent to the DAQ is provided by the Trigger Utility Board II (TUBii). TUBii latches both signals to the 50 MHz detector clock removing any potential jitter in the trigger time.

## 4.6 Monitoring optical attenuation

The AMELLIE analysis involves the selection of PMT hits in a light injection event from a 2D phase space of time and PMT position. Figures of merit (FOMs) are constructed and then compared across datasets to deduce the general trend of optical attenuation in the liquid scintillator. There are a large amount of parameters and inputs related to the system that must be understood in order to undertake such an analysis and produce meaningful results. The analysis presented in the remainder of this chapter is the most recent contributions to an analysis that is still in development.

Photons that exist in the detector will undergo many different optical processes due to the presence of the three main materials in the SNO+ detector: water, scintillator and acrylic. Photons can undergo scattering, absorption, reemission and reflection as they travel through the detector. These processes can change how events in the detector manifest and need to be accounted for in simulation and reconstruction algorithms.

### 4.6.1 Injection points

#### 4.6.1.1 Direction of fibres

The location of the injection points were recorded at installation time and have been verified in the water phase. It is important to determine the direction in which the fibre ends point. The mounting plates shown in Figure 4.4 have some small uncertainty in their fittings due to the use of rivets that were slightly smaller than the holes that were machined in the hex cells. Therefore the mounting plates have settled into positions that are not completely flush with the hex cells, leading to a small offset in the directions of the fibre ends.

The direction of the fibres is measured using data taken in the water phase. A 2D Gaussian fit is performed to the PMT hit maps using a modified version of an existing fitting routine [81]. Firstly, the occupancy of each PMT is calculated for the run used to fit the direction, where the occupancy of PMT  $i$  is defined as

$$\text{PMT}_{\text{occ}}^i = \frac{\text{PMT}_{\text{hits}}^i}{\sum_{j=0}^{N_{\text{PMTs}}} \text{PMT}_{\text{hits}}^j}, \quad (4.1)$$

where  $\text{PMT}_{\text{hits}}^i$  is the number of hits recorded by PMT  $i$  across the whole run. PMTs with high occupancy ( $> 5\%$ ) are excluded from the fit. Secondly, using the known position of the light injection point and the initial estimate of the direction, all PMTs within a  $20^\circ$  cone from the expected beamspot are weighted by their occupancy and position from the

expected beamspot centre. The weighted position of these PMTs are projected onto a 2D plane at the weighted centre point and a 2D Gaussian fit is performed to extract the beamspot centre. An example of such a fit is shown in Figure 4.5 where the fit procedure is also applied to the reflected beamspot, that is, light that reflects off the AV and is collected by PMTs near the injection point.

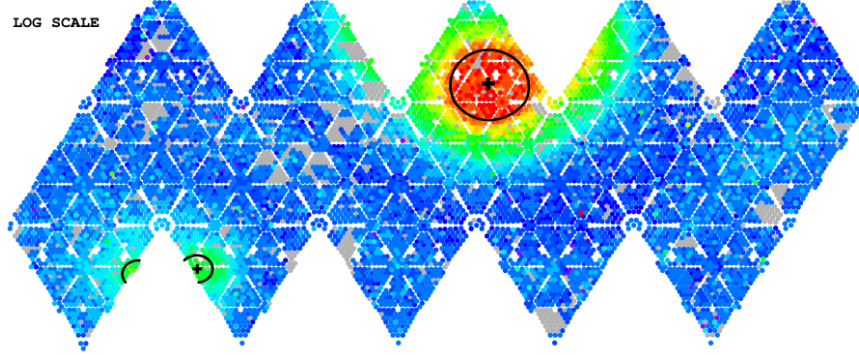


Figure 4.5: A PMT hit map for an AMELLIE run with a fit for the beamspot centre. Both the direct and reflected beamspots are fit (separately), with the fit result marked by heavy plus symbols and the  $1\sigma$  contour lines drawn. Offline PMTs are marked in grey.

Finally, the fit result is compared to that of the recorded direction. An estimate of the beam centre is obtained by calculating a straight line from the recorded fibre position using the recorded direction. The angle between the fitted beamspot centre and the estimated centre is calculated and the results for each fibre are shown in Table 4.2. It is seen that the deviation between the fit result and the expected beamspot is consistent with  $0^\circ$  to within  $1\sigma$  for 5 out of 8 fibres. The maximum deviation away from  $0^\circ$  for any fibre is  $1.44\sigma$ , for fibre FA108. It is noted that this fibre is located at the top of the PSUP and points downwards and is impacted by the neck of the AV. The refracted optical path through the neck is not considered when estimating the beamspot centre leading to an enhanced deviation from the fit result. A similar argument can be made for fibre FA089, as this fibre terminates at the bottom of the PSUP and points almost directly upwards. The fitted results shown have not been used to correct the MC and it is anticipated that they will constitute a systematic uncertainty in the final AMELLIE analysis.

#### 4.6.2 Beam profile tuning

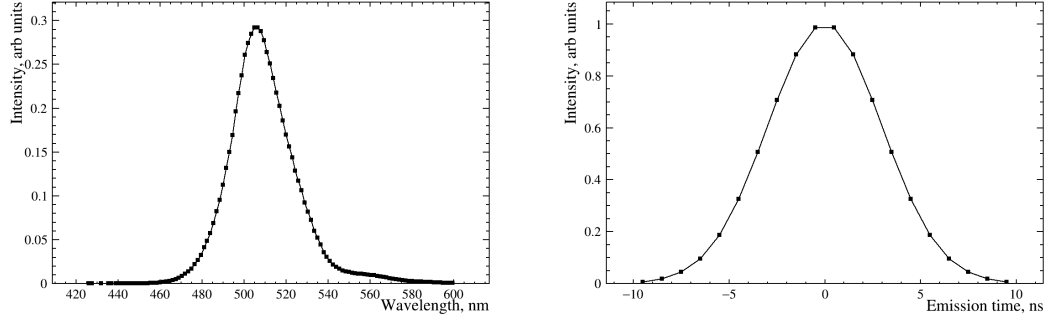
The techniques deployed in the AMELLIE analysis are developed using MC simulated data. It is therefore important that the beam profile of the fibres in simulation matches what is seen in data.

Table 4.2: The deviation between the estimated and fitted beam spot centre for each AMELLIE fibre, fitting to data collected during the water phase. In 5 out of 8 fibres the deviation is consistent with  $0^\circ$  within  $1\sigma$ . All fibres are consistent with  $0^\circ$  within  $1.5\sigma$ .

Fibre (Angle w.r.t centre)	Fit deviation, $^\circ$
FA050 ( $0^\circ$ )	$1.78 \pm 2.74$
FA089 ( $10^\circ$ )	$3.20 \pm 2.74$
FA092 ( $0^\circ$ )	$2.16 \pm 2.74$
FA093 ( $20^\circ$ )	$1.08 \pm 2.70$
FA108 ( $0^\circ$ )	$3.99 \pm 2.77$
FA150 ( $20^\circ$ )	$2.55 \pm 2.77$
FA173 ( $20^\circ$ )	$3.13 \pm 2.70$
FA189 ( $0^\circ$ )	$0.61 \pm 2.73$

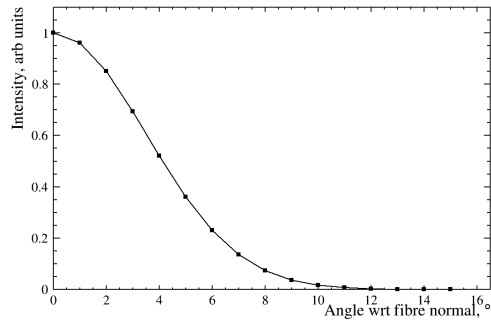
Photons are generated in simulation at the ends of the fibres by sampling three distributions: a wavelength profile, a time profile and an angular profile. The wavelength profiles are modelled as two half Gaussian distributions, using spectral measurements performed on the LEDs in a benchtop setup. The time profile of the LEDs is modelled as a single Gaussian distribution with a width of 3 ns, based on lab measurements. The angular distribution is modelled as a Gaussian distribution with a width  $3.5^\circ$ , based on measurements of the 2D intensity profile of the fibres made in a benchtop setup. Details of the measurements of the distributions are found in [80]. The quartz fibres used in AMELLIE were found to have the same  $\sigma$  in both dimensions of the measurement. The three distributions are shown in Figure 4.6.

A substantial improvement to the angular distribution of the photons can be made by tuning the MC distribution such that the distribution of hit PMTs better match the data. Firstly, a selection was made to isolate prompt PMT hits, that is PMT hits caused by photons that were not affected by optical processes such as scattering. The selection was implemented by requiring valid PMT hits to be in a 45 ns window that is centered around the prompt timing peak. Secondly, the PMT hits were weighted corresponding to their angular distance from the expected beamspot centre, as per the recorded position and direction. This is included to reduce the impact of random noise PMT hits while also



(a) The wavelength distribution for the 503 nm LED used in AMELLIE. The  $\sigma_{\text{left}}$  is 10.02 nm and the  $\sigma_{\text{right}}$  is 12.65 nm.

(b) The time distribution. The  $\sigma$  is 3 ns.



(c) The angular distribution. The  $\sigma$  is  $3.5^\circ$ .

Figure 4.6: The distributions that are sampled when generating photons in the AMELLIE simulation.

placing more importance on PMTs located within the beamspot.

The weighted PMT hit distributions are fit with half-Gaussian functions. The ratio of the fitted  $\sigma$  of the half-Gaussian fits to data and simulation is calculated and the MC distribution is scaled by this ratio, as shown in Figure 4.7. This ratio is shown for all eight AMELLIE fibres in Figure 4.8, with the associated error bars multiplied by a factor of 10 for illustrative purposes. The average ratio across all fibres is  $1.64 \pm 0.25$  and the  $\sigma$  of the MC angular distribution is scaled by this factor. It is noted that the ratios of fibres FA050 and FA150 are approximately two standard deviations away from the mean ratio. These fibres are located close to the middle of the detector (in the vertical axis) and are affected by belly plates which may not be correctly modelled in simulation, leading to anomalous results here.

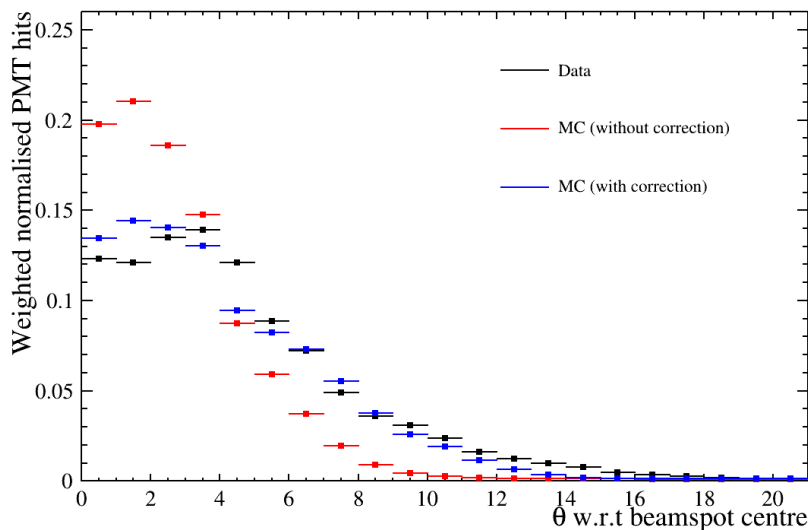


Figure 4.7: The PMT hits for all events in AMELLIE (simulated) data. The PMTs are weighted by their distance from the beamspot centre.

### 4.6.3 Optical attenuation

#### 4.6.3.1 Optical paths in SNO+

When AMELLIE is operating photons are injected into the detector from a point on the PSUP. A majority of the photons will travel through the external water, acrylic and scintillator unimpeded. However, photons may experience optical effects while propagating or at material boundaries. Photons may undergo Rayleigh scattering in the external water and the liquid scintillator. Additionally, photons may also be absorbed by the scintillator and have a wavelength dependent probability of being re-emitted. The absorption and scattering lengths in the scintillator cocktail, as modelled in simulation, are shown in Figure 4.9. The absorption length of the individual components that make up the liquid scintillator cocktail are shown separately. As described in Chapter 3 LAB is the liquid scintillator and PPO is used to increase the light yield when energy is deposited in the scintillator. bis-MSB is a wavelength shifter that is designed to produce photons with a wavelength that more closely matches the maximal quantum efficiency of the SNO+ PMTs. The final component not yet mentioned, TeDiol, is a compound that is formed when telluric acid is heated with 1,2-butanediol. This compound is soluble in LAB and represents the final component of the SNO+ tellurium loaded liquid scintillator cocktail. This is described in more detail in [82].

Photons may undergo reflection or transmission at the water/acrylic, acrylic/scintillator

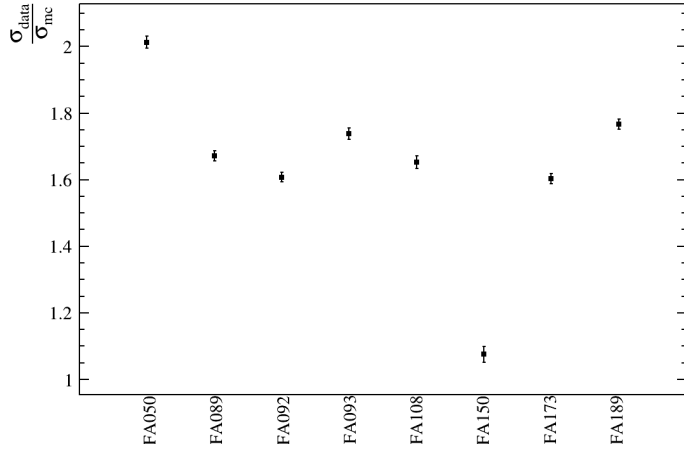
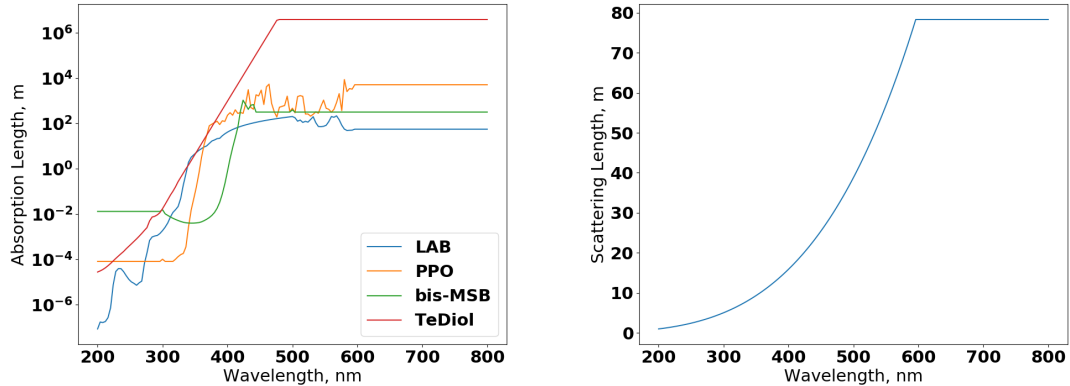


Figure 4.8: The ratio of the fitted  $\sigma$  of half-Gaussian fits for data and MC simulation. The error bars are multiplied by a factor of 10 for visual purposes.

and water/PMT glass interfaces. The majority of AV reflections occur at the acrylic/water boundaries due to the closely matching refractive indices of acrylic and scintillator. Finally, photons that enter the PMT bucket may not fall on the photocathode and may instead reflect off the glass and return to the external water.



(a) The absorption length of the components of the scintillator cocktail.  
(b) The scattering length of the scintillator cocktail.

Figure 4.9: The absorption and scattering lengths of the liquid scintillator cocktail. The main components that contribute to the absorption are modelled separately, while the cocktail is treated with a single wavelength dependent scattering length.

#### 4.6.3.2 Identification of optical paths

The optical processes described in Section 4.6.3.1 are easily identified in simulated data by looking at the MC truth information for the photons. When looking at real calibration data this is impossible. It is therefore of great importance to identify photons that undergo the various optical effects by using real observables. The location of PMTs, relative to the fibre, and the time at which they are hit are used to identify photons undergoing these optical processes. This takes advantage of the fact that those photons will travel longer path lengths in the detector.

Figure 4.10 shows a phase space of residual hit time and PMT position for all events in a typical AMELLIE run. The position of a given PMT is displayed as the angle between the injection point and the PMT as seen from the centre of the detector. In this representation the injection point is at  $\cos(\alpha) = 1$  and the direct beamspot is centered around  $\cos(\alpha) = -1$ . The residual hit time,  $t_{\text{res}}$ , is as defined in Equation 3.1.

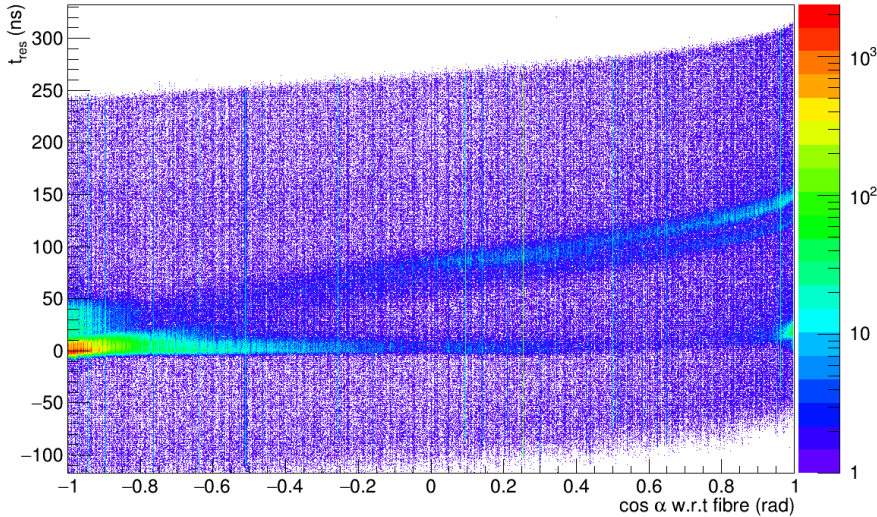


Figure 4.10: The residual hit time and PMT position phase space for a typical AMELLIE run in the water phase. The residual hit time is the PMT hit time that has been corrected for the photon time of flight and injection time.  $\alpha$  is the angle between a PMT and the injection point as seen from the detector centre.

Regions of interest are identified in Figure 4.10 to emphasize the power in this particular phase space. The region at  $\cos(\alpha) \approx -1$  and  $t_{\text{res}} \approx 0$  is the direct beamspot. The width of the distribution in time is due to the timing profile of the photon injection along with the PMT pulse timing profile. The region at  $\cos(\alpha) \approx 1$  and  $t_{\text{res}} \approx 0$  is the reflected beamspot.

The two bands that span across the entire PMT position space that increase in  $t_{\text{res}}$  with increasing  $\cos(\alpha)$  are due to the reflections from the PSUP/PMTs and the far side of the AV. The triangular region in the middle of the plot (in terms of both  $t_{\text{res}}$  and  $\cos(\alpha)$ ) are photons that have undergone either optical scattering or absorption and subsequent re-emission. Figure 4.11 verifies the regions discussed by displaying the MC truth information for simulated AMELLIE data. By visualising the path taken by simulated optical photons in the  $t_{\text{res}}$  and  $\cos(\alpha)$  phase space the relationship between regions of the phase space and optical paths is justified.

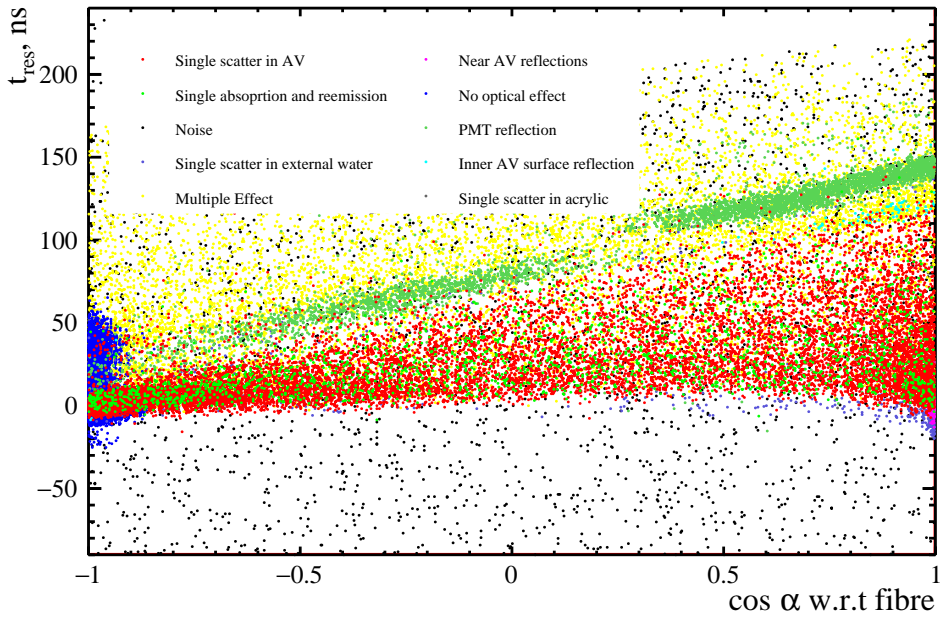


Figure 4.11: The residual hit time and PMT position phase space for simulated AMELLIE MC events, separated by optical path. The wavelength simulated is 403 nm to highlight the absorption. The MC truth information is used to identify photons that underwent different optical effects and their position in the phase space is uncovered.

#### 4.6.3.3 Tracking optical changes

The regions identified in Section 4.6.3.2 are used to construct FOMs to monitor the optical attenuation over time. When considering the amount of attenuation in the liquid scintillator it is reasonable to expect that more or less light will be present in the direct beamspot when the attenuated length is increased or reduced respectively.

The FOMs make use of the number of hits in the direct beamspot, the reflected beamspot and the triangular region. The direct and reflected beamspot regions are cre-

ated using simple box cuts. The triangular region is found by an algorithm that optimises the signal to background ratio, where the signal is attenuated light.

While many combinations of the regions (along with the full phase space) can be used, the two that give the best performance are

$$\text{FOM}_1 = \frac{\text{hits in reflected region}}{\text{hits in direct region}}, \quad (4.2)$$

$$\text{FOM}_2 = \frac{\text{hits in triangular region}}{\text{hits in direct region}}. \quad (4.3)$$

Figure 4.12 shows the percentage change from the nominal for these FOMs as a function of changing scattering length or absorption length, simulating a 375 nm LED to generate the photons. This study was performed for various wavelength LEDs but a 375 nm LED is chosen in order to probe the wavelength region most sensitive to optical attenuation whereby use of an LED is feasible. In both cases the FOM is more sensitive to a change in the scattering length. This increased sensitivity can be explained by considering that the nominal absorption length at this wavelength is 8.6 mm, while the scattering length is 12.4 m. The path length across the AV is comparable to the scattering length while it is many times larger than the absorption length. Therefore the relative change in the absorption length has less impact than that of the scattering length.

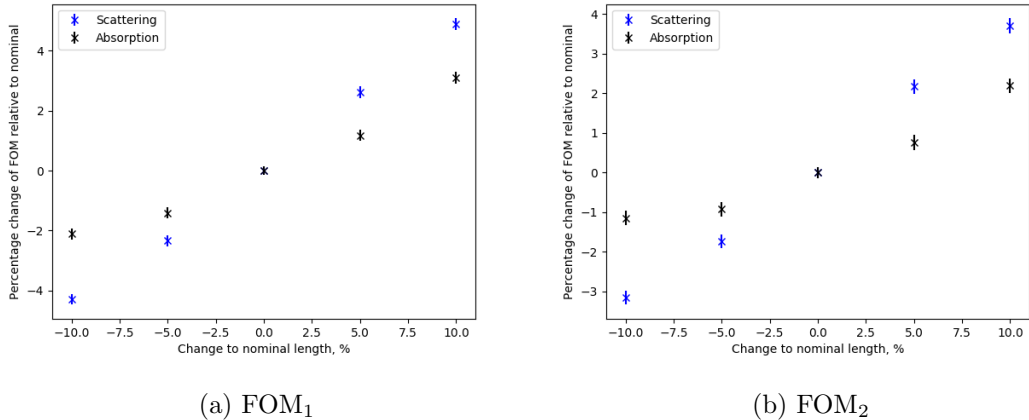


Figure 4.12: The FOMs used to measure the change in optical properties. The error bars are statistical only and are multiplied by a factor of 100 for display purposes.

It is shown that for a 10% change in the scattering length of the scintillator, the FOMs changes by approximately 4%. For the same change in the absorption length the FOMs change by approximately 2%. The error bars displayed are statistical uncertainties only and are multiplied by a factor of 100 for illustration purposes. The results quoted are very

preliminary and are intended to demonstrate that such an analysis is feasible. The regions will undergo further optimisations to improve the results.

#### 4.6.4 Further improvements

The analysis presented here is very preliminary and there are aspects that will be refined to determine the sensitivity of AMELLIE. A large omission thus far are systematic uncertainties arising from both the region selection and detector effects. The regions are defined in terms of time and position and uncertainties can be assigned to these quantities. The uncertainties in  $\cos(\alpha)$  is qualitatively estimated to be small as the PMT positions and fibre positions are well known. When calculating  $t_{\text{res}}$  the same injection time for the photons is used. As discussed in Section 4.6.2 the emission time profile of the LEDs is a Gaussian distribution with a  $\sigma$  of 3 ns and as such hits may fall into different time bins. The impact of this will need to be assessed and incorporated into the analysis.

The optimisation of the triangular region uses MC truth information and if the simulation does not accurately match the data then the region selected may not be optimised for data. This can lead to reduced sensitivity due to hits leaking into the defined region or by the absence of signal in the region. The direct and reflected beamspot regions are currently loosely defined and it is possible that tighter cuts here could improve the sensitivity as the regions become more susceptible to hits falling inside or outside them.

### 4.7 Conclusion

Calibration of the detector is vital to have confidence in any physics analysis that is undertaken. Notably it is important to have systems and analyses in place to effectively monitor the change in attenuation length in the liquid scintillator as this is a main input for the detector optical model. Steps have been undertaken to move towards such an approach using AMELLIE. The positions and the directions of the installed AMELLIE fibres have been verified and the MC simulation has been significantly improved. This has enabled a proof of concept study to be completed with MC simulated data that supports the view that AMELLIE can be used to monitor the optical attenuation over time.

## Chapter 5

# Reactor antineutrinos at SNO+

### 5.1 Introduction

SNO+ is a multipurpose physics experiment and the detection of reactor antineutrinos is the primary physics goal in the pure scintillator phase. SNO+ is in a position to contribute to understanding the current tension between the measurements of  $\Delta m_{21}^2$  by KamLAND (reactor antineutrinos) [36] and SNO/Super-Kamiokande (solar neutrinos) [39]. KamLAND reports  $\Delta m_{21}^2 = 7.53^{+0.19}_{-0.18} \times 10^{-5}$  eV<sup>2</sup> while the SNO/Super-Kamiokande joint fit is  $\Delta m_{21}^2 = 4.84^{+1.26}_{-0.60} \times 10^{-5}$  eV<sup>2</sup>, a disagreement on the order of  $2.15\sigma$ .

SNO+ is able to perform independent measurements of  $\Delta m_{21}^2$  using both reactor antineutrinos and solar neutrinos, along with a joint measurement combining the two analyses. These results will shed light on the incompatible measurements from solar and reactor experiments. The sheer size of the detector coupled with relatively nearby nuclear reactor cores allow such a measurement to be made using reactor antineutrinos. The measurement of both  $\Delta m_{21}^2$  and  $\theta_{12}$  is possible with the antineutrino analysis, further allowing SNO+ to contribute to the global determination of neutrino oscillation parameters.

Antineutrinos are identified by selecting two events that are close to each other in both space and time. This corresponds to a prompt positron annihilation and delayed neutron capture, produced in an IBD interaction, as will be described in more detail in Section 5.4. The shape of the prompt event energy spectrum is defined by the values of the oscillation parameters. Therefore, the measurement of  $\Delta m_{21}^2$  and  $\theta_{12}$  is obtained by performing a maximum likelihood fit to the prompt energy spectrum of reactor antineutrino events. The contributions of given reactor cores to the total antineutrino flux are floating parameters in the fit and must be understood and constrained. The details of the oscillation parameter fit is discussed in more detail in Chapter 7.

The coincident nature of antineutrino events leads to excellent background rejection in this analysis. However, antineutrinos are not the only interactions that manifest as two coincident events in the detector.  $^{13}\text{C}(\alpha, n)^{16}\text{O}$  and geoneutrino interactions mimic the antineutrino signal and must be accounted for when fitting the prompt energy spectrum. These will be discussed in more detail in Section 5.3.

## 5.2 Sources of reactor antineutrinos

Reactor antineutrinos are produced in the cores of nuclear reactors. Reactors are driven by nuclear fission reactions where large unstable nuclei (such as  $^{238}\text{U}$ ) split into two smaller daughter nuclei after bombardment with neutrons. This process produces more neutrons which induce more fission interactions in nuclei. The daughter nuclei undergo  $\beta$  decays that produce electrons and electron antineutrinos. The antineutrinos then travel through the Earth to the SNO+ detector and interact in the liquid scintillator. The antineutrinos are produced isotropically from the reactor cores and as such antineutrinos from any reactor core in the world can be detected at SNO+.

The number of antineutrinos arriving at SNO+ from any given nuclear reactor core is determined by the thermal power of the core,  $P_{\text{Th}}$ , and the distance from the detector,  $R$ , as

$$N_{\bar{\nu}_e} \propto \frac{P_{\text{Th}}}{R^2}. \quad (5.1)$$

Therefore, the reactor cores that are closest to the detector make the biggest contribution to the expected antineutrino flux. Canada has four nuclear power plants, three of which are in Ontario and thus close to SNO+. The closest reactor complex to SNO+ is the Bruce Nuclear Generating Station, the largest reactor complex in North America [83]. Bruce is located approximately 240 km away from SNO+ and has a total of 8 operational reactor cores, each with an approximate power output of 2800 MW<sub>Th</sub>. Approximately 40% of the antineutrino flux at SNO+ originates from Bruce.

Pickering Nuclear Generating Station is a reactor complex located approximately 340 km away from SNO+. There are 6 active reactor cores that each produce approximately 1750 MW<sub>Th</sub> of power. The Darlington Nuclear Generating Station is located approximately 350 km away from SNO+. Darlington has 4 operational reactor cores, each with an approximate power output of 2775 MW<sub>Th</sub>. These two reactor complexes together contribute approximately 20% of the antineutrino flux at SNO+. The final reactor complex, not located in Ontario, is Point Lepreau Nuclear Generating Station. This complex is

located approximately 1150 km from SNO+ and has a single reactor core producing 2180 MW<sub>Th</sub>.

The nuclear reactors used throughout Canada are CANDU pressurised heavy water reactors (PHWR) [83]. While most of the design aspects of the nuclear reactors are inconsequential for performing physics analyses with antineutrinos, the fuel used in a reactor core is critical information when predicting the antineutrino flux. The fissile materials that produce antineutrinos are two isotopes of uranium:  $^{238}\text{U}$  and  $^{235}\text{U}$ , and two isotopes of plutonium:  $^{241}\text{Pu}$  and  $^{239}\text{Pu}$ . The energy spectrum of antineutrinos produced by each of these four isotopes is unique and therefore knowledge of the relevant fractions of each isotope in the fuel is required. This will be discussed in more detail in Chapter 6.

Almost all of the remaining antineutrino flux is produced at the reactors that are located in the USA. There are 31 nuclear reactor complexes that are located within 1000 km of SNO+ (excluding Bruce, Pickering and Darlington) and another 27 complexes located further than 1000 km from SNO+ on the North American continent. The reactors constructed in the USA are one of two types: pressurised water reactors (PWR) or boiling water reactors (BWR). As with the CANDU reactors, the design of the reactors is largely irrelevant but the fractions of the fissile isotopes in the fuels used is important information.

When considering the global landscape of nuclear power there are over 190 active nuclear reactor complexes around the world [83]. Each one of the reactor cores at these complexes will contribute to the overall antineutrino flux at SNO+. As per Equation 5.1, the large distances involved with those reactors not in North America mean that their contribution to the flux is small. All of reactors outside of North America sum for a contribution of approximately 2% to the antineutrino flux at SNO+. Furthermore, dependence of  $\Delta m_{21}^2$  on the electron antineutrino survival probability is lost for these reactors, as per Equation 2.37, due to the large oscillation baseline.

### 5.3 Backgrounds

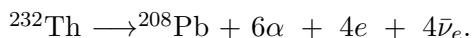
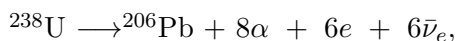
Reactor antineutrinos manifest in the detector as two coincident events (separated by up to 0.8 ms) which allows for excellent background rejection. There are two significant types of interactions that also appear as two coincident events: geoneutrino interactions and  $^{13}\text{C}(\alpha, n)^{16}\text{O}$  interactions. These interactions must be predicted and accounted for when performing the oscillation analysis.

There is also a third background to consider: the accidental coincidence background.

These are two completely unrelated events that occur close to each other in space and time with a delayed event energy near to that of a neutron capture. Such event pairs survive all analysis cuts and look like a signal or background interaction. The rate of accidental coincidence events was calculated to be negligible when compared to the geoneutrino and  $^{13}\text{C}(\alpha, n)^{16}\text{O}$  background and are not considered further in this analysis [84].

### 5.3.1 Geoneutrinos

Geoneutrinos are the collective name for electron antineutrinos that are produced in the mantle and crust of the Earth. These antineutrinos are the product of  $\beta$  decays in the uranium and thorium decay chains. The Earth's crust and mantle contain trace amounts of  $^{238}\text{U}$  and  $^{232}\text{Th}$  [85]. These isotopes are unstable and undergo a series of  $\alpha$  and  $\beta$  decays to stable isotopes of lead, collectively summarised as



The antineutrinos produced as a result of these decay chains can be seen in the detector with the same coincidence signal as reactor antineutrinos, as their energies are on the MeV scale. Another source of geoneutrinos is the  $\beta$  decay of  $^{40}\text{K}$ , however, the energy of these antineutrinos are below the IBD threshold energy and therefore they cannot interact in the SNO+ detector.

The study of geoneutrinos is of great interest for the geological modelling of the Earth's radiogenic heat flux [86]. The decay chains of uranium and thorium are thought to produce approximately 80% of the radiogenic heat from the Earth's interior [85]. The detection of geoneutrinos at SNO+ would be the first of its kind in North America. The detection would help constrain and improve geological models by providing more insight into the relative amounts of uranium and thorium present in the Earth's mantle and crust. This will also provide more information for radiogenic heat models.

Geoneutrinos are considered a background in the reactor antineutrino analysis as they provide no information about  $\Delta m_{21}^2$  or  $\theta_{12}$ . The antineutrinos can originate from any location within the Earth's mantle or crust and therefore the baseline used to calculate the survival probability is unknown. This leads to the use of the average survival probability (Equation 2.37) for geoneutrino oscillation. The dependance of  $\Delta m_{21}^2$  is lost and the impact of  $\theta_{12}$  is on the order of 3%, well below the statistical uncertainties expected in the early stages of such an analysis.

### 5.3.2 $^{13}\text{C}(\alpha, n)^{16}\text{O}$

The  $^{13}\text{C}(\alpha, n)^{16}\text{O}$  interaction is the largest background in the antineutrino oscillation analysis. The interaction occurs when an  $\alpha$  particle interacts with a  $^{13}\text{C}$  nucleus to emit a neutron, as



This signal mimics the reactor antineutrino signal by virtue of a prompt event and a delayed neutron capture event in coincidence. Therefore it is almost impossible to distinguish these events from reactor antineutrino events with a coincident event tag. The first demonstration of the differentiation of  $^{13}\text{C}(\alpha, n)^{16}\text{O}$  events from reactor antineutrino events is reported in Chapter 8.

A single molecule of the liquid scintillator used in SNO+ is a phenyl ring and two methyl groups attached to a carbon chain. The length of the carbon chain is variable and therefore each molecule contains between 15 and 20 carbon atoms [57]. Natural carbon exists as 98.9%  $^{12}\text{C}$  and 1.1%  $^{13}\text{C}$ . The  $^{13}\text{C}$  atoms that participate in the  $^{13}\text{C}(\alpha, n)^{16}\text{O}$  interactions are a fundamental component of the scintillator and their number cannot be reduced.

The  $\alpha$  particle that initiates the  $^{13}\text{C}(\alpha, n)^{16}\text{O}$  interaction is not a fundamental component of the scintillator and arises as a product of the decay of radioactive contaminants in the detector. The decay chain of interest here is the uranium decay chain, prompted by the existence of  $^{222}\text{Rn}$  in the detector. Radon is a component of the air in SNOLAB and small amounts of radon were introduced into the detector during the scintillator filling process.

Figure 5.1 outlines the uranium decay chain. When starting with  $^{222}\text{Rn}$  there are four  $\alpha$  decays before reaching the stable isotope of  $^{206}\text{Pb}$ . The  $\alpha$ s from these four decays can initiate the  $^{13}\text{C}(\alpha, n)^{16}\text{O}$  interaction. Three of these four decays can be mitigated and thus any subsequent  $^{13}\text{C}(\alpha, n)^{16}\text{O}$  interaction can be disregarded. The first  $\alpha$  comes from the decay of  $^{222}\text{Rn}$  itself. The half life of this decay is approximately 3.8 days [88] and therefore the number of  $\alpha$ s from  $^{222}\text{Rn}$  can be reduced by simply letting a significant fraction decay away. For this to be effective it is chosen to not use data collected for approximately two weeks after the introduction of radon for analysis. The second  $\alpha$  is produced by the decay of  $^{218}\text{Po}$  that immediately follows the  $^{222}\text{Rn}$  decay. This decay has a half life of approximately 3 minutes [89] and therefore the same strategy can be deployed to reduce the number of  $\alpha$  particles in the detector. The third decay occurs when  $^{214}\text{Po}$  decays with a half life of approximately 164  $\mu\text{s}$  [89]. The short half life allows for such

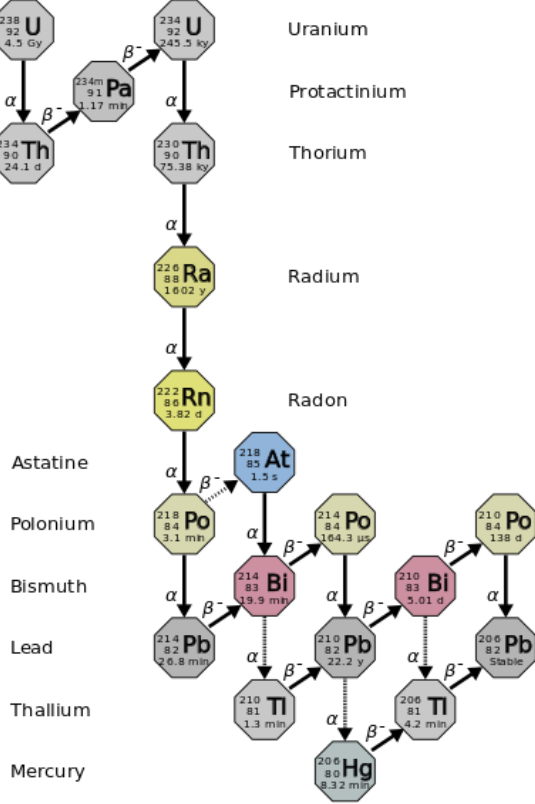


Figure 5.1: The decay chain of uranium. The  $\alpha$  particles that initiate  $^{13}\text{C}(\alpha, n)^{16}\text{O}$  interactions are the product of  $^{210}\text{Po}$  decays that come from small amounts of  $^{222}\text{Rn}$  in the detector. Taken from [87].

decays to be identified by looking for an event that is coincident in space and time with the previous decay of  $^{214}\text{Bi}$ . Any  $^{13}\text{C}(\alpha, n)^{16}\text{O}$  interactions that follow these coincident BiPo events can be disregarded.

The final  $\alpha$  decay in the uranium chain is that of  $^{210}\text{Po}$ . This decay has a half life of approximately 138 days [89] with the product being the stable  $^{206}\text{Pb}$  and as such it cannot be identified by coincidence with another decay. With its relatively long half life it is also unfeasible to wait for a significant fraction of the  $^{210}\text{Po}$  to decay away. Therefore the  $\alpha$ s produced by the decay of  $^{210}\text{Po}$  are the primary source of  $\alpha$ s that drive the  $^{13}\text{C}(\alpha, n)^{16}\text{O}$  interactions. The rate of  $^{13}\text{C}(\alpha, n)^{16}\text{O}$  interactions is directly related to the rate of  $^{210}\text{Po}$  decays in the detector, discussed in more detail in Chapter 6.

The  $^{13}\text{C}(\alpha, n)^{16}\text{O}$  interaction is only one of multiple possible  $(\alpha, n)$  interactions. An  $\alpha$  particle may interact with an  $^{18}\text{O}$  or  $^{17}\text{O}$  nucleus to produce a neutron and a  $^{21}\text{Ne}$  or  $^{20}\text{Ne}$  respectively. While there is oxygen in the liquid scintillator cocktail, one molecule of PPO has one oxygen atom, the number of oxygen atoms is several orders of magnitude

lower than that of  $^{13}\text{C}$ . The natural abundance of  $^{18}\text{O}$  and  $^{17}\text{O}$  combined is 0.24% [90]. Furthermore, the cross section for  $(\alpha, n)$  interactions where oxygen is the  $\alpha$  target is comparable to that of carbon  $(\alpha, n)$  interactions. Collectively these three facts mean that the  $(\alpha, n)$  interactions involving oxygen are negligible.

## 5.4 Detection

Reactor antineutrinos and geoneutrinos manifest in SNO+ via IBD interactions, introduced in Chapter 2. IBD interactions produce two separate events in the detector that are coincident in space and time, as depicted in Figure 5.2. The prompt event exists due to the deposition of energy by the positron followed by electron-positron annihilation. The annihilation  $\gamma$ s deposit their energy in the liquid scintillator and scintillation photons are incident on the PMTs. Some time later, the neutron that was produced in the IBD interaction undergoes a capture on a free proton. This results in the emission of a 2.2 MeV  $\gamma$  that provides the visible energy for the delayed event.

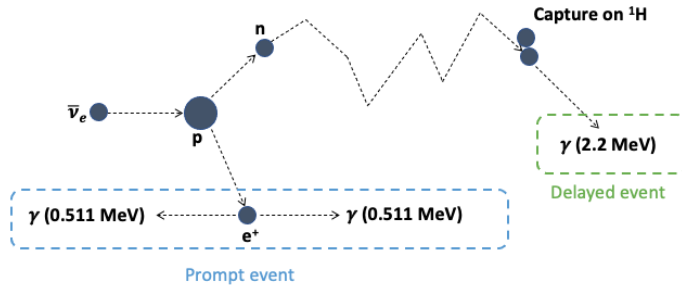


Figure 5.2: A cartoon of an IBD interaction. The prompt event comes from the energy deposition and annihilation of the positron while the delayed event is a neutron capture on a free proton.

The energy released in the delayed neutron capture is determined by the mass difference between the final  $^2\text{H}$  nucleus and initial proton and neutron mass. Therefore all neutron captures on free protons will emit a 2.2 MeV  $\gamma$ . This gives a narrow energy window in which to search for a potential delayed event. Once a candidate delayed event has been identified the proceeding events in some time window can be checked. The reconstructed position of any events identified within this time window with sufficient energy to be that of a positron from an IBD interaction are compared with that of the delayed event. An IBD candidate pair is identified if any of the potential prompt events are located within a given distance of the delayed event.

$^{13}\text{C}(\alpha, n)^{16}\text{O}$  interactions are detected in the exact same way as IBD interactions due to their identical coincident event nature. While the events look the same in the SNO+ detector, only the delayed neutron capture events are identical. The mechanism for the prompt event is different to that of IBD interactions, as shown in Figure 5.3. There are three possible scenarios that can generate the photons in the prompt event. Process 1 is the mechanism by which the majority of prompt  $^{13}\text{C}(\alpha, n)^{16}\text{O}$  events occur. The neutron has a mean capture time on free protons of  $216\ \mu\text{s}$  [91] in liquid scintillator and therefore it travels some distance before undergoing a capture. While travelling the neutron can scatter off protons in the scintillator and lose some of its energy. These protons will recoil and emit photons which are incident on the PMTs and constitutes the prompt event. It will be seen in later chapters that the neutron can scatter multiple protons on a timescale of the order of 10 ns.

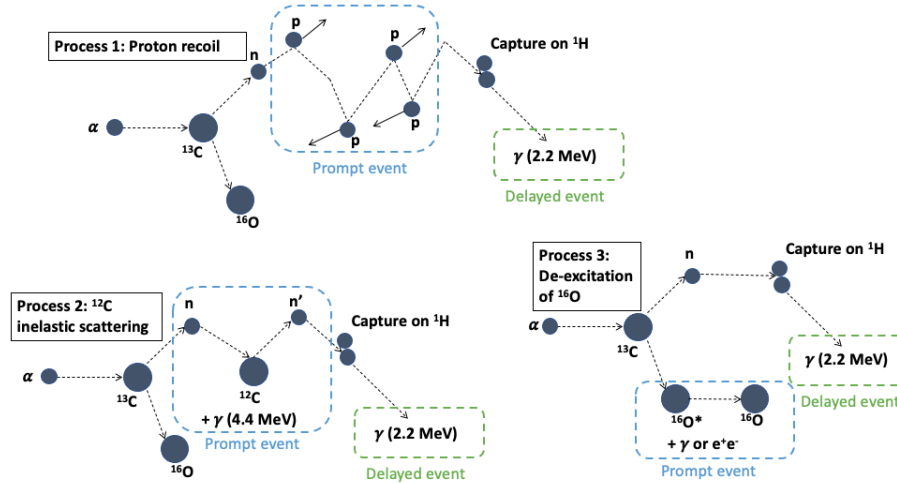


Figure 5.3: A cartoon describing the three possible processes for an  $^{13}\text{C}(\alpha, n)^{16}\text{O}$  interaction. The prompt event can either originate from recoiling protons that are scattered by the neutron as it moves through the scintillator (process 1), or from  $\gamma$  emission due to inelastic scattering on  $^{12}\text{C}$  (process 2) or by de-excitation of  $^{16}\text{O}$  (process 3). The delayed event in all processes is a neutron capture on a free proton.

Protons are not the only obstacles that the neutron may encounter in the scintillator. It is possible that the neutron may scatter inelastically off a  $^{12}\text{C}$  nucleus, described by process 2 in Figure 5.3. Such a scattering interaction excites the  $^{12}\text{C}$  and results in the emission of a 4.4 MeV  $\gamma$  as it de-excites. This  $\gamma$  deposits its energy in the scintillator and the prompt event is formed. The prompt event in process 3 also involves the deposition of energy in the scintillator via a  $\gamma$ . In some cases the  $^{16}\text{O}$  is in an excited state and subsequently de-excites via the emission of a 6.1 MeV  $\gamma$ . Depending on the exact excited

state of the  $^{16}\text{O}$  it may also de-excite by the emission of an electron-positron pair, via pair production. These particles annihilate and the resulting annihilation  $\gamma$ s are seen in the prompt event.

## Chapter 6

# Prediction and selection of reactor IBD and $^{13}\text{C}(\alpha, n)^{16}\text{O}$ events

### 6.1 Introduction

The reactor antineutrino analysis involves the prediction and selection of IBD events induced by antineutrinos originating from nuclear reactors. The prompt energy distribution of such events are fit to extract the oscillation parameters  $\Delta m_{21}^2$  and  $\theta_{12}$ . It is therefore important to correctly simulate antineutrino events so that accurate predictions can be made of what is expected to be observed. More precise predictions can also help constrain floating parameters in the oscillation fitting routine, improving the sensitivity to the parameters of interest.

This chapter describes the methods to model and predict the number of reactor IBD events at SNO+. The techniques to simulate and predict the contributions of the main backgrounds in the analysis are considered. This chapter also describes the selection criteria for finding candidate events in data.

### 6.2 Prediction and simulation

The basis of the reactor antineutrino analysis is the comparison between what is expected and what is observed. The expectation is determined by prediction and MC simulation, while the observation comes from the data collected by SNO+. Therefore the number of both signal and background events seen at SNO+ must be predicted with their uncertainties accounted for.

### 6.2.1 Reactor antineutrinos

The antineutrinos that are released from the  $\beta$  decay of daughter products from nuclear fission reactions within nuclear reactor cores contribute to the signal in this analysis. As described in Chapters 2 and 5 the antineutrinos are detected via the IBD interaction and thus the antineutrinos themselves are not directly observed. The number of expected IBD events is estimated by firstly considering the reactor antineutrino flux at SNO+, secondly considering the effects of oscillation, thirdly the IBD cross section and finally the detection efficiency in SNO+.

#### 6.2.1.1 Reactor antineutrino flux

The first step in predicting the antineutrino flux is to consider the reactor cores in which the antineutrinos are produced. Antineutrinos are the product of decaying daughter isotopes in nuclear fission interactions within a nuclear reactor core. Commercial nuclear reactors use fuels that are typically composed of  $^{235}\text{U}$ ,  $^{238}\text{U}$ ,  $^{239}\text{Pu}$  and  $^{241}\text{Pu}$ . The antineutrino emission spectrum from the neutron induced fission of these four isotopes is the first input into the flux prediction. In RAT the antineutrino spectra of the four isotopes are modelled as 5th order polynomials, as shown in Figure 6.1. The spectra of  $^{235}\text{U}$ ,  $^{239}\text{Pu}$  and  $^{241}\text{Pu}$  are those of the Huber model [92], while the  $^{238}\text{U}$  spectrum is that of the Mueller model [93]. Any other sources of antineutrinos within nuclear reactor cores are not considered.

There are many different designs of nuclear reactors, each with their own fuel compositions. Three different designs of reactors are considered: pressurised heavy water reactors (PHWR), pressurised water reactors (PWR) and boiling water reactors (BWR). Any reactor that has a design that is not one of these three is modelled as a PWR. All three of the designs considered use fuels that are composed of  $^{235}\text{U}$ ,  $^{238}\text{U}$ ,  $^{239}\text{Pu}$  and  $^{241}\text{Pu}$ , with a varying fractional contribution of each isotope. Table 6.1 shows the relative amount of each isotope in the reactor fuel. The fractions for the PWR and BWR are given by measurements performed at KamLAND [5] while the fractions for the PHWR were given by private communication from Atomic Energy of Canada (AECL) in 2013.

Nuclear reactor cores are often characterised by their thermal power output. The energy released per fission is known in literature [94] and this can be combined with the number of neutrinos per fission, as shown in Figure 6.1, to estimate the number of neutrinos per second from a reactor core. The number of antineutrinos per unit time per

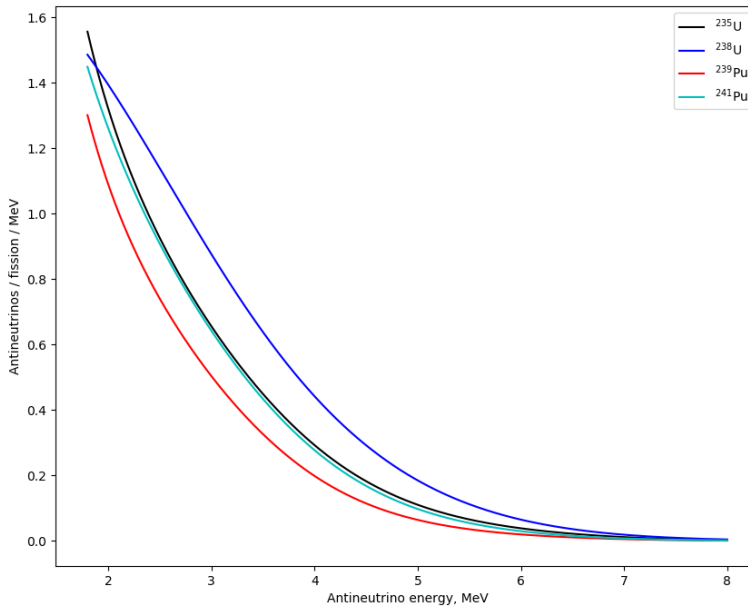


Figure 6.1: The antineutrino spectra as modelled in RAT for  $^{235}\text{U}$ ,  $^{238}\text{U}$ ,  $^{239}\text{Pu}$  and  $^{241}\text{Pu}$ . The spectra of all four isotopes are modelled as 5th order polynomials as described in [92] and [93].

unit energy is given by

$$N_{\bar{\nu}_e}(E, t) = P_{\text{th}} \sum_{i=0}^{N_{\text{isotopes}}} \frac{f_i n_i}{\epsilon_i}, \quad (6.1)$$

where  $P_{\text{th}}$  is the thermal power of the reactor core,  $f_i$  is the fractional contribution in the fuel of isotope  $i$ ,  $\epsilon_i$  is the energy released per fission and  $n_i$  is the number of antineutrinos emitted per fission per unit energy.

Equation 6.1 shows that the number of antineutrinos produced at a given nuclear reac-

Table 6.1: The relative contribution from each isotope in the fuel of the three modelled reactor designs. Data provided by [5] and AECL.

Design	$^{235}\text{U}$	$^{238}\text{U}$	$^{239}\text{Pu}$	$^{241}\text{Pu}$
PHWR	0.52	0.05	0.42	0.01
PWR	0.568	0.078	0.297	0.057
BWR	0.568	0.078	0.297	0.057

tor core is dependent on the thermal power of the core. The design specification, including the maximum thermal power, of nuclear reactor cores is publicly available information [83]. In an idealised world nuclear reactors would operate at their designed power output at all times. However, this is not the case due to refueling campaigns and maintenance. Reactors also have an intended operating lifetime and are permanently shutdown when such time has elapsed. Additionally, reactor fuel components degrade and become weaker over time, reducing the thermal power [95]. It is therefore important to introduce time dependence when considering the thermal power of reactor cores.

The International Atomic Energy Agency (IAEA) publishes an annual report detailing the operational performance of every nuclear reactor in the world [96]. A statistic included in this report is the load factor (LF), a measure of the fuel loading in a given reactor and thus a measure of the relative thermal power. A LF of 100% indicates that the reactor core has a thermal power that is equivalent to the design specification, while a LF of 50% indicates that the reactor core is producing half as much thermal power as it was designed to produce. A LF for each reactor core is quoted on a monthly basis, giving good time variation information for all nuclear reactors.

It is desirable to have thermal power information on shorter timescales for the nuclear reactor cores that have the largest contributions to the flux at SNO+. The Independent Energy System Operator (IESO) publishes the electrical output of the nuclear reactors in Ontario on an hourly basis [97]. This actual electrical output can be compared to the maximum capability to define an equivalent to the LF. Figure 6.2 shows the agreement for a typical reactor core between the data provided by the IAEA (monthly) and the IESO (hourly), justifying the use of the electrical data.

The electrical data is published in hourly intervals but in practice it is sufficient to use a LF that is averaged over one calendar day. Over this timescale it is still possible to observe variations in the thermal output of the reactor cores on a daily basis while reducing the susceptibility to fluctuations in the thermal power output. Figure 6.3 shows an example of the evolution of the LF over one year for one of the Bruce reactor cores. The electrical output of the core is mostly stable throughout the year and two periods where the reactor core was shutdown can be seen. There is some instability after the second reactor shutdown, this slightly reduced output is reflected in the thermal power data from the IAEA but the day to day structure of the instability can only be seen in the electrical data.

The methods described thus far predict the number of antineutrinos produced at a

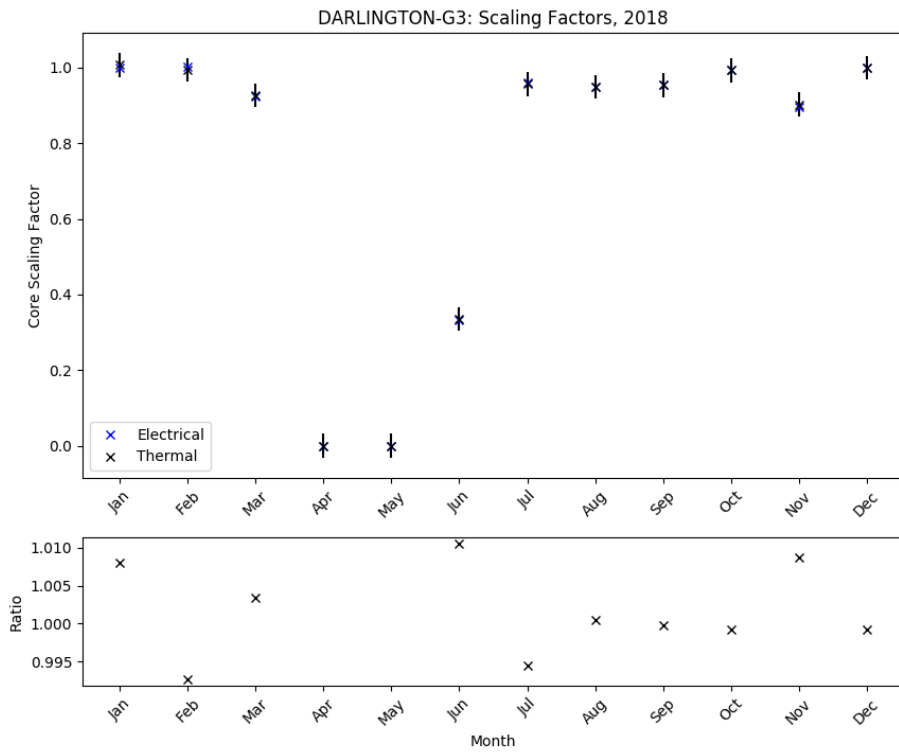


Figure 6.2: A comparison of the load factor quoted by the IAEA and the load factor calculated using the electrical data provided by the IESO for one of the Darlington reactor cores in 2018. The error bars are statistical only. The two data sets agree with each other in stable running periods as well as before and after reactor shutdown.

given nuclear reactor core. The antineutrinos will then propagate to the SNO+ detector. The antineutrinos are assumed to be emitted isotropically from the nuclear reactor core. Therefore, the flux at a given distance from the reactor core,  $R$ , follows as

$$I_{\bar{\nu}_e} = \frac{P_{\text{th}}}{4\pi R^2}. \quad (6.2)$$

The closest nuclear reactor complexes provide the largest contributions to the reactor antineutrino flux at SNO+. Figure 6.4 illustrates this by showing  $I_{\bar{\nu}_e}$  for the reactor complexes that are within 550 km of SNO+. The thermal power of each reactor core is scaled using Equation 6.2 to account for the isotropic nature of the antineutrino emission.

### 6.2.1.2 Reactor antineutrino oscillation

The reactor antineutrino flux described in Section 6.2.1.1 is calculated assuming that no neutrino oscillation occurs between the origin reactor and SNO+. The effect of oscillation

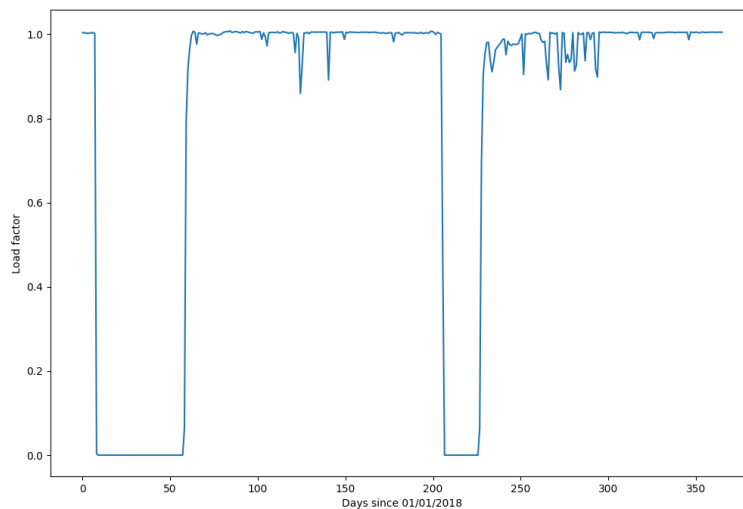


Figure 6.3: The evolution of the load factor for the Bruce-G1 core over 2018. Here two reactor shutdowns are visible along with some instability after the second reactor shutdown. Data provided by IESO [97].

must be applied by generating MC simulation comprising of IBD events according to the unoscillated neutrino flux and incorporating the survival probability of electron antineutrinos. This is advantageous as it allows for the events to be generated only once but various values of the oscillation parameters to be applied at a later point in time.

Oscillation is applied on an event by event basis. As described in Chapter 2 the two inputs to determine the antineutrino survival probability, excluding the oscillation parameters, are the antineutrino energy and the distance over which it travels. Both of these parameters are known as the MC truth information contains the parent antineutrino energy and the reactor core from which it originated. The survival probability of an electron antineutrino is calculated for each event and a random number [98] is thrown to decide if the event should be kept.

Figure 6.5 shows the predicted reactor antineutrino flux at SNO+ for two different sets of oscillation parameters, specifically two different values of  $\Delta m_{21}^2$ . The unoscillated predicted flux is also shown for comparison. It is clear that neutrino oscillation has a significant impact on the predicted flux. The flux has a strong dependence on the true value of  $\Delta m_{21}^2$  which allows SNO+ to make such a measurement.

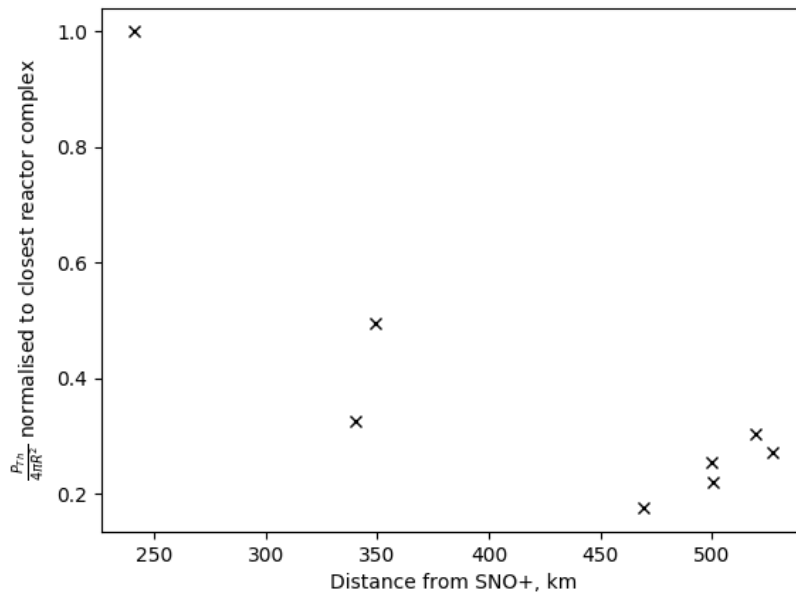


Figure 6.4: The intensity of the antineutrino flux for reactors within 550 km of SNO+. It is seen that the  $R^2$  term in Equation 6.2 leads to the closest reactors providing the greatest contribution to the flux.

### 6.2.1.3 Inverse beta decay

With the effects of neutrino oscillation applied to the reactor antineutrino flux the rate of interaction within the SNO+ scintillator can be estimated. This is achieved by considering the IBD cross section and the target number of protons within the SNO+ detector.

There are three main interaction channels for the detection of reactor antineutrinos: IBD, neutrino-electron elastic scattering and neutrino-nucleus coherent scattering. Of the three processes, neutrino-nucleus coherent scattering has the largest cross section at typical reactor antineutrino energies. IBD has a cross section that is approximately two orders of magnitude lower than that of the coherent scattering. Neutrino-electron elastic scattering has the smallest cross section, a further two orders of magnitude below IBD. A thorough review of neutrino cross sections is given in [99].

While the cross section of neutrino-nucleus coherent scattering is attractive for the detection of reactor antineutrinos it is not possible to detect this interaction channel in the SNO+ detector. The experimental signature consists of the recoil of the nucleus upon which the antineutrino is scattered. This recoil has an energy that is on the order of keV [100], a value below the threshold of SNO+. Neutrino-electron elastic scattering has an advantage over IBD in that the interaction is available for all flavours of neutrinos via a

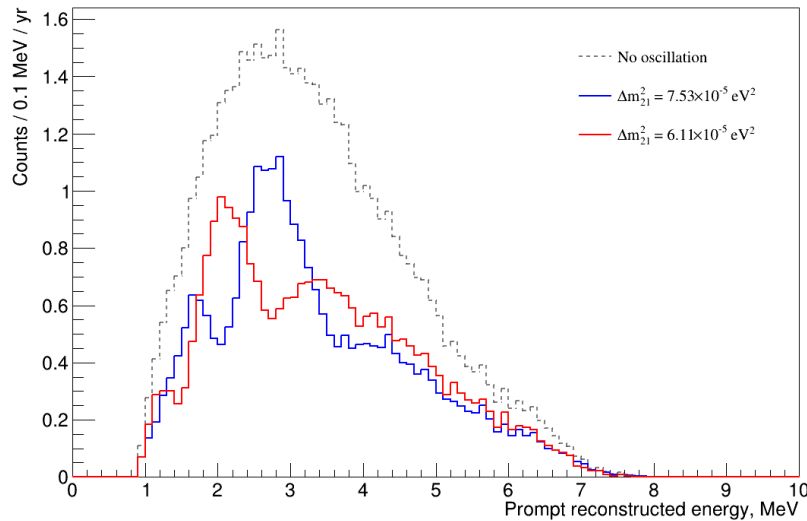


Figure 6.5: The expected reactor antineutrino flux at SNO+ in the partial fill phase. The oscillated flux for two different values of  $\Delta m_{21}^2$  corresponding to  $7.53 \times 10^{-5} \text{ eV}^2$  and  $6.11 \times 10^{-5} \text{ eV}^2$  are shown, along with the unoscillated flux.

neutral current process. In spite of this, IBD is the channel of interest for the detection of reactor antineutrinos due to the larger cross section and coincident event nature.

The IBD cross section is described in literature and the cross section calculation used in RAT is provided by Vogel and Beacom [101], defined as

$$\frac{d\sigma}{d\cos\theta} = \frac{\sigma_0}{2} [(f^2 + 3g^2) + (f^2 - g^2)\nu_e^{(1)} \cos\theta] E_e^{(1)} p_e^{(1)} - \frac{\sigma_0}{2} \left[ \frac{\Gamma}{M} \right] E_e^{(0)} p_e^{(0)}, \quad (6.3)$$

where  $f$  is the vector coupling constant,  $g$  is the axial coupling constant,  $E_e^{(1)}$  and  $p_e^{(1)}$  are expansions of the positron energy and momentum in  $\frac{1}{M}$ ,  $\nu_e$  is the positron velocity and  $\Gamma$  is a large additional term with no extra dependencies. A complete description of Equation 6.3 is given in the paper by Vogel and Beacom.

Of importance here is the normalisation constant,  $\sigma_0$ . This constant can be expressed in two ways using different components. The constant can be written in terms of the Fermi Coupling Constant,  $G_F$ , and the Cabibbo mixing angle,  $\theta_C$ , as

$$\sigma_0 = \frac{G_F^2 \cos^2 \theta_C}{\pi} (1 + \Delta_{\text{inner}}^R) \quad (6.4)$$

where  $\Delta_{\text{inner}}^R$  is a radiative correction term [102]. The normalisation constant can also be

Table 6.2: The current best values for the components of Equations 6.4 and 6.5. The relative uncertainty on  $G_F$  is the dominant term when calculating the total uncertainty for normalisation constants.

Quantity	Value	Relative uncertainty, %
$G_F$	$1.16639 \pm 0.0510 \times 10^{-11} \text{ MeV}^{-2}$ [37]	4.37
$\cos(\theta_C)$	$0.97450 \pm 0.00014$ [37]	0.01
$\Delta R_{\text{inner}}$	$0.02467 \pm 0.00022$ [104]	0.89
$f_{\text{p.s.}}^R$	$1.71517 \pm 0.00009$ [103]	$5.25 \times 10^{-3}$
$\tau_n$	$879.4 \pm 0.6 \text{ s}$ [37]	0.07
$m_e$	$0.5109989461 \pm 0.0000000031 \text{ MeV}$ [37]	$6.07 \times 10^{-7}$
f	1 [101]	-
g	$1.27641 \pm 0.00056$ [105]	0.04

expressed in terms of the neutron lifetime,  $\tau_n$ , and the electron mass,  $m_e$ , as

$$\sigma_0 = \frac{2\pi^2}{f_{\text{p.s.}}^R \tau_n m_e} \frac{1}{f^2 + 3g^2}, \quad (6.5)$$

where  $f_{\text{p.s.}}^R$  is a phase space factor [103]. Equations 6.4 and 6.5 evaluate to give constants that differ by approximately 0.38%. However, the uncertainty on each of the expressions is very different. The constant calculated with Equation 6.4 has an uncertainty of 8.54% while the constant calculated with Equation 6.5 has an uncertainty of 0.23%. This can be explained by the relative uncertainty of the components, specifically  $G_F$ , as shown in Table 6.2. The constituents of Equation 6.4 are relatively less well known than the constituents of Equation 6.5, leading to a larger uncertainty. As the two constants are consistent with each other it was decided to use the constant as defined in Equation 6.5 in order to quote a reduced cross section uncertainty.

The cross section gives the probability that IBD will occur when an antineutrino passes near a proton. The cross section must therefore be multiplied by the number of protons in the detector to get the probability of an interaction in the full detector volume. This probability is then multiplied by the antineutrino flux to get the total interaction rate.

The number of free protons in the SNO+ detector is determined by estimating the amount of hydrogen in the liquid scintillator. This is performed by considering the volume

of the AV and the density of LAB to calculate the mass of LAB in the detector. The volume of the AV is a fixed quantity (as a sphere with a 6 m radius) but the density of LAB is temperature dependent [57]. The SNO+ cavity is kept at approximately 13°C and is approximately uniform [106]. In the water phase there was a temperature difference of 3°C between the top and bottom of the cavity [107] and such a difference introduces a 0.2% uncertainty in the proton calculation, however recent measurements show a much more uniform temperature in the scintillator phase.

With the LAB at a temperature of 13°C the number of protons in the full detector volume is  $5.69 \times 10^{31}$ . In the partially filled phase with a reduced mass of LAB the number of protons is  $2.41 \times 10^{31}$ . With the number of protons and the IBD cross section known the interaction rate is therefore completely modelled in the SNO+ detector.

### 6.2.2 Geoneutrinos

Geoneutrinos, or more specifically geo antineutrinos, are antineutrinos that are produced within the crust and mantle of the Earth. These antineutrinos come from the uranium and thorium decay chains as well as the decay of  $^{40}\text{K}$  as discussed in Chapter 5. The antineutrinos produced by the uranium and thorium chains are of sufficient energy to be detected at SNO+. The geoneutrinos are treated as a background in the reactor oscillation analysis, however future analyses will measure the geoneutrino rate.

The expected geoneutrino flux is estimated in RAT by considering multiple geological models that describe the amount of uranium and thorium present in the Earth's crust and mantle. The antineutrino energy spectrum from these two decay chains is well known and is shown in Figure 6.6, with the normalisation (expected flux) dependent on the model considered.

There are three main models that are considered which each predict different geoneutrino fluxes due to different estimates of radiogenic heat production. The models each estimate the flux in Terrestrial Neutrino Units (TNU). A single TNU is defined as one IBD interaction in a one year livetime for  $10^{32}$  target protons. The models each predict fluxes for both the uranium chain and the thorium chain which are then summed to get a single geoneutrino flux prediction. The first main model is the “Cosmochemical” model. This is a “low-Q” model whereby the amount of U and Th in the Earth's mantle is predicted to be low and therefore approximately 10-15 TW of radiogenic heat is available. The second model is the “Geochemical” model. This is a “mid-Q” model, predicting a larger amount of U and Th leading to approximately 17-22 TW of radiogenic heat. The

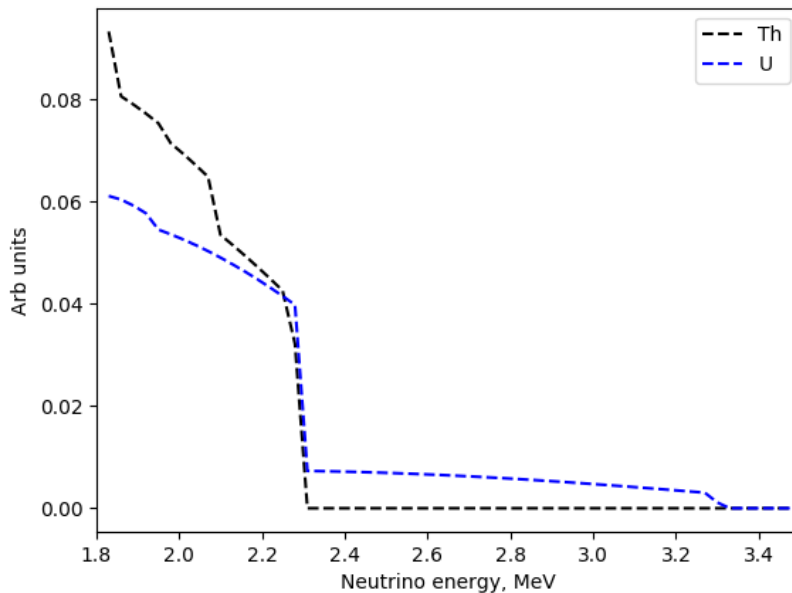


Figure 6.6: The antineutrino energy spectra from the U and Th decay chains that constitute the geoneutrino flux [108].

Table 6.3: The predicted geoneutrino flux for the low-Q, mid-Q and high-Q geological models [110]. 1 TNU is defined as a single IBD interaction in a full year exposure to  $10^{32}$  protons.

Chain	Low Q flux (TNU)	Mid Q flux (TNU)	High Q flux (TNU)
U	29.73	34.12	41.54
Th	8.21	9.53	11.4

final model is the “Geodynamical” model. This model is a “high-Q” model as it predicts the largest amount of U and Th in the mantle, giving greater than 25 TW of radiogenic heat. A description of the models and their impact on the neutrino flux is given by Šrámek et al [109]. The expected geoneutrino fluxes at SNO+ for these three models are shown in Table 6.3.

The geoneutrino flux has not yet been measured on the North American continent and measurements by other experiments (Borexino [111], KamLAND [36]) have not yet been able to distinguish between these three geological models. There are also large uncertainties in defining the models, for this reason SNO+ has adopted the mid-Q model to predict the geoneutrino flux. The uncertainty on this flux is taken as 100% to account

for the differences between the three models and the assumptions within them.

The fluxes given in Table 6.3 are combined with the number of protons in the detector, defined in Section 6.2.1.3. This allows the expected number of geoneutrino interactions in the full detector volume per 1 year of livetime to be calculated. A prediction can therefore be made for any given livetime.

### 6.2.3 $^{13}\text{C}(\alpha, n)^{16}\text{O}$

The  $^{13}\text{C}(\alpha, n)^{16}\text{O}$  interaction is the dominant background in the reactor antineutrino analysis. As described in Chapter 5 the rate of these interactions is directly dependent on the rate of  $^{210}\text{Po}$  decays in the detector, due to the inability to identify these  $\alpha$  particles by other means.

The  $^{210}\text{Po}$  rate has been measured in the SNO+ detector in both the partially filled phase and the full scintillator phase. The rate is calculated by performing a fit to the measured events at the energy of the  $^{210}\text{Po}$  decay. The  $\alpha$  emitted in this decay has an energy of 5.304 MeV [112], however due to quenching in the SNO+ scintillator the observed energy is approximately 0.4 MeV [113]. The  $^{210}\text{Po}$  rate in the partial fill is measured to be 0.24 Hz m<sup>-3</sup> [114], while the rate in the fully filled detector is lower at 0.08 Hz m<sup>-3</sup> [115], due to improvements in the filling procedure that reduced the amount of radon introduced into the detector. These improvements included an increase in the rate at which nitrogen was flowed through the primary gas stripping column, more efficiently removing impurities from the scintillator.

With the rate of  $\alpha$  particles that can initiate an interaction known, the cross section of the interaction must be considered, along with the amount of  $^{13}\text{C}$  present in the detector. This will determine the number of neutrons produced by the  $\alpha$  which will mimic the IBD signal. This can be calculated by using the thick target yield formula

$$Y = N_{^{13}\text{C}} \int_0^{E_\alpha} \frac{\sigma_E}{S_\alpha} dE, \quad (6.6)$$

where  $N_{^{13}\text{C}}$  is the number density of  $^{13}\text{C}$  atoms in the scintillator,  $\sigma_E$  is the energy dependent cross section of the interaction and  $S_\alpha$  is the stopping power of an  $\alpha$  in the scintillator.  $N_{^{13}\text{C}}$  is determined by the chemical composition of the scintillator.  $^{13}\text{C}$  has a natural abundance of 1.1% [116] and therefore it assumed that this value holds for the carbon that makes up the liquid scintillator.  $S_\alpha$  is provided by the SRIM software package [117].

The  $(\alpha, n)$  cross section is provided by the JENDL/AL-2005 library [118]. The cross

section is based on measurements performed by Sekharan et al [119] and Bair et al [120] and the cross section is shown in Figure 6.7. It is important to note that this is the total cross section. The  $^{13}\text{C}(\alpha, n)^{16}\text{O}$  interaction has three different mechanisms by which to occur, two of which are ground state interactions while the other leaves the  $^{16}\text{O}$  in an excited state. There are large uncertainties on the cross section, with the ground state cross sections having an uncertainty of 30% and the first excited state cross section having an uncertainty of 100%.

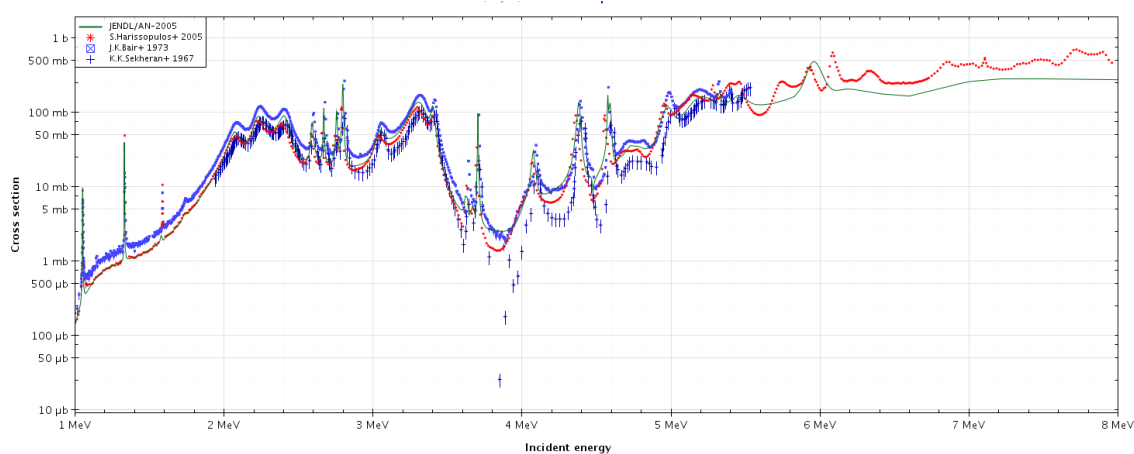


Figure 6.7: The total cross section for the  $^{13}\text{C}(\alpha, n)^{16}\text{O}$  interaction. This information is provided by the JENDL/AL-2005 libraries [118] and plotted using JANIS web [121].

The  $\alpha$  to neutron yield was calculated to be  $5.75 \pm 0.41 \times 10^{-8}$  using the same inputs for the cross section and stopping power as described above, for the Daya Bay liquid scintillator [122]. The scintillator used in Daya Bay has a  $^{13}\text{C}$  density of  $3.84 \times 10^{20}\text{cm}^{-3}$  [123], while the SNO+ scintillator was measured to have a density of  $4.19 \times 10^{20}\text{cm}^{-3}$  [113]. Therefore the  $\alpha$  to neutron yield is scaled by the ratio of the two densities to give a yield of  $6.27 \pm 0.44 \times 10^{-8}$ .

The measurement of the  $^{210}\text{Po}$  rate along with the calculation of the neutron yield allow the rate of  $^{13}\text{C}(\alpha, n)^{16}\text{O}$  interactions to be predicted. As described in Chapter 5 there are three main mechanisms that drive  $^{13}\text{C}(\alpha, n)^{16}\text{O}$  events. The majority of events are the ground state interactions, with a branching ratio of 0.908 used in RAT. The excited state interactions therefore have a branching ratio of 0.092. Furthermore the first excited state (deexcitation via  $e^+e^-$  pair emission) has a branching ratio of 0.88, while the second excited state (deexcitation via  $\gamma$ ) has a branching ratio of 0.12. It is noted that there are large uncertainties associated with these branching ratios, particularly the excited states [124]. The impact of these branching ratios on the prompt energy spectrum is shown in Section 6.4.

## 6.3 Signal selection

With the signal and the main backgrounds modelled from their sources to their manifestation in the detector it is possible to make predictions of what is expected in data. This involves the definition of analysis level cuts to apply to data events in order to best select the IBD signal.

### 6.3.1 Analysis cuts

As described in Chapter 5 the IBD signal is a clean coincident signal in both time and space in the detector. The energy of the delayed event is well known, as a neutron capture on a free proton will always produce a 2.2 MeV  $\gamma$ . Therefore these factors can be used to identify such events.

The data (or MC) events are subjected to the analysis cuts defined in Table 6.4, with a pair of events satisfying both the prompt event selection and delayed event selection constituting an IBD candidate. In practice, the position and energy delayed event cuts are applied to events until a delayed candidate event is found. The events in a time window corresponding to the  $\Delta T$  window preceding the delayed candidate are subjected to the prompt event cuts, along with the  $\Delta T$  and  $\Delta R$  cuts. If a valid prompt event is found then the penultimate check is a multiplicity cut, that is, there can be no other high energy events close to either of the candidate pair events within some time window. Finally, a muon veto is made whereby the candidate pair is rejected if there was an event with a very high  $N_{\text{hits}}$  in the previous 20 s. This cut is intended to remove any neutrons generated by muons [125]. If all these cuts are satisfied then these coincident events are an IBD candidate.

The analysis cuts defined in Table 6.4 are motivated by the initial measurement of reactor antineutrinos made at SNO+ [84]. All events are required to have a valid reconstruction such that the reconstructed quantities can be used. The energy of the prompt event is determined as the visible energy deposited in the scintillator for an IBD event. The visible energy threshold of IBD events is approximately 1 MeV, as described in Chapter 2. The delayed event energy is determined by the 2.2 MeV  $\gamma$  emission when a neutron undergoes capture on a free proton. The energy range is selected to account for the energy resolution and uncertainties in the energy scale of the detector, along with an observed reduction of hits at high radius in the detector [126]. The fiducial volume cuts are included so that background events from the AV can be ignored. In the partial fill phase a cut on

Table 6.4: The analysis cuts used to select IBD candidate event pairs in data and MC.

Cut	Prompt event	Delayed event	Efficiency, %
Valid reconstruction	True	True	88.2
Energy, MeV	$0.9 < E < 8$	$1.85 < E < 2.4$	77.6
Radius, m	$< 5.7$	$< 5.7$	65.4
Z position (partial fill only), m	$> 0.85$	$> 0.85$	63.6
$\Delta R$ , m		$< 1.5$	63.0
$\Delta T$		$400 \text{ ns} < \Delta T < 0.8 \text{ ms}$	61.5
Muon veto		20 s after event with $> 3000$ nhits	-
Multiplicity	$E > 0.4 \text{ MeV}$ and $\Delta R < 2 \text{ m}$ within 2 ms of event pair		-

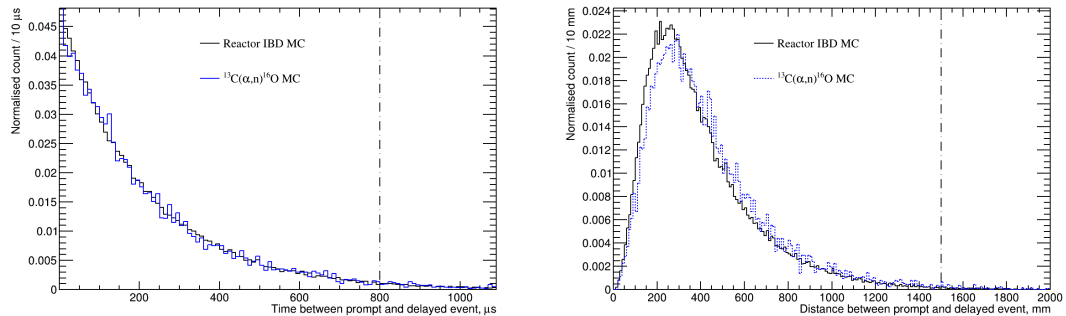
the position in the vertical direction is included to remove poorly reconstructed events near the water-scintillator interface.

The efficiency of the analysis cuts are also given in Table 6.4 as calculated using MC generated data. The leading contributions to the efficiency are the requirement for valid reconstruction and a suitable energy and position of both prompt and delayed events. The muon veto has no associated effect on the efficiency as this cut simply reduces the livetime of the dataset. The multiplicity cut was previously estimated to be negligible [84]. The purity of the event selection is not calculated as the efficiencies for IBD and  $^{13}\text{C}(\alpha, n)^{16}\text{O}$  events are almost identical and therefore the purity of an IBD sample is unchanged.

The  $\Delta R$  and  $\Delta T$  thresholds are placed to reduce the amount of accidental coincidences passing the analysis cuts. Accidental coincidences are a prompt and delayed event that satisfy all analysis cuts but the constituent events are completely unrelated. Accidental coincidences are uniformly distributed in both  $\Delta R$  and  $\Delta T$  while true IBD events are not, as shown in Figure 6.8. The capture time for neutrons on free protons is  $216\mu\text{s}$  [91]. Therefore an upper  $\Delta T$  threshold of 0.8 ms corresponds to approximately 4 half lives for the neutron capture, approximately 92.5% of events.

Table 6.5: The expected number of events in the partial fill phase, split by interaction type.

Signal	Events
Reactor IBD	9.4
Geoneutrino IBD	2.2
$^{13}\text{C}(\alpha, n)^{16}\text{O}$	33.3



(a) The  $\Delta T$  distribution for reactor IBD and (b) The  $\Delta R$  distribution for reactor IBD and  $^{13}\text{C}(\alpha, n)^{16}\text{O}$  MC events.

$^{13}\text{C}(\alpha, n)^{16}\text{O}$  MC events.

Figure 6.8: The  $\Delta T$  and  $\Delta R$  distributions for reactor IBD and  $^{13}\text{C}(\alpha, n)^{16}\text{O}$  MC events. The vertical dashed black lines correspond to the upper threshold on the cut.

## 6.4 Prediction

The techniques described in this chapter culminate in the predictions of the number of signal and background events in a given livetime, along with the prompt energy spectrum. Predictions are made for the partially filled phase, with a known livetime, and the fully filled scintillator phase.

### 6.4.1 Partially filled phase

The predicted number of events in the partially filled phase are shown in Table 6.5. This corresponds to a livetime of 130.2 days [84]. As this is the partially filled phase, the Z positional cut in Table 6.4 is also applied.

The energy spectrum of the prompt events is shown in Figure 6.9. Here the impact of the large number of  $^{13}\text{C}(\alpha, n)^{16}\text{O}$  events is clearly visible, particularly if a geoneutrino measurement was desired. The  $^{13}\text{C}(\alpha, n)^{16}\text{O}$  spectrum can be split by the three main

mechanisms described in Chapter 5 (Figure 5.3). The events with a prompt energy below 3.5 MeV are ground state interactions where the photons are produced by recoiling protons, due to the neutron moving through the scintillator. The events centered around the peak at 4.4 MeV are also ground state interactions, but the neutron inelastically scatters off a  $^{12}\text{C}$  and produces a 4.4 MeV  $\gamma$ . Finally, the higher energy events centered around 6 MeV are the excited state interactions, with deexcitation occurring via both  $e^+e^-$  emission and  $\gamma$  emission.

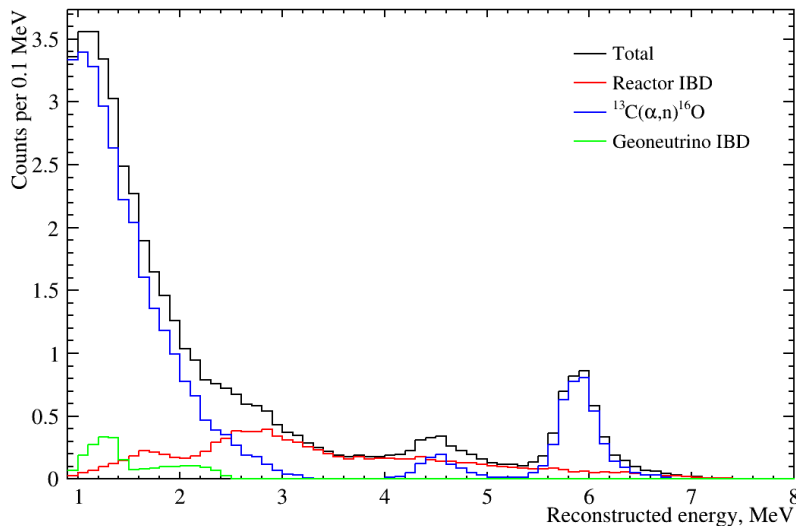


Figure 6.9: The predicted prompt energy spectrum after applying analysis cuts in the partial fill phase. The distributions are normalised according to the predicted event counts in Table 6.5.

#### 6.4.2 Fully filled scintillator phase

The predicted number of events in the fully filled scintillator phase are shown in Table 6.6. As data taking in this phase is ongoing the predictions are made for exactly 1 full year of livetime. The vertical positional cut in Table 6.4 is no longer applied as there is no water-scintillator interface in the detector.

Once again the energy spectrum of the prompt events is shown in Figure 6.10. The  $^{13}\text{C}(\alpha, n)^{16}\text{O}$  prediction used the lower  $^{210}\text{Po}$  rate as discussed in Section 6.2.3. The relative amount of  $^{13}\text{C}(\alpha, n)^{16}\text{O}$  events is clearly reduced here when compared to the partial fill phase which benefits both the reactor oscillation analysis and any measurement of geoneutrinos.

Table 6.6: The expected number of events in the fully filled scintillator phase, split by interaction type.

Signal	Events
Reactor IBD	80.80
Geoneutrino IBD	19.30
$^{13}\text{C}(\alpha, n)^{16}\text{O}$	87.40

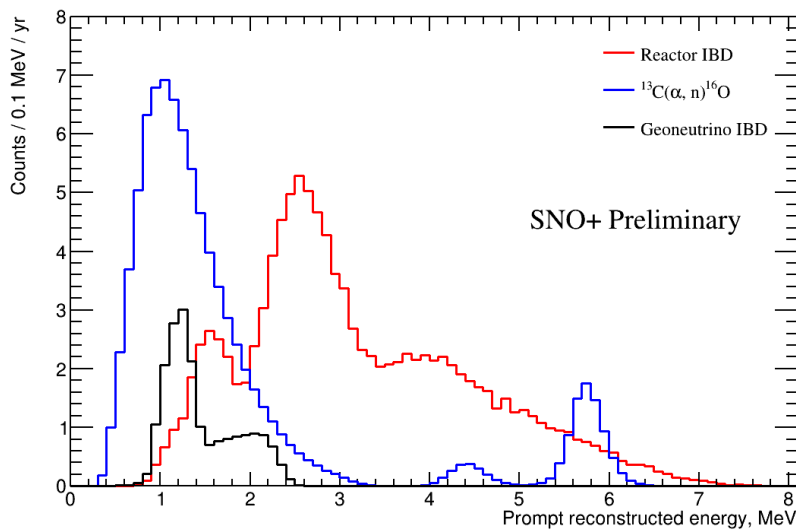


Figure 6.10: The predicted prompt energy spectrum after applying analysis cuts in the full scintillator phase. The distributions are normalised according to the predicted event counts in Table 6.6.

## 6.5 Conclusion

The modelling and prediction of the reactor IBD signal and the main backgrounds is a vital component of the reactor oscillation analysis. The reactor antineutrino signal is composed of many different inputs which have been summarised in this chapter. The effects of neutrino oscillation on antineutrinos produced at nuclear reactors has been quantified and the expected prompt event energy spectrum shown. The models used to make predictions for the dominant  $^{13}\text{C}(\alpha, n)^{16}\text{O}$  background and the geoneutrino background have been outlined. The impact of the  $^{210}\text{Po}$  rate on the background prediction is considered, as demonstrated by comparing the prediction in the partially filled phase and the full scintillator phase.

# Chapter 7

## Reactor antineutrino oscillation

### 7.1 Introduction

The ability to detect reactor antineutrinos at SNO+ leads to the development of an analysis to extract the oscillation parameters  $\Delta m_{21}^2$  and  $\theta_{12}$ . Such an analysis is performed by comparing the energy spectrum of prompt IBD candidate events to the predicted spectrum produced from MC events. The spectrum produced using MC events can be varied by assuming different values of  $\Delta m_{21}^2$  and  $\theta_{12}$ . The parameters that best match the data are extracted.

As described in previous chapters, the coincident IBD signal in the detector leads to excellent background rejection. The remaining backgrounds for the reactor antineutrino oscillation analysis are IBD events initiated by geoneutrinos and  $^{13}\text{C}(\alpha, n)^{16}\text{O}$  interactions. The expected contribution of these two backgrounds must be accounted for as nuisance parameters when performing the oscillation analysis. This chapter describes an analysis to extract oscillation parameters while taking into account the dominant backgrounds.

### 7.2 Oscillation parameter extraction

The antineutrino analysis measures the neutrino oscillation parameters by performing a maximum likelihood fit to the prompt energy spectrum of candidate IBD events. As discussed in Chapter 5 the true values of  $\Delta m_{21}^2$  and  $\theta_{12}$  impact the prompt energy spectra of reactor antineutrinos. Therefore PDFs describing the signal and background contributions, along with the expected normalisations of these PDFs, can be fit to the data spectrum.

The oscillation analysis is performed in two steps. The first stage involves the fitting of the data to maximise the likelihood with respect to the parameters in the fit and this is done for each set of oscillation parameters. The fit parameters are the normalisations

(expected event counts) of the different PDFs. The fit is performed as a binned extended maximum likelihood fit, whereby the likelihood function to maximise is

$$\log(\mathcal{L}(n_{\text{obs}})) = \sum_{i=0}^{N_{\text{bins}}} n_{\text{obs}}^i \log\left(\sum_{j=0}^{N_{\text{PDFs}}} N_j P_j^i\right) - \sum_{j=0}^{N_{\text{PDFs}}} N_j, \quad (7.1)$$

for  $N_{\text{PDFs}}$  with  $N_{\text{bins}}$ .  $n_{\text{obs}}^i$  is the observed number of events in the  $i$ th bin,  $N_j$  is the normalisation constant of the  $j$ th PDF and  $P_j^i$  is the normalised content of the  $i$ th bin in the  $j$ th PDF. The normalisation constants are allowed to float in some range around their expected values, discussed in more detail in Section 7.2.2. This fit is performed for many combinations of the oscillation parameters with the maximum likelihood with respect to the fit parameters, for each set of oscillation parameters, recorded.

The second stage is to select the set of oscillation parameters that give the maximum likelihood. A likelihood ratio test is performed for all oscillation parameters against the selected maximum likelihood,  $\log(\mathcal{L}(\Delta m_{21}^2, \hat{\theta}_{12}))$ , as

$$\Delta \log(\mathcal{L}) = \log\left(\frac{\mathcal{L}(\Delta m_{21}^2, \theta_{12})}{\mathcal{L}(\Delta m_{21}^2, \hat{\theta}_{12})}\right), \quad (7.2)$$

where  $\log(\mathcal{L}(\Delta m_{21}^2, \theta_{12}))$  is the maximised log likelihood for given  $\Delta m_{21}^2$  and  $\theta_{12}$  values. By Wilks' theorem, the result of Equation 7.2 multiplied by -2 is  $\chi^2$  distributed [127]. Therefore the quantity  $-2\Delta \log(\mathcal{L})$  can be used to determine the uncertainties associated with the best fitting oscillation parameters to various confidence limits. The  $1\sigma$  limits are typically taken as uncertainties on the measured oscillation parameters.

The fitting routine is implemented by using the tools provided in the RooFit package. The component PDFs are defined as RooHistPDF objects and then summed into a single RooAddPDF object. Each constituent PDF has a corresponding normalisation parameter, defined as a RooRealVar, which can float in some defined range and is described in more detail in Section 7.2.2. The data points are then fit using Minuit as the minimisation routine.

### 7.2.1 PDFs of components

The likelihood described in Equation 7.1 uses component PDFs to fit the data. These PDFs correspond to the expected signals in the data: the antineutrinos from nuclear reactors, the  ${}^{13}\text{C}(\alpha, n){}^{16}\text{O}$  events and geoneutrinos. The PDFs are generated using simulated MC events with many orders of magnitude larger statistics than expected from data.

### 7.2.1.1 Reactors

The reactor PDFs are generated by selecting MC events that pass all the analysis cuts described in Chapter 6. A record of the nuclear reactor core in which these events were simulated to have originated from is stored in the MC truth information. Therefore PDFs corresponding to different nuclear reactor cores can be built up.

While all operational reactor cores in the world are simulated in RAT, it was chosen to generate individual PDFs for only the nuclear reactor cores located within 1000 km of SNO+. There are 34 reactor complexes located within this distance of SNO+ and their power and distance away from SNO+ are described in Appendix C. Additionally it was chosen to group all reactor cores that are located at the same complex into one single PDF to simplify the analysis. To illustrate this, there are six reactor cores at the Pickering reactor complex but a single PDF is used that corresponds to events from all cores combined, as shown in Figure 7.1.

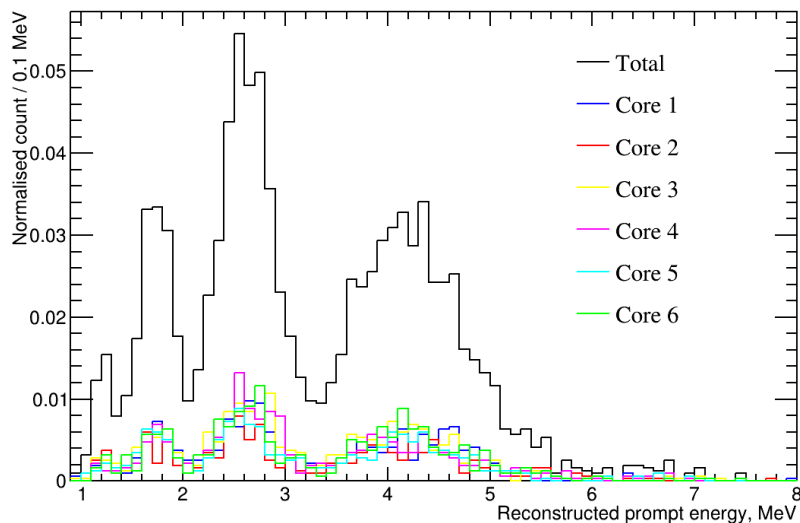


Figure 7.1: The PDF used in the likelihood fitting routine for the Pickering reactor complex. The component PDFs corresponding to the six reactor cores at this complex are also shown.

### 7.2.1.2 Geoneutrino

The geoneutrino PDF is generated using MC simulated events by applying the analysis cuts to identify surviving events. As described in Chapter 6 the geoneutrino spectrum arises due to the  $\beta$  decay of elements forming the uranium and thorium decay chains that are present in the Earth's mantle and crust. For the purposes of this analysis a single

PDF corresponding to events from both decay chains was adopted. This was chosen as the rate of geoneutrino events is small and there will be insufficient events to distinguish the two sources of geoneutrinos.

### 7.2.1.3 $^{13}\text{C}(\alpha, n)^{16}\text{O}$

As with the reactor and geoneutrino PDFs, the  $^{13}\text{C}(\alpha, n)^{16}\text{O}$  PDFs are generated using MC simulated events. The  $^{13}\text{C}(\alpha, n)^{16}\text{O}$  spectrum is split into three component PDFs, corresponding to the three different mechanisms by which the interaction can proceed as described in Chapter 6. Figure 7.2 shows the three component PDFs, normalised such that the sum of the integrals of all three PDFs is unity.

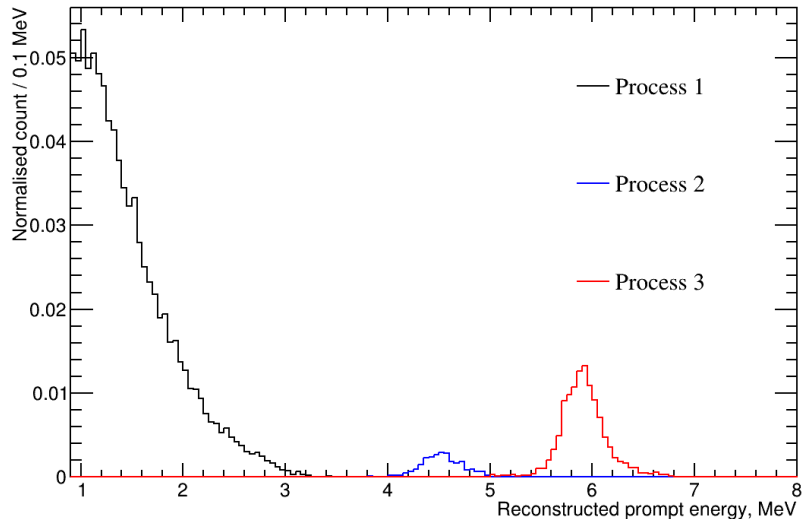


Figure 7.2: The three PDFs used in the likelihood fitting routine for the  $^{13}\text{C}(\alpha, n)^{16}\text{O}$  events. The three PDFs correspond to the three mechanisms by which the interaction can proceed.

The spectrum was split in this way for two reasons. Firstly, the  $^{16}\text{O}$  excited state interactions (process 3) are treated separately from the ground state interactions as the branching ratio has a large uncertainty, as described in more detail in Section 7.2.2. Secondly, the technique to reduce the  $^{13}\text{C}(\alpha, n)^{16}\text{O}$  background, described in Section 8.2, is only valid for proton recoil events (process 1). Therefore each mechanism can be treated individually by splitting the spectrum in this way.

### 7.2.2 Constraints

The PDFs described in Section 7.2.1 are the components that make up the predicted shape of the prompt energy spectrum. The relative contribution of each component is an input to the fit routine. These contributions are subject to systematic uncertainties and therefore they must be passed as floating parameters to the fit procedure. The allowed range in which these values can float are defined by the associated systematic uncertainties.

The uncertainty on the predicted number of reactor IBD events has multiple sources. Firstly, there is a 2.7% uncertainty associated with the antineutrino emission spectra from nuclear reactor cores [128]. The relative fractions of the fissile material in reactor fuels, described in Chapter 6, have an uncertainty of 0.6% [128]. The overall flux normalisation has been measured by multiple other experiments and the Daya Bay collaboration reports a correction factor of 0.95 to the flux, with a 0.7% uncertainty on this factor [128]. The power scaling factor that is applied to each reactor core, reflecting the time variable thermal power, has an uncertainty of 0.5%. Additionally, spent nuclear reactor fuel is typically stored on, or nearby, the nuclear reactor complexes from which they came. This spent fuel is still radioactive and will produce antineutrinos. This introduces a 0.3% uncertainty to the reactor flux [128].

Secondly, the uncertainties in the neutrino oscillation parameters are propagated through the oscillation formula, described in Equation 2.36. The oscillation analysis is designed to measure  $\Delta m_{21}^2$  and  $\theta_{12}$ , with the other three parameters held constant. By assuming symmetric errors for  $\Delta m_{32}^2$  and  $\sin^2(\theta_{13})$  the uncertainty in the oscillation probability propagates as 3.2%.

Finally, the IBD cross section has an uncertainty on the order of 0.7%. As discussed in Chapter 6 this uncertainty is greatly reduced, by an order of magnitude, by employing the normalisation constant that is calculated using the free neutron lifetime rather than the Fermi coupling constant. Combining the described uncertainties gives an overall uncertainty on the reactor normalisation of 4.4%.

The three  $^{13}\text{C}(\alpha, n)^{16}\text{O}$  PDFs can each have their own associated uncertainty in their normalisation. The dominant uncertainty for these events is in the cross section for the ground state events (processes 1 and 2) and the branching ratio for the excited state events. There are multiple measurements of the  $^{13}\text{C}(\alpha, n)^{16}\text{O}$  cross section, with varying degrees of disagreement [119], [120], [129]. The recent publication by Febbraro et al [124] evaluate the expected  $^{13}\text{C}(\alpha, n)^{16}\text{O}$  predictions for the KamLAND detector using their updated cross section measurements. The ground state prediction is reduced by approximately

Table 7.1: The uncertainties of the components in the oscillation analysis. The reactor uncertainty has multiple inputs, while the geoneutrino and  $^{13}\text{C}(\alpha, n)^{16}\text{O}$  interactions are assigned conservative uncertainties.

Reactor	Uncertainty, %	$^{13}\text{C}(\alpha, n)^{16}\text{O}$	Uncertainty, %	Geoneutrino	Uncertainty
Fixed oscillation parameters	3.2	Ground state proton recoil	30	Flux models	100
Emission spectra	2.7	Ground state neutron scattering	30		
IBD cross section	0.7	Excited state	100		
Flux correction	0.7				
Fissile fuel fractions	0.6				
Thermal power output	0.5				
Stored spent fuel	0.3				
Total	4.4				

8%, with an approximate 15% uncertainty on the prediction, compared to the prediction quoted by KamLAND [130]. It was decided for the purposes of this analysis to assign an uncertainty of 30% to the ground state interactions. It is recognised that this may be overly cautious and further work to reduce this uncertainty will take place in future analyses.

The cross section for the excited state interactions have a larger uncertainty when considering the predictions of Febbraro et al., with an approximate 29% uncertainty on a prediction that is reduced by 54%. This large uncertainty coupled with the poorly known branching ratio to the excited states results in the adoption of a 100% uncertainty for the third  $^{13}\text{C}(\alpha, n)^{16}\text{O}$  PDF corresponding to process 3.

The expected number of events from geoneutrinos is not well predicted, as discussed in Chapter 6. There are various models describing the relative amounts of uranium and thorium in the Earth’s mantle and crust. The lack of a high statistics measurement of geoneutrinos means that none of the three described models in Chapter 6 are disfavoured. The geoneutrino contribution is therefore conservatively assigned a 100% uncertainty. The uncertainties are summarised in Table 7.1.

It is noted that only systematic uncertainties affecting the antineutrino flux and  $^{13}\text{C}(\alpha, n)^{16}\text{O}$  rate are considered in this analysis. There are uncertainties affecting the shape of the energy distribution that are not included here. There are two main contributions to shape systematic uncertainties: energy scale and energy resolution. The uncertainty in the energy scale arises due to a reliance on calibration data when performing the conversion from  $N_{\text{hits}}$  to energy in the reconstruction algorithm, described in Chapter 3. The impact of an energy scale factor that deviates from unity is a distortion in

the prompt energy spectrum whereby the peaks and troughs of the spectrum are shifted. The energy resolution of the detector is a measure of how precisely the energy of an event can be measured. A given event will be reconstructed with an energy that will lie in some range, determined by the energy resolution, around the true value. This manifests as a smearing of the prompt energy spectrum which can lead to a reduction in definition of features in the spectrum.

The true value of  $\Delta m_{21}^2$  dictates the shape of the energy spectrum and therefore the shape uncertainties will impact the measurement of this parameter. These uncertainties are not included in this analysis as the short livetime in the partial fill leads to the assumption that statistical uncertainties will dominate any measurement of  $\Delta m_{21}^2$ . It is recognised that systematic uncertainties affecting the shape of the prompt energy spectrum will need to be accounted for when this analysis is performed on a larger dataset.

### 7.2.3 Results in partial fill

The fit routine described in this chapter was developed to perform a fit to data to extract the oscillation parameter  $\Delta m_{21}^2$ . The fit can be used for both MC simulated data and real IBD candidates. In both cases, the data is stored as a histogram of the prompt energy and this is fit using the PDFs described earlier in the chapter.

#### 7.2.3.1 MC data

When analysing MC data sets a distribution known as the “Asimov” data set is used. The Asimov dataset, coined by Glen Cowan [131] and inspired by the Isaac Asimov story *Franchise*, is a histogram where each bin has content equal to the expected number of events from each of the contributing interactions. That is, the expected number of IBD and  $^{13}\text{C}(\alpha, n)^{16}\text{O}$  events for a given bin is calculated and the bin content set to this value. An example of an Asimov data set for the prediction corresponding to 130 days of live time, along with the contributing distributions, has been shown in Figure 6.9. In reality, the Asimov data set will not be observed in data due to statistical fluctuations, rather it is the underlying predicted energy spectrum.

The oscillation analysis leaves  $\Delta m_{21}^2$  and  $\theta_{12}$  as free parameters and thus the output of the analysis is a phase space like that shown in Figure 7.3. By evaluating Equation 7.2 the exclusion contours corresponding to various confidence limits are drawn. In the case of Figure 7.3 there are insufficient statistics to produce a clear solitary  $1\sigma$  contour and so 25%, 50% and  $1\sigma$  exclusion limits are drawn.

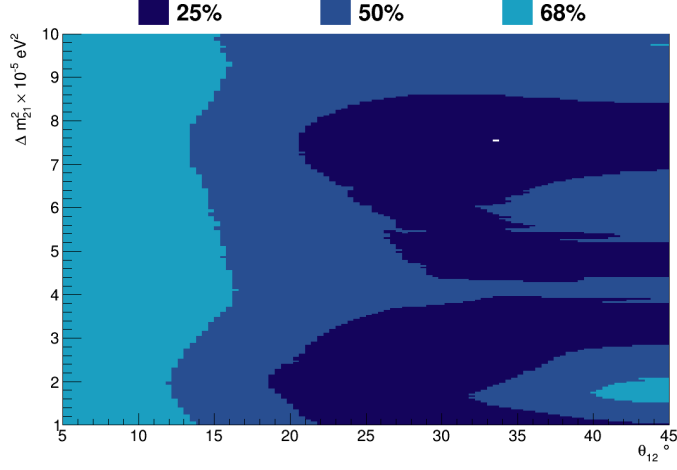


Figure 7.3: The likelihood phase space for  $\Delta m_{21}^2$  and  $\theta_{12}$  for an Asimov data set in the partially filled phase. The number of IBD events is insufficient to produce a solitary  $1\sigma$  contour. Confidence limits of 25%, 50% and  $1\sigma$  are drawn so that the structure of the space is revealed. The best fit is  $\Delta m_{21}^2 = 7.54 \times 10^{-5} \text{ eV}^2$ ,  $\theta_{12} = 33.6^\circ$ .

SNO+ as a reactor oscillation experiment is most sensitive to  $\Delta m_{21}^2$  and therefore it is useful to look at a 1D slice of the likelihood space by fixing  $\theta_{12}$  to the global value. Figure 7.4 shows an example of the likelihood space for  $\Delta m_{21}^2$  by fixing  $\theta_{12} = 33.467^\circ$ . While there are insufficient statistics to determine a single central value with  $1\sigma$  limits, it can be seen how such a value could be extracted from this plot, given that the y axis is  $\chi^2$  distributed with one degree of freedom.

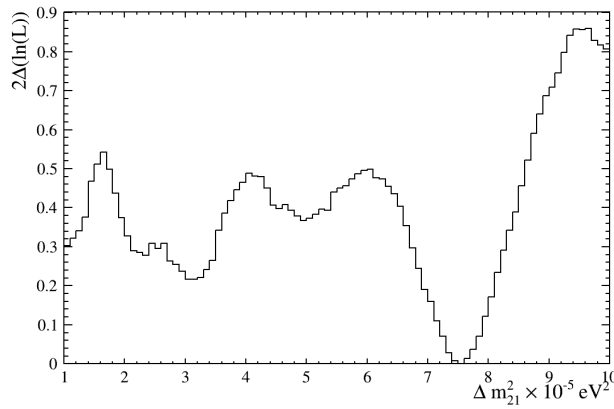


Figure 7.4: The likelihood space for  $\Delta m_{21}^2$  with  $\theta_{12} = 33.467^\circ$  fixed in the partially filled phase. With sufficient data a central value of  $\Delta m_{21}^2$  with upper and lower bounds can be extracted.

The 1D likelihood space like that of Figure 7.4 is extremely useful for evaluating the

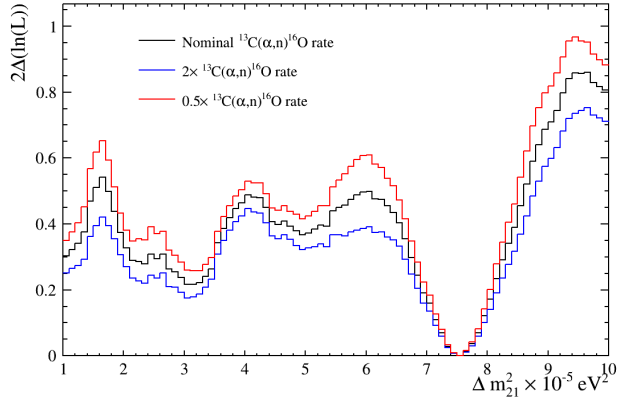


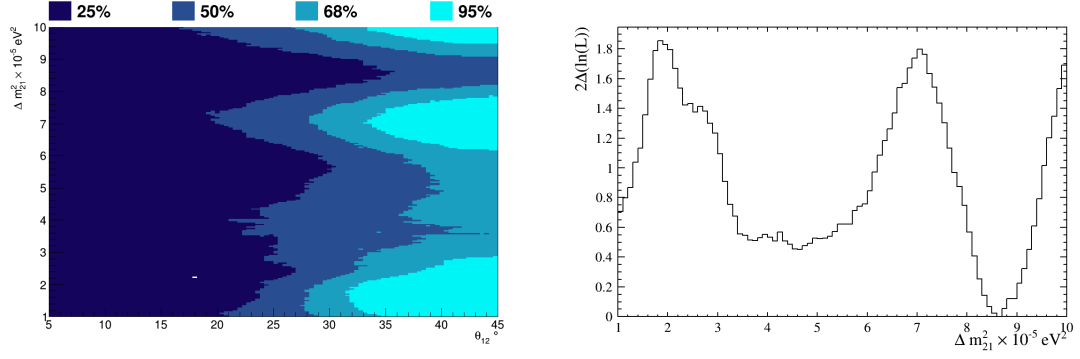
Figure 7.5: The likelihood space for  $\Delta m_{21}^2$  with varying rate of  $^{13}\text{C}(\alpha, n)^{16}\text{O}$  events. This is the dominant background in the analysis and the impact on the oscillation fit result is large.

impact of the background rates on the  $\Delta m_{21}^2$  sensitivity. Multiple Asimov data sets can be generated corresponding to different rates of  $^{13}\text{C}(\alpha, n)^{16}\text{O}$  events and the oscillation analysis performed. Figure 7.5 shows the impact on the likelihood space for  $\Delta m_{21}^2$  when the  $^{13}\text{C}(\alpha, n)^{16}\text{O}$  rate is changed by a factor of two while keeping the IBD rate constant. It can be seen that an increase of  $^{13}\text{C}(\alpha, n)^{16}\text{O}$  events negatively impacts the fit result. Conversely a decrease of those events improves the likelihood space for  $\Delta m_{21}^2$ . Therefore a technique to reduce the rate of  $^{13}\text{C}(\alpha, n)^{16}\text{O}$  events while preserving the IBD signal will improve the sensitivity of the analysis to  $\Delta m_{21}^2$ .

### 7.2.3.2 IBD candidates

The oscillation analysis is designed so that it can be performed on IBD candidate events identified in data. The partially filled period yielded 130.19 days of physics data available for analysis. When applying the analysis cuts described in Chapter 6 a total of 45 IBD candidate events were identified [84], [132]. This selection is in excellent agreement with the prediction of  $44.9 \pm 12.7$  events.

Figure 7.6 shows the  $\theta_{12}$  and  $\Delta m_{21}^2$  likelihood phase space for the events identified in data, as well as the 1D slice for  $\Delta m_{21}^2$  given  $\theta_{12} = 33.467^\circ$ . Due to the statistically limited nature of this data set a single central value for  $\Delta m_{21}^2$  is not reached, as predicted with the Asimov data set. Similarly, a single  $1\sigma$  contour is not defined in the 2D likelihood space. Nonetheless, this acts as a verification that the oscillation parameters can be extracted from IBD candidates identified in data.



(a) The likelihood phase space for  $\Delta m_{21}^2$  and  $\theta_{12}$ . (b) The  $\Delta m_{21}^2$  slice at  $\theta_{12} = 33.467^\circ$ .

Figure 7.6: The oscillation fit result for the observed IBD candidates in the partially filled phase. The data set is statistically limited and therefore no central value of  $\Delta m_{21}^2$  is reached. The best fit is  $\Delta m_{21}^2 = 2.22 \times 10^{-5} \text{ eV}^2$ ,  $\theta_{12} = 18.0^\circ$ .

### 7.3 Conclusion

It has been demonstrated that a maximum likelihood fitting routine has been developed to extract  $\Delta m_{21}^2$  and  $\theta_{12}$  from IBD candidate events identified in SNO+. The prompt energy spectrum of events is fit to predicted spectra generated using MC events corresponding to varying values of the oscillation parameters. The fitting routine can also be evaluated using “Asimov” data sets obtained from MC events. The fit result can be viewed in a 2D phase space for both oscillation parameters or one of the parameters can be fixed to extract a measurement of the other.

The analysis is performed for both MC generated data sets and a small sample of IBD candidate events identified in data. The resulting likelihood space for the data sample is consistent with expectation. It was also shown that the rate of the  $^{13}\text{C}(\alpha, n)^{16}\text{O}$  background events significantly impacts the sensitivity of the reactor antineutrino oscillation analysis.

## Chapter 8

# Improved sensitivity via identification of $^{13}\text{C}(\alpha, n)^{16}\text{O}$ events

### 8.1 Introduction

The sensitivity of the reactor antineutrino oscillation analysis shown in Chapter 7 is largely dominated by the rate of  $^{13}\text{C}(\alpha, n)^{16}\text{O}$  background events. The analysis is also statistically limited due to the long live time needed to observe a large number of antineutrinos at long baselines from nuclear reactors. Therefore an effective way to improve the sensitivity of the analysis is by reducing the background rate while preserving the signal events.

A technique to mitigate a large fraction of this background in the low energy region of the spectrum will be introduced and motivated in this chapter. The physics that underpins the technique will be verified using MC simulation. The impact of the background suppression on the oscillation analysis will be demonstrated for both MC generated data and a small sample of real IBD candidates.

### 8.2 $^{13}\text{C}(\alpha, n)^{16}\text{O}$ prompt event topology

As was seen in Section 7.2 the rate of  $^{13}\text{C}(\alpha, n)^{16}\text{O}$  events significantly impacts the sensitivity of SNO+ to the oscillation parameters of interest. A method to reduce this background will allow a more competitive measurement of  $\Delta m_{21}^2$  to be made with a shorter livetime. The prompt events of low energy  $^{13}\text{C}(\alpha, n)^{16}\text{O}$  and IBD events show a small difference in their time profiles which can be exploited to discriminate between the two event types. In this case “low energy” is defined as prompt events with a reconstructed energy that is less than 3.5 MeV.

The different mechanisms by which the  $^{13}\text{C}(\alpha, n)^{16}\text{O}$  and IBD interactions proceed were discussed in Chapter 5. In this analysis only the first interaction method for  $^{13}\text{C}(\alpha, n)^{16}\text{O}$  events is considered, that is, the interactions by which the prompt event arises due to recoiling protons. This contrasts to the IBD events whereby the prompt event is due to energy deposition and annihilation  $\gamma$ s from a positron. The remaining two processes for the  $^{13}\text{C}(\alpha, n)^{16}\text{O}$  events result in  $\gamma$  or  $e^+e^-$  emission, similar to that of IBD.

There are two fundamental differences that will be discussed in this section: protons and positrons/ $\gamma$ s have different scintillation time profiles, and multiple protons can recoil after interaction with the neutron across a relatively long timescale. These two facts give rise to the different event time profiles that can be used for event classification.

### 8.2.1 Interactions in simulation

The behaviour of the neutrons in  $^{13}\text{C}(\alpha, n)^{16}\text{O}$  events were investigated using MC truth information. Firstly the origin of the photons in the prompt event were used to verify that the mechanisms described in Chapter 5 are simulated as expected. Figure 8.1 shows the fraction of PMT hits where the photon that caused the hit originated from different possible particles. It shows that the photons in the high energy events are produced by  $\gamma$ s, while the low energy events are driven by protons. It should also be noted that in the very low energy events the contribution due to the  $\alpha$  itself becomes non-negligible.

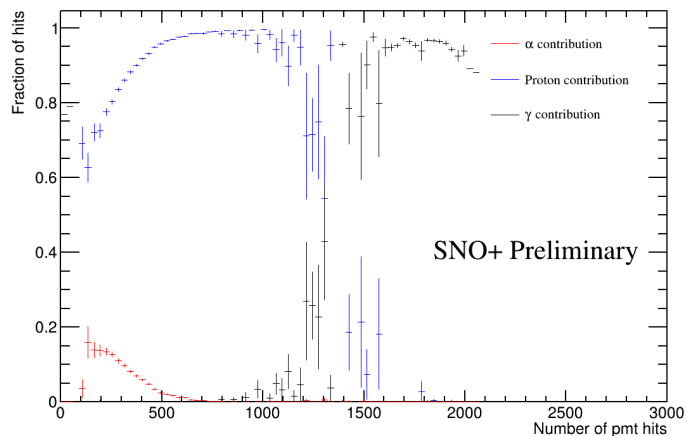


Figure 8.1: The fraction of particles producing photons that cause PMT hits in MC events. The photons in higher energy events are produced by  $\gamma$ s while the lower energy events have photons produced by protons. In the very low energy events the  $\alpha$  itself has a non-negligible contribution to the PMT hits.

The MC truth information for the protons in the low energy prompt events can be

used to verify that the neutron and protons in the scintillator are simulated as expected. Figure 8.2 shows that multiple protons are scattered by the neutron in MC events. A particle track is only generated in RAT if such a particle is involved in an interaction and therefore the number of protons generated by the neutron can be counted. The mean number of protons scattered in these events is 6.1.

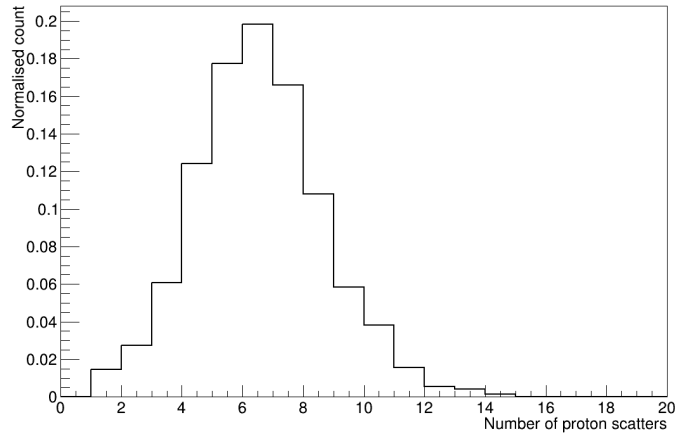


Figure 8.2: The number of scattered protons in low energy  $^{13}\text{C}(\alpha, n)^{16}\text{O}$  events. The mean number of protons scattered in such an event is 6.1.

Furthermore, Figure 8.3 shows the time at which the protons are scattered relative to the  $\alpha$ - $^{13}\text{C}$  interaction. It can be seen that the distribution is exponential in nature with a mean scatter time of  $7.5 \pm 1.2$  ns. Therefore not only are multiple protons scattered in low energy  $^{13}\text{C}(\alpha, n)^{16}\text{O}$  prompt events but the scattering interactions can occur on timescales of the order of tens of nanoseconds after the initial  $\alpha$  interaction. The multi-site nature of the prompt events gives rise to a longer time profile for  $^{13}\text{C}(\alpha, n)^{16}\text{O}$  prompt events.

### 8.2.2 Proton timing calibration

The scattering of multiple protons across long timescales is not the only contributing factor to the difference in time profiles. The scintillation time profile of protons is also fundamentally different to that of positrons. At the time of writing, SNO+ has no direct external measurement of the proton scintillation time profile. Instead a tuning of the scintillation time profile in RAT was performed using a pure sample of  $^{13}\text{C}(\alpha, n)^{16}\text{O}$  events. The tuned distribution was verified using neutrons produced by the  $^{241}\text{Am}^9\text{Be}$  calibration source.

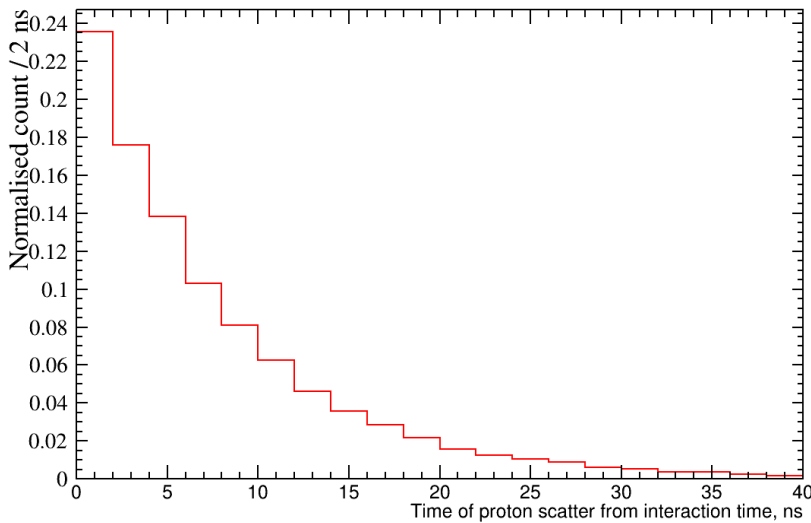


Figure 8.3: The time at which protons are scattered relative to the initial  $\alpha - ^{13}\text{C}$  interaction. The distribution has a mean scatter time of  $7.5 \pm 1.2$  ns.

Table 8.1: The  $\alpha$  and  $\beta$  scintillation time constants in the partially filled phase.

	$A_1$	$A_2$	$A_3$	$\tau_1$ , ns	$\tau_2$ , ns	$\tau_3$ , ns
$\beta$	0.55	0.335	0.115	-13.5	-23.0	-98.5
$\alpha$	0.57	0.26	0.17	-12.75	-43.0	-650.0

### 8.2.2.1 Uncalibrated proton timing

The time profile of the scintillation photon emission when particles deposit energy in the scintillator is modelled in RAT by the sum of three exponentials, as

$$f(t) = \sum_{i=1}^3 A_i \frac{e^{-\frac{t}{\tau_i}} - e^{-\frac{t}{\tau_{\text{rise}}}}}{\tau_i - \tau_{\text{rise}}}, \quad (8.1)$$

where  $\tau_{\text{rise}}$  is the common rise time of the scintillator. There are the decay constants,  $\tau$ , and normalisation constants,  $A$ , for each exponential. Table 8.1 shows the decay and normalisation constants for both  $\alpha$ s and  $\beta$ s in the partially filled detector while Figure 8.4 shows the distributions described by Equation 8.1 when using those constants.

Figure 8.4 shows that the scintillation time for  $\alpha$  particles is slightly faster than that of the  $\beta$  particles. This was an unexpected result but agreed with what was observed in  $\alpha$  and  $\beta$  decays from the uranium and thorium chains [84].

The constants described in Table 8.1 are determined by performing external benchtop

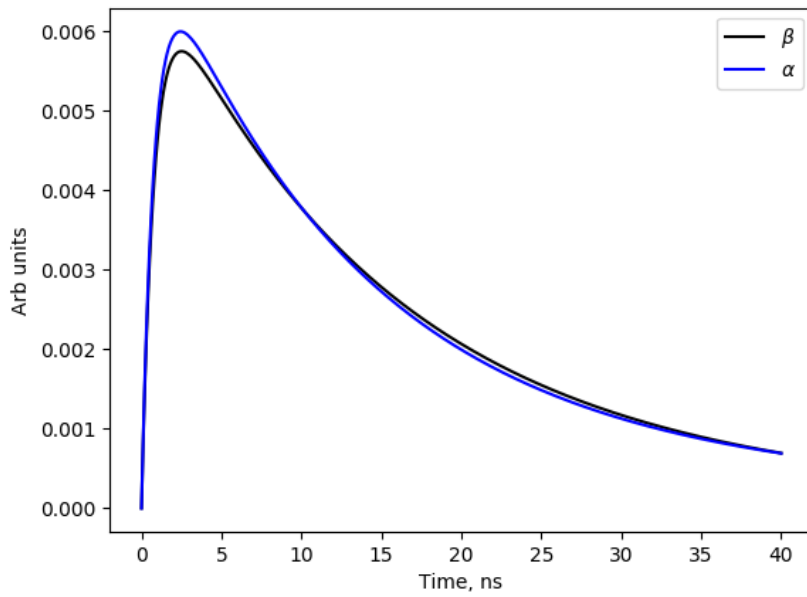


Figure 8.4: The scintillation time profiles of  $\alpha$  and  $\beta$  particles in the liquid scintillator cocktail in the partially filled detector. The scintillation time for  $\alpha$  particles is slightly faster than that of  $\beta$  particles.

measurements. Such measurements were not made for protons and therefore the same constants as those of  $\beta$ s are used to model the proton timing. In the partially filled phase the proton time constants were tuned using  $^{13}\text{C}(\alpha, n)^{16}\text{O}$  events identified in data.

### 8.2.2.2 $^{13}\text{C}(\alpha, n)^{16}\text{O}$ sample selection

A sample of events thought to be mostly consisting of  $^{13}\text{C}(\alpha, n)^{16}\text{O}$  events was identified in the partially filled open data period. The events pass all of the partial fill analysis cuts described in Chapter 6 and the reconstructed prompt energy is in the region corresponding to the proton recoil  $^{13}\text{C}(\alpha, n)^{16}\text{O}$  events. There were 13 events selected that were used to tune the proton time constants. The sample was identified during a one month period in which there was an elevated level of radon in the detector volume and thus a higher rate of  $^{210}\text{Po}$  decays. This, coupled with the low IBD expectation in a one month period, leads to the sample having high purity.

### 8.2.2.3 Calibrated proton timing

The scintillation time profile as shown in Equation 8.1 is not directly observable in data events as scintillation photons are emitted isotropically and travel different path lengths

to the PMTs that detect them. It is therefore more suitable to look at the residual hit time distribution, as described in Chapter 3. Residual hit times are PMT hit times that are corrected by the reconstructed event time and the photon time of flight from the reconstructed event position to the PMT. The corrections to the hit times make this distribution more closely match that of Equation 8.1.

The residual hit time distribution was built up for the events in the data sample and compared to MC events generated using different time constants. Figure 8.5 shows the data and MC time residual distributions when using the  $\beta$  time constants in the MC production, as historically done. The subpanel shows the ratio between the two distributions and this ratio is fit with a straight line. It can be clearly seen that the MC does not match the data, particularly in the tail of the distribution. A straight line with 0 gradient would be indicative of matching data and MC. The gradient of the ratio line can be used as a measure of how well the distributions match. The gradients are reported later in the chapter in Table 8.4.

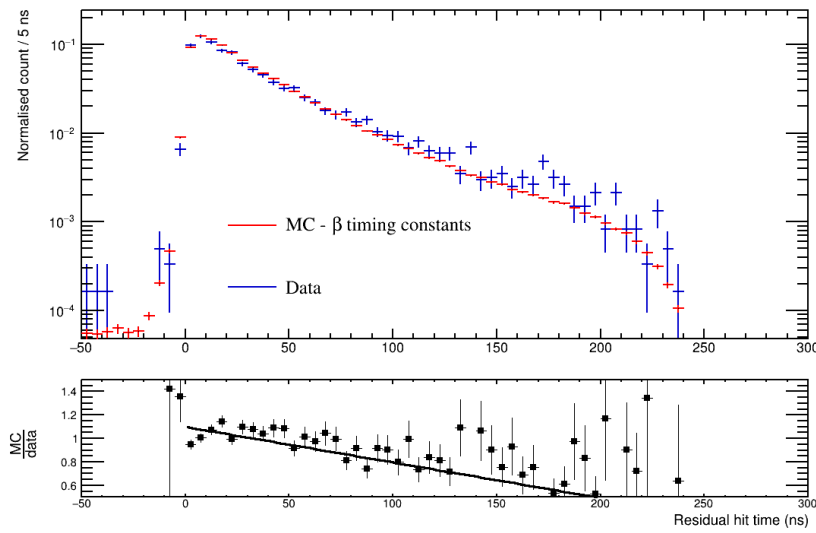


Figure 8.5: The time residual profiles of  $^{13}\text{C}(\alpha, n)^{16}\text{O}$  data and MC events in the partially filled detector. The MC is produced using the  $\beta$  time constants from Table 8.1. The fit results are reported in Table 8.4.

As a first approximation change, the data was compared to MC events generated with the  $\alpha$  time constants, as shown in Figure 8.6. The two distributions match much more closely when using these time constants and it was decided that this swap from  $\beta$  to  $\alpha$  time constants was sufficient for the partially filled phase. The gradient of the ratio line is closer to 0 than that of Figure 8.5, indicating that the change of constants is suitable.

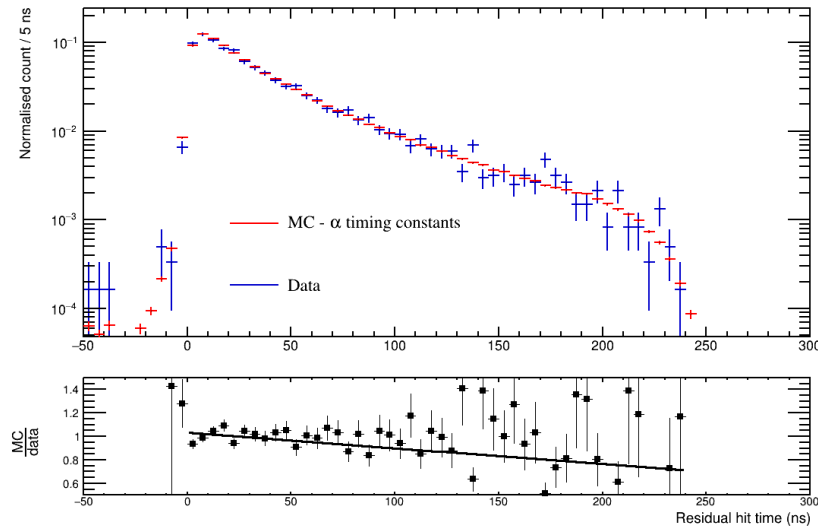


Figure 8.6: The time residual profiles of  $^{13}\text{C}(\alpha, n)^{16}\text{O}$  data and MC events in the partially filled detector. The MC is produced using the  $\alpha$  time constants from Table 8.1. The fit results are reported in Table 8.4.

Figures 8.5 and 8.6 show the full time residual distributions but it is also important to look closely at the peak of the distributions. Figure 8.7 shows the peak of the distributions for data and both MC productions. It is shown that the change from  $\beta$  to  $\alpha$  time constants certainly does not negatively impact the distribution in this region. The statistically limited nature of tuning this distribution with 13 events is amplified here and also motivates the decision to not tune the timing constants any further.

#### 8.2.2.4 Verification with the $^{241}\text{Am}^9\text{Be}$ source

Prompt low energy  $^{13}\text{C}(\alpha, n)^{16}\text{O}$  interactions are not the only events that are driven by recoiling protons. The  $^{241}\text{Am}^9\text{Be}$  calibration source is primarily used for energy calibration by virtue of the 4.4 MeV  $\gamma$  that is emitted, along with the capture of the neutron that is also emitted. However, the  $\gamma$  is only produced approximately 60% of the time and therefore coincident events can arise where the neutron causes protons to recoil as it travels through the scintillator.

##### 8.2.2.4.1 $^{241}\text{Am}^9\text{Be}$ deployment and event selection

The  $^{241}\text{Am}^9\text{Be}$  calibration source was designed for deployment in water and therefore the source was deployed in the external water outside of the AV during the partially filled phase. The source was at a position that was approximately 46 cm away from the AV

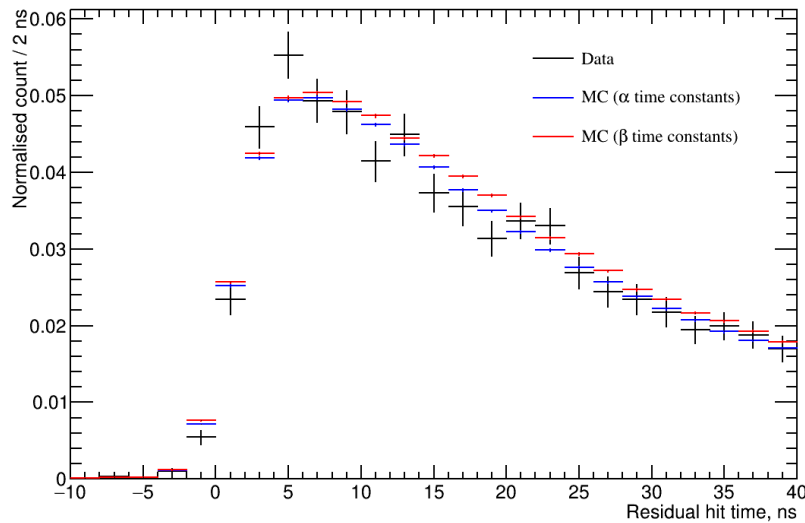


Figure 8.7: The peak of the time residual profiles of  $^{13}\text{C}(\alpha, n)^{16}\text{O}$  data and MC events in the partially filled detector. The MC is produced using the  $\alpha$  and  $\beta$  time constants from Table 8.1

surface and 1 m above the equator in the vertical axis, approximately 25 cm above the water-scintillator interface in the vertical axis. The data taking period while the source was deployed was 5.4 hours. With the source outside of the AV the number of neutrons travelling into the scintillator is significantly reduced. Additionally, the interactions typically occur very close to the AV which is an optically challenging region, it is for these two reasons why this data is not used to tune the timing constants and instead used for verification purposes.

Figure 8.8 shows the  $N_{\text{hits}}$  distribution for the  $^{241}\text{Am}^9\text{Be}$  events. Visible near 650  $N_{\text{hits}}$  is the 2.2 MeV  $\gamma$  from the neutron captures, while the peak around 1200  $N_{\text{hits}}$  is due to the 4.4 MeV  $\gamma$ s emitted from the source. A selection criterion was formed to identify coincident events where the prompt event is caused by recoiling protons, outlined in Table 8.2. The prompt  $N_{\text{hits}}$  cut was defined such that the tail of the 4.4 MeV  $\gamma$  events is avoided.

#### 8.2.2.4.2 Time residual distributions

The time residual distributions for  $^{241}\text{Am}^9\text{Be}$  prompt events is compared to distributions generated from MC events, as described in Section 8.2.2.3. Figure 8.9 shows the time residual distributions for MC events generated using both  $\alpha$  and  $\beta$  time constants compared with the data. It is immediately obvious that the change in timing constants leads

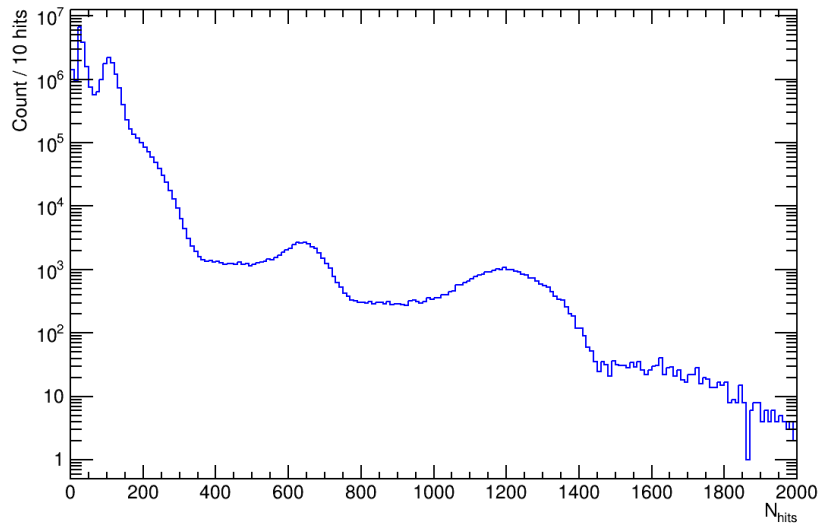
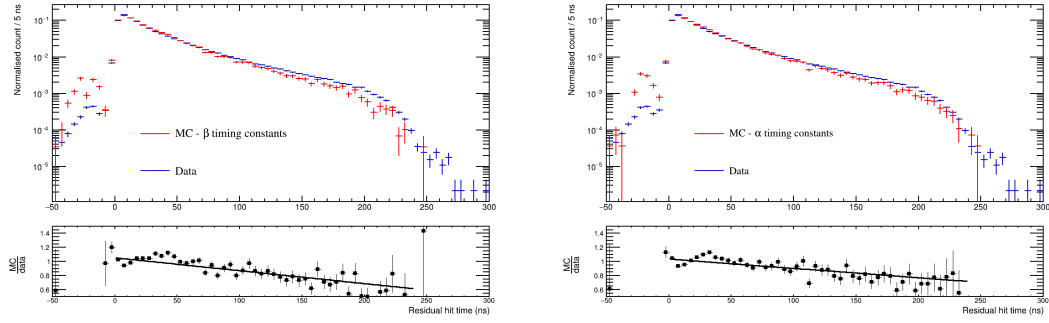


Figure 8.8: The  $N_{\text{hits}}$  distribution of events during the  $^{241}\text{Am}^9\text{Be}$  source deployment. The peak at approximately  $650 N_{\text{hits}}$  is due to the 2.2 MeV  $\gamma$ s from neutron capture on free protons. The peak at approximately  $1200 N_{\text{hits}}$  are the 4.4 MeV  $\gamma$ s emitted from the source.

to a smaller difference than is seen with the  $^{13}\text{C}(\alpha, n)^{16}\text{O}$  event sample. This is attributed to the events occurring close to the AV surface where the optical modelling of the detector becomes more difficult. The MC distribution generated with the  $\alpha$  time constants does match the data marginally better than the distribution generated with the  $\beta$  constants, therefore the tuning is acceptable.

Table 8.2: The analysis cuts used to select  $^{241}\text{Am}^9\text{Be}$  candidate event pairs in data and MC. The prompt  $N_{\text{hits}}$  cut ensures that only events driven by recoiling protons are selected

Cut	Prompt event	Delayed event
Valid position reconstruction	True	True
$N_{\text{hits}}$	$135 < N_{\text{hits}} < 900$	$500 < N_{\text{hits}} < 750$
$\Delta R$ (m)		$< 1.5$
$\Delta T$		$400\text{ns} < \Delta T < 1.1 \text{ ms}$



(a) MC generated with  $\beta$  time constants. The (b) MC generated with  $\alpha$  time constants. The fitted gradient of the ratio is  $-1.83 \pm 0.13 \times 10^{-3}$ . fitted gradient of the ratio is  $-1.32 \pm 0.14 \times 10^{-3}$ .

Figure 8.9: The time residual profiles of  $^{241}\text{Am}^9\text{Be}$  data and MC events in the partially filled detector. The change in time constants does not lead to such a significant change in the distributions. This is a consequence of the events being close to the AV surface which is an optically challenging region.

### 8.3 Discrimination of IBD and $^{13}\text{C}(\alpha, n)^{16}\text{O}$ events

With the proton time profile tuned to better match what is observed in data it is possible to use this information to discriminate between IBD events and  $^{13}\text{C}(\alpha, n)^{16}\text{O}$  events. The residual time distributions are used as inputs for a likelihood ratio test that can be performed using the time residuals of a given prompt event. For a given PDF,  $P$ , the likelihood,  $\mathcal{L}$ , is calculated as

$$\mathcal{L} = \sum_{i=1}^N P(x_i), \quad (8.2)$$

where  $x$  is the observable parameter. In the case of this analysis, the observable parameter is the residual hit time. Practically, the residual hit time is calculated for each PMT hit in an event and Equation 8.2 is evaluated.

The event discrimination is done by performing a likelihood ratio test, as

$$\Delta \log(\mathcal{L}) = \log \left( \frac{\mathcal{L}_{\text{hypothesis}}}{\mathcal{L}_{\text{alternative hypothesis}}} \right), \quad (8.3)$$

where, in this case, the two hypotheses are that the event is an IBD interaction or a  $^{13}\text{C}(\alpha, n)^{16}\text{O}$  interaction.

### 8.3.1 Partially filled phase

The PDFs used in the partially filled phase are shown in Figure 8.10. It can be seen that the time residual distribution for  $^{13}\text{C}(\alpha, n)^{16}\text{O}$  events is broader than that of IBD events at the peak of the distribution. Additionally the tail of the distribution is more significant for the  $^{13}\text{C}(\alpha, n)^{16}\text{O}$  events. This is somewhat contradictory to what would be expected with the scintillation time constants described in Table 8.1. The broader distribution can be explained by considering the number of protons scattered and the time over which they are scattered, as described in Section 8.2.1. Multiple protons are scattered over a longer timescale than that of the  $\gamma$  energy deposition in the IBD events.

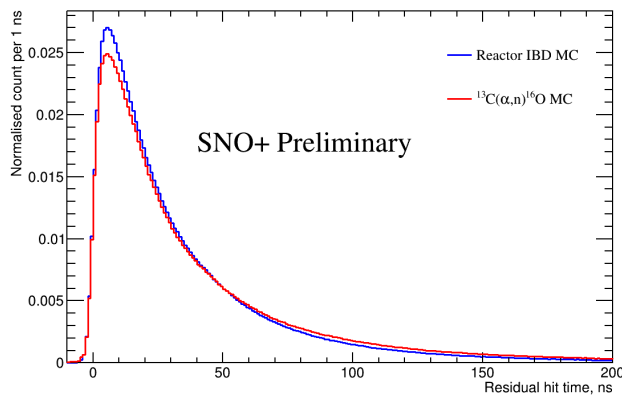


Figure 8.10: The IBD and  $^{13}\text{C}(\alpha, n)^{16}\text{O}$  time residual PDFs used in the partially filled phase. The broader peak and more significant tail for the  $^{13}\text{C}(\alpha, n)^{16}\text{O}$  distribution is attributed to the multiple proton scatters.

The event discrimination technique is performed on MC generated events to quantify the performance. Figure 8.11 shows the likelihood ratio values for IBD and  $^{13}\text{C}(\alpha, n)^{16}\text{O}$  events that pass the analysis cuts described in Chapter 6. The events are well separated using this technique with some overlap. It is therefore possible to apply a selection cut based on this classification result to remove a large fraction of  $^{13}\text{C}(\alpha, n)^{16}\text{O}$  events. The method to optimise such a cut will be described in Section 8.4.1.1.

### 8.3.2 Scintillator phase

The same exercise can be performed for MC events generated in the fully filled detector geometry. As the SNO+ scintillator phase is ongoing it has not yet been possible to tune the proton timing constants. Therefore the proton timing constants are taken to be the same as that of  $\alpha$  particles, as was the case in the partially filled phase. The

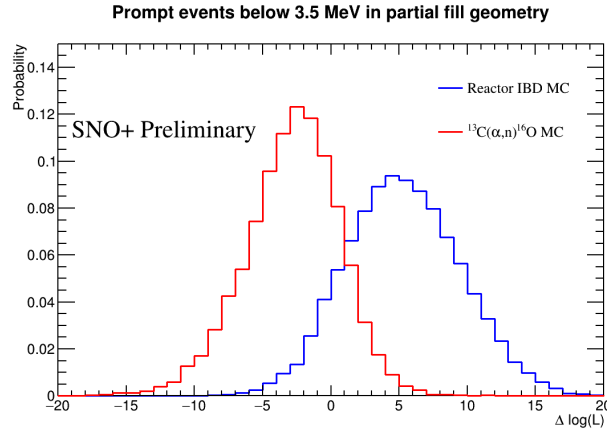


Figure 8.11: The likelihood ratio for IBD and  $^{13}\text{C}(\alpha, n)^{16}\text{O}$  MC events in the partially filled phase. The events are well separated with some overlap.

same tuning process as described in Section 8.2.2.3 is planned to be performed in the full scintillator phase. Figure 8.12 shows the time residual PDFs for the full scintillator phase. The scintillation time is faster in the full scintillator phase due to the increased PPO concentration. This increased concentration leads to an enhanced PPO to LAB non-radiative transfer efficiency which reduces the scintillation time [57]. Therefore the multiple proton scatters that constitute the  $^{13}\text{C}(\alpha, n)^{16}\text{O}$  events become more significant as the photons from the individual scattering sites are less smeared in time.

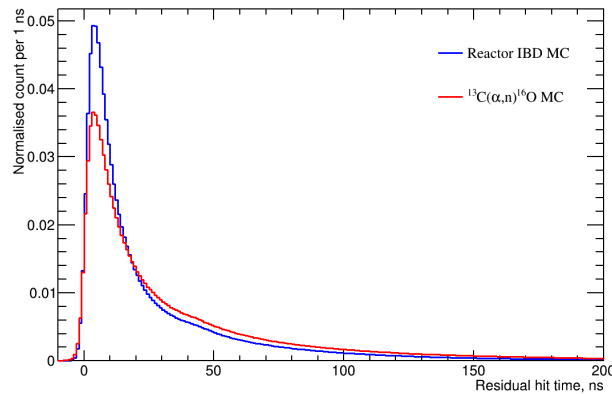


Figure 8.12: The IBD and  $^{13}\text{C}(\alpha, n)^{16}\text{O}$  time residual PDFs used in the full scintillator phase. The broader peak and more significant tail for the  $^{13}\text{C}(\alpha, n)^{16}\text{O}$  distribution is attributed to the multiple proton scatters becoming more prominent due to the faster scintillation time.

As for the partial fill, the event discrimination is performed on MC generated events. Figure 8.13 shows that the events are much more separated in the full scintillator geometry.

This is attributed to the faster scintillation time profiles, caused by an increased PPO concentration, and a better optical model due to the lack of the water-scintillator interface.

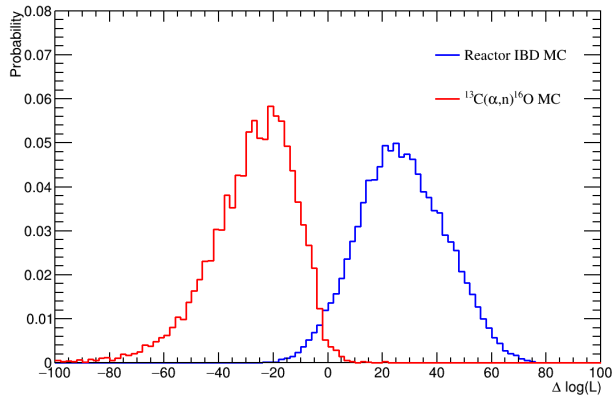


Figure 8.13: The likelihood ratio for IBD and  $^{13}\text{C}(\alpha, n)^{16}\text{O}$  MC events in the full scintillator phase. The events are significantly more separated here when compared to the partially filled phase.

## 8.4 Impact on reactor sensitivity

The technique described to discriminate between IBD and  $^{13}\text{C}(\alpha, n)^{16}\text{O}$  events is ultimately designed to improve the sensitivity of the reactor antineutrino oscillation analysis. The likelihood ratio is calculated on an event by event basis and a threshold is defined for which any events with a likelihood ratio below this threshold are removed from the analysis. The impact of applying this event classification on the sensitivity to  $\Delta m_{21}^2$  can be quantified in the full scintillator phase. Additionally, the event classification can be verified using the IBD candidates identified in the partially filled phase.

### 8.4.1 Partial fill

The partially filled phase provided a small sample of IBD candidate events (45) for which the performance of the event classification could be investigated. It was seen in Section 7.2 that the small number of candidate events also severely limited the expected performance of the oscillation analysis, however a qualitative evaluation of the performance of the event classification can be undertaken. This involves the optimisation of a cut on the likelihood ratio for the event sample and the consideration of the systematic uncertainty associated with the event classification.

### 8.4.1.1 Classifier cut optimisation

The likelihood ratio for IBD and  $^{13}\text{C}(\alpha, n)^{16}\text{O}$  events has considerable overlap in the partially filled phase, as shown in Figure 8.11. Therefore any cut on this quantity will reduce the  $^{13}\text{C}(\alpha, n)^{16}\text{O}$  background at the expense of losing a fraction of the signal events. The optimal cut value is determined by performing the oscillation analysis, as described in Section 7.2, on Asimov datasets generated with a range of cut values. The cut value that minimises the uncertainty on the best fit value of  $\Delta m_{21}^2$  is taken as the optimal cut value.

As described in Section 7.2, the small number of expected IBD candidate events means that a central value of  $\Delta m_{21}^2$  with  $1\sigma$  uncertainties is not reached when considering Asimov datasets. Therefore the cut value was optimised by measuring a central value with 30% confidence limits, with a verification performed with 40% and 50% limits. Figure 8.14 shows the resulting optimisation curves for the partially filled phase, where the uncertainty is minimum subtracted. It can be seen that the optimal cut value when considering the 30% confidence limits lies between -1 and 2. When looking at larger confidence limits the optimal cut value is restricted to the range between 0 and 0.5.

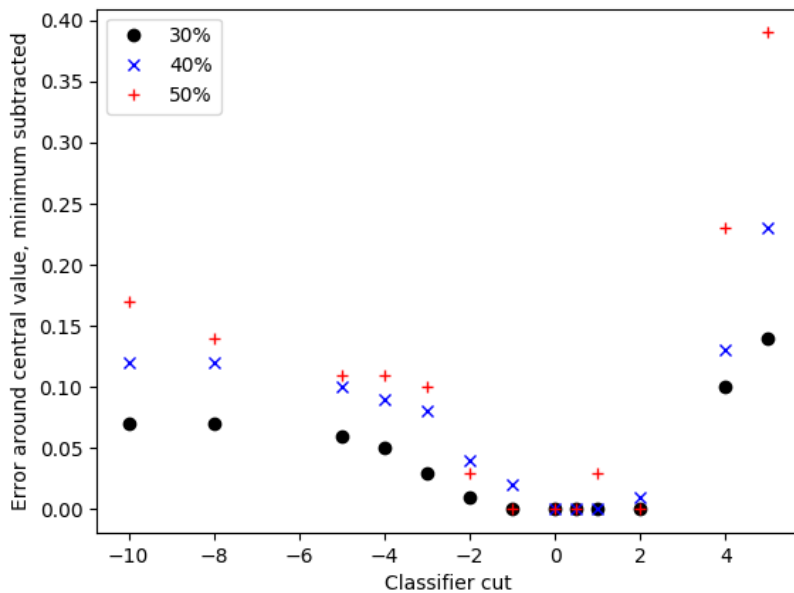


Figure 8.14: The classifier cut optimisation curves in the partially filled phase. The uncertainty around the central value is minimum subtracted. When considering all three confidence limits, the allowed range for the optimised cut is 0 to 0.5. This result was obtained assuming the oscillation parameters as quoted by the PDG.

The relative expected event counts of the signal and background are what determines the optimal classification cut value. For this reason, the optimisation process is performed again while varying the  $^{13}\text{C}(\alpha, n)^{16}\text{O}$  event rate. As described in Section 7.2.2, the uncertainty on the cross section and branching ratios for the  $^{13}\text{C}(\alpha, n)^{16}\text{O}$  interaction is large and a 30% uncertainty on the event rate is assigned to the ground state interactions and a 100% uncertainty assigned to the excited state interactions. Asimov datasets are generated assuming  $^{13}\text{C}(\alpha, n)^{16}\text{O}$  rates at the upper and lower extremes of this uncertainty and the optimisation routine is performed. Figure 8.15 shows that the optimised cut value is consistent with 0 for both the low and high  $^{13}\text{C}(\alpha, n)^{16}\text{O}$  rates. When the results in Figures 8.14 and 8.15 are considered together the optimal cut value in the partial fill phase is 0. At this value, 69.46% of  $^{13}\text{C}(\alpha, n)^{16}\text{O}$  events are removed with a 6.60% reactor IBD sacrifice.

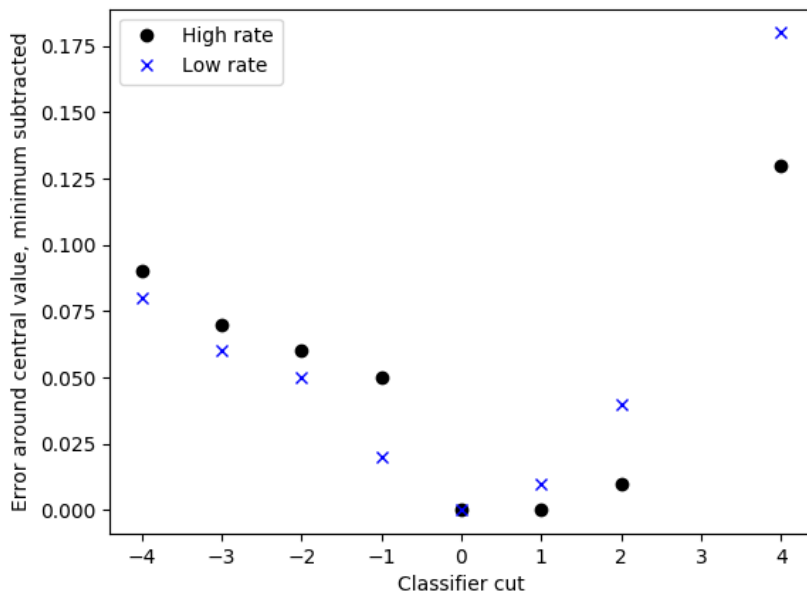


Figure 8.15: The classifier cut optimisation curves in the partially filled phase for different  $^{13}\text{C}(\alpha, n)^{16}\text{O}$  rates, corresponding to the upper and lower extremes of the systematic uncertainties. The confidence limit shown is 40% and there is a consistent minimum at 0.

#### 8.4.1.2 Classifier cut systematic uncertainty calculation

The use of the likelihood ratio value as an analysis level cut to reject events will alter the predicted number of reactor IBD, geoneutrino IBD and  $^{13}\text{C}(\alpha, n)^{16}\text{O}$  interactions. Naturally this introduces another source of uncertainty into the analysis and such a systematic

uncertainty must be accounted for and quantified. A systematic uncertainty is introduced by the classifier due to the unknown proton timing constants and potential mismodelling of the proton scintillation time. The classification may reject a significantly different fraction of events if the PDFs used in the likelihood routine are not representative of the real distributions. This effect can be estimated by generating MC events assuming different proton time constants and comparing the fraction of events cut when using the same PDFs in the likelihood method.

The optimised classifier cut of 0 was applied to two sets of reactor IBD and  $^{13}\text{C}(\alpha, n)^{16}\text{O}$  MC events. The proton timing constants differed in each set and the same constants as those of  $\alpha$ s and  $\beta$ s were used, as per Table 8.1. The PDFs used to calculate the likelihood ratio were those generated assuming the  $\alpha$  time constants for protons. The  $^{13}\text{C}(\alpha, n)^{16}\text{O}$  rejection and IBD sacrifice are summarised in Table 8.3. The IBD sacrifice changes minimally as protons have almost no contribution to the prompt event in an IBD interaction. The  $^{13}\text{C}(\alpha, n)^{16}\text{O}$  rejection has a significant change as the recoiling protons make a large contribution to the prompt events.

Table 8.3: The impact of applying the classifier to MC events that have been produced with different scintillator time constants for protons. The IBD sacrifice does not change significantly as protons contribute very little to the prompt IBD events. The difference in the  $^{13}\text{C}(\alpha, n)^{16}\text{O}$  rejection is large as these prompt events are dominated by recoiling protons.

Proton timing / PDF	$^{13}\text{C}(\alpha, n)^{16}\text{O}$ rejection, %	IBD sacrifice %
$\alpha / \alpha$	69.46	6.60
$\beta / \alpha$	27.15	6.48

With the variation of the  $^{13}\text{C}(\alpha, n)^{16}\text{O}$  rejection known for different proton timing constants the systematic uncertainty can be quantified if the level at which the proton timing is mismodelled can be estimated. The tuning of the proton time constants that was described in Section 8.2.2.3 offers a method for this by considering the straight line fits performed to the ratios in Figures 8.5 and 8.6. The difference in the gradients of the lines that are fit to the two ratios can be expressed in terms of the difference in  $^{13}\text{C}(\alpha, n)^{16}\text{O}$  rejection as per Table 8.3.

The gradient of the straight line that is fit to the ratio of the data and MC is indicative of how well the proton time constants are calibrated as a gradient of 0 would be expected

for a perfect calibration. Therefore the gradient of the line associated with the  $\alpha$  time constants can be used as a measure of the distance from a perfect calibration. The gradient of the two straight line fits to the data/MC ratios are displayed in Table 8.4. By taking the difference in  $^{13}\text{C}(\alpha, n)^{16}\text{O}$  rejection from Table 8.3 along with the difference in gradients from Table 8.4 the uncertainty in the  $^{13}\text{C}(\alpha, n)^{16}\text{O}$  rejection can be expressed as  $\pm 17.1 \pm 7.7\%$ . The former value is the direct result of the calculation while the latter value is obtained by propagating the error on the fitted gradient. Therefore the uncertainty can be reduced in two ways; a dedicated proton timing calibration will improve the agreement between the data and MC, while obtaining more  $^{13}\text{C}(\alpha, n)^{16}\text{O}$  data to increase the statistics in the ratio plots will reduce the uncertainty in the fitted gradients.

Table 8.4: The gradients of the straight line fits to the ratio of the data and MC distributions in Figures 8.5 and 8.6. The difference in the gradients is used in the calculation of the systematic uncertainty introduced by the event classification.

Proton timing constants	Gradient of straight line fit to ratio
$\beta$	$-2.5 \pm 0.2 \times 10^{-3}$
$\alpha$	$-0.7 \pm 0.3 \times 10^{-3}$

The same method can be applied to calculate the systematic uncertainty introduced to the reactor IBD prediction. Table 8.3 shows that the changing the scintillation time constants for protons has only a very small effect on the IBD sacrifice. This is to be expected as those prompt events are driven by the positron and annihilation  $\gamma$ s. The additional systematic uncertainty for the reactor IBD prediction is  $\pm 0.05 \pm 0.02\%$ . This value is negligible when compared to those uncertainties discussed in Section 7.2.2.

#### 8.4.1.3 Result

The impact of the optimised classifier cut can be evaluated for the MC dataset and the likelihood distributions verified with the IBD candidate sample. The primary objective for developing and implementing this event classification technique is to improve the sensitivity of SNO+ to  $\Delta m_{21}^2$ . The improvement can be estimated using a MC generated dataset. The small sample of 45 IBD candidates can also be used, but it is noted that a sample of this size is not expected to provide statistically significant results. However, this sample can be used to verify that the likelihood curves for both IBD and  $^{13}\text{C}(\alpha, n)^{16}\text{O}$  generated from MC are consistent with data.

Table 8.5 outlines the predicted event count in the partially filled phase before and after the application of the analysis cut on the prompt event likelihood ratio. The predicted number of events after using the event classification technique is representative of the  $^{13}\text{C}(\alpha, n)^{16}\text{O}$  rejection and IBD sacrifice reported in Table 8.3.

Table 8.5: The expected number of events in the partial fill phase, split by interaction type, after event classification.

Signal	Events (no event classification)	Events (with event classification)
Reactor IBD	$9.4 \pm 0.3$	$8.8 \pm 0.3$
Geoneutrino IBD	$2.2 \pm 2.2$	$2.1 \pm 2.1$
$^{13}\text{C}(\alpha, n)^{16}\text{O}$	$33.3 \pm 12.5$	$10.2 \pm 6.4$

#### 8.4.1.3.1 Asimov MC data

The first way to evaluate the impact of the prompt event classification routine is by using MC generated events. These events were used when determining the optimal cut value described in Section 8.4.1.1. The oscillation fit routine is performed on an Asimov data set that is generated assuming the PDG neutrino oscillation parameters and the likelihood phase space generated. The cut on the event classifier output is applied to this data set.

Figure 8.16 shows the oscillation fit likelihood phase space for  $\Delta m_{21}^2$  and  $\theta_{12}$  with the event classification applied. This can be directly compared to Figure 7.3. It can be seen that the region corresponding to 25% confidence limits grows smaller when the event classification is used. Additionally there is the emergence of a  $2\sigma$  exclusion contour indicating a generally better fit result.

Figure 8.17 shows the 1D slice of the oscillation fit when  $\theta_{12}$  is taken to be equal to the global best fit value quoted by the PDG. The distribution is compared to that of the fit to the full data sample. There is improvement across the whole phase space when the prompt event classification is included. The correct minimum is found ( $\Delta m_{21}^2 = 7.53 \times 10^{-5}\text{eV}^2$ ), giving confidence that the use of the prompt event classifier does not bias the oscillation fit. The trough corresponding to the minimum is narrower when the event classification is used leading to the conclusion that its use will positively impact the fit result.

#### 8.4.1.3.2 IBD candidate events

The event classification routine is applied to the IBD candidates with a prompt energy below 3.5 MeV identified in the partially filled phase. Firstly, the predicted number of

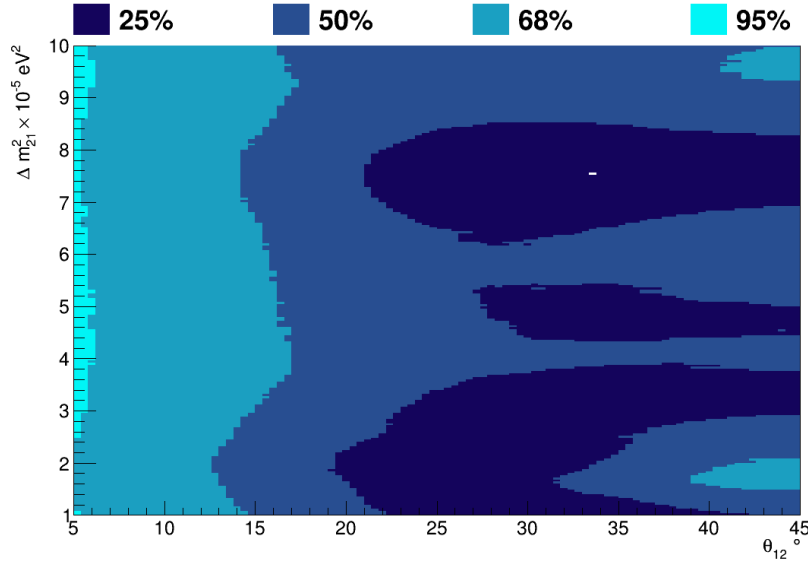


Figure 8.16: The likelihood space for  $\Delta m_{21}^2$  and  $\theta_{12}$  after using the prompt event classifier for an Asimov MC data set. There is a larger region that is excluded at 25% confidence and a  $2\sigma$  exclusion contours has appeared when compared to the result shown in Figure 7.3. The best fit is  $\Delta m_{21}^2 = 7.54 \times 10^{-5} \text{ eV}^2$ ,  $\theta_{12} = 33.6^\circ$ .

events can be compared with the observation in data, before and after using the cut on the event classifier. It has already been described in Section 7.2 that 45 IBD candidate events were selected in data without event classification. The predicted number of events in Table 8.5, without event classification, is  $44.9 \pm 12.7$  events. Therefore the prediction agrees very well with the data and is a good baseline for evaluating the performance of the event classification.

The predicted event count after the application of the event classification is  $21.1 \pm 6.7$ . Applying the optimised cut value of 0 to the IBD candidates leaves 20 events remaining. Once again the prediction agrees very well with what is observed in data and is a good indicator that the event classification technique is valid. Figure 8.18 shows the data and MC prompt energy distributions before and after applying the classifier cut. The MC curve is the sum of the reactor IBD, geoneutrino IBD and  $^{13}\text{C}(\alpha, n)^{16}\text{O}$  spectra and is normalised such that the integral is equal to the predicted event count. There is good agreement, particularly across the low energy bins where the event classification is applied.

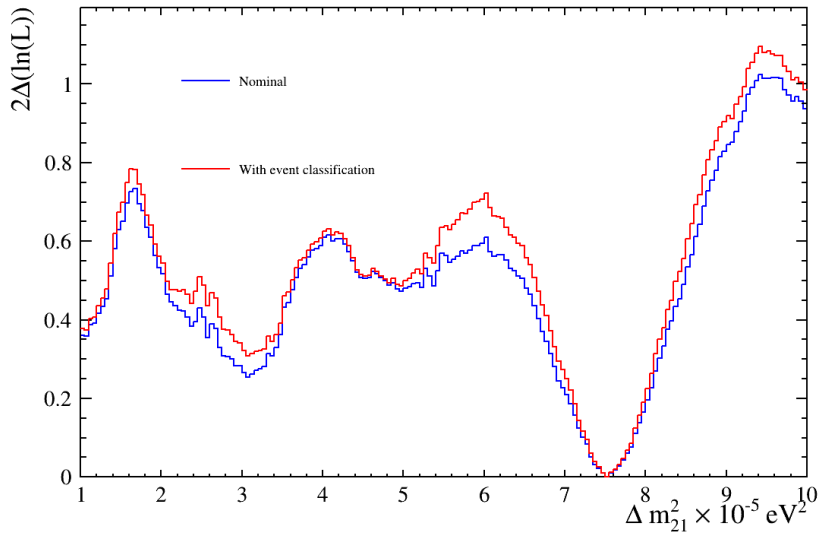


Figure 8.17: The likelihood space for  $\Delta m_{21}^2$  after using the prompt event classifier for an Asimov MC data set. This 1D slice is obtained by taking  $\theta_{12}$  to be the value as quoted by the PDG. It can be seen that there is improvement across the whole phase space when including the event classification and the trough corresponding to the minimum is narrower.

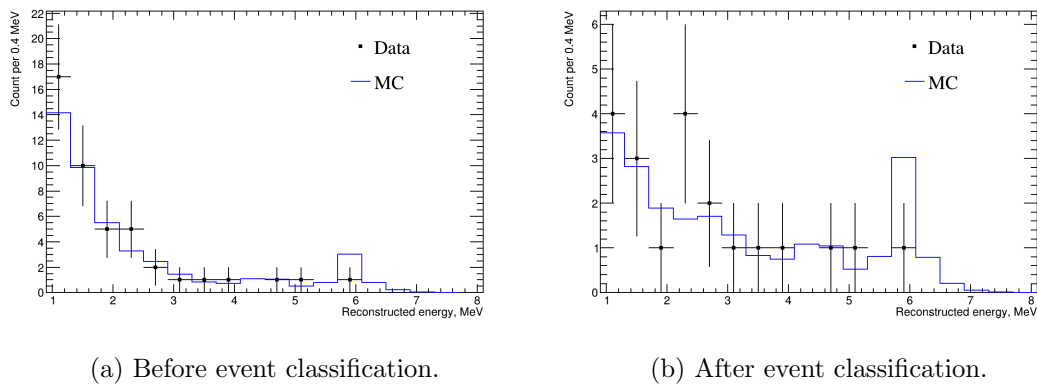


Figure 8.18: The prompt energy spectra in the partially filled phase for data and MC before and after application of the event classification. The MC is the sum of the reactor IBD, geoneutrino IBD and  $^{13}\text{C}(\alpha, n)^{16}\text{O}$  spectra. The MC is normalised such that the integral is equal to the predicted number of events.

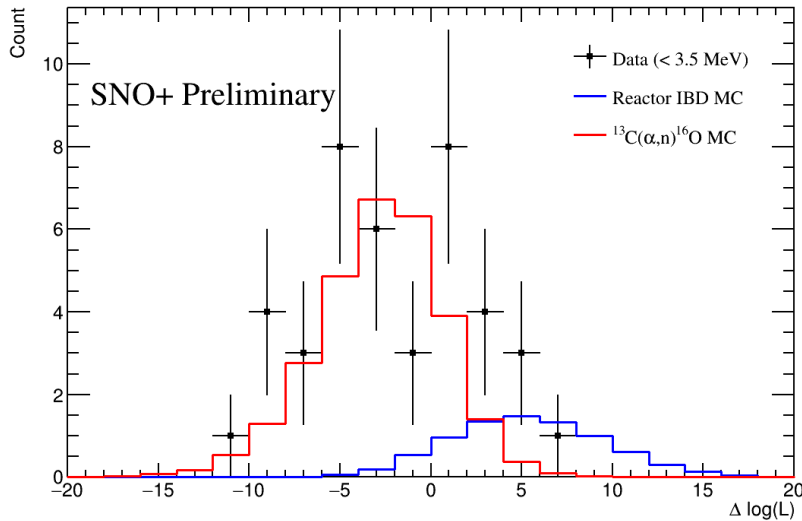


Figure 8.19: The likelihood ratio distributions in data and MC. The MC is scaled such that the integrals of the distributions are equal to the predicted number of events. The data events are only those with a prompt energy  $< 3.5$  MeV.

The IBD candidate event sample that was identified in the partially filled phase can be used to verify that the likelihood curves generated from MC events accurately reflect what is observed in data, for prompt events below 3.5 MeV. Figure 8.19 shows the likelihood curves as predicted in Figure 8.11 scaled such that the integral of the curves is equal to the predicted event count. There is generally good agreement across the likelihood ratio space, although it is noted that more data will need to be collected to better understand the distributions.

Finally, the oscillation fit analysis can be performed on the data events that remain after the application of the prompt event classification. Figure 8.20 shows the 2D likelihood space for  $\Delta m_{21}^2$ . The likelihood has been expressed to show the 25%, 50%,  $1\sigma$  and  $2\sigma$  confidence intervals. There are a number of interesting features when compared to that of the fit performed without the event classification as in Figure 7.6. Firstly there is a smaller region of the likelihood space that is present within 25% confidence of the minimum value, with two islands now visible. Secondly, the  $1\sigma$  and  $2\sigma$  contours have grown larger, indicating that there is generally better fit performance.

Figure 8.21 shows the likelihood distribution for  $\Delta m_{21}^2$  when taking  $\theta_{12}$  to be equal to the global best fit value of  $33.6^\circ$ . The distribution for the data after the event classification shows the appearance of a second minimum with a much smaller  $\Delta m_{21}^2$ . This region was not excluded at  $1\sigma$  confidence in the full data sample and as such the second minima is

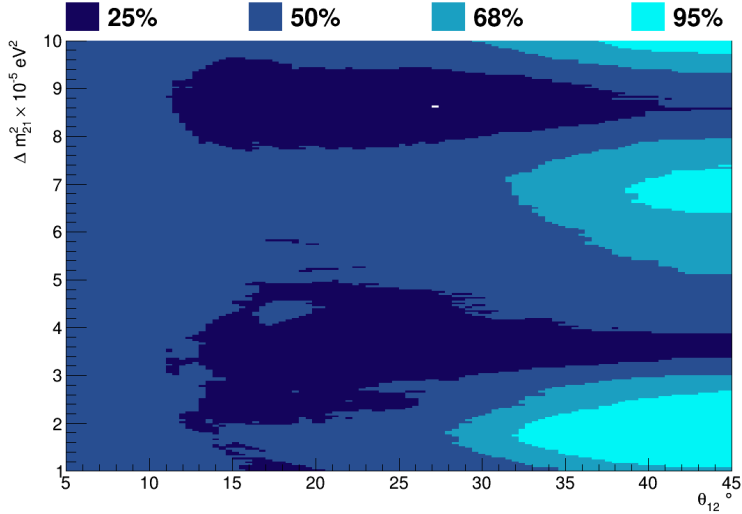


Figure 8.20: The likelihood space for  $\Delta m_{21}^2$  and  $\theta_{12}$  after using the prompt event classifier. There is a larger region that is excluded at 25% confidence and the  $1\sigma$  and  $2\sigma$  exclusion contours are also larger. The best fit is  $\Delta m_{21}^2 = 8.62 \times 10^{-5} \text{ eV}^2$ ,  $\theta_{12} = 27.2^\circ$ .

not inconsistent with the original fit result. Finally, there are now some regions of the phase space that are excluded with  $2\sigma$  confidence, highlighting improvement after using the prompt event classifier.

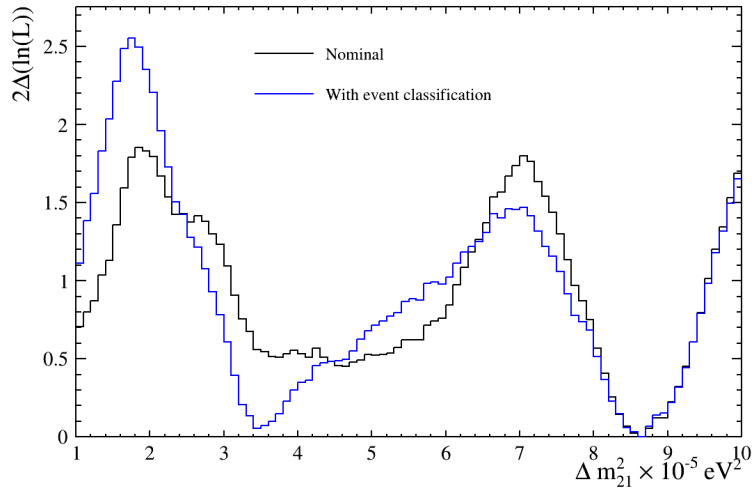


Figure 8.21: The likelihood space for  $\Delta m_{21}^2$  after using the prompt event classifier. This 1D slice is obtained by taking  $\theta_{12}$  to be the value as quoted by the PDG. It can be seen that there is now a region of phase space that is excluded at  $2\sigma$  confidence. There is the emergence of a second minima in the distribution but this is consistent with the fit to the full data set.

### 8.4.2 Future sensitivity for SNO+

The results discussed in Section 8.4.1.3 show that including an analysis cut on the prompt event classification in the event selection improves the sensitivity to  $\Delta m_{21}^2$ . All results shown thus far have focused on the partially filled phase of the experiment. With data taking in the full scintillator phase underway, the predicted sensitivity over time was also evaluated. A new blindness scheme to be applied to data collected in the full scintillator phase is proposed in Appendix D.

The sensitivity over time is estimated by performing the oscillation analysis on Asimov data sets corresponding to different data collection livetimes. The resulting  $1\sigma$  uncertainties on the best fit values are fit as a function of livetime $^{-\frac{1}{2}}$  to obtain the sensitivity curve. This process is carried out for three different cases: the nominal event prediction, the event prediction assuming a reduction in the  $^{13}\text{C}(\alpha, n)^{16}\text{O}$  rate by a factor of ten and the nominal event prediction after event classification.

For the case in which the event classification routine is used the analysis cut value must be reoptimised for each data set that is fit. The reason behind this concerns the increased reactor IBD signal events observed with increasing livetime. With larger statistics it becomes detrimental to the oscillation fit if too much of the signal is sacrificed. This is illustrated in Figure 8.22, where the optimised cut value becomes more negative with increasing livetime. Referring back to Figure 8.13, this indicates that the cut is less aggressive for rejecting  $^{13}\text{C}(\alpha, n)^{16}\text{O}$  events and sacrificing IBD events. This is attributed to the location of the troughs in the prompt energy spectrum. Only one of these troughs is in the same region as the low energy  $^{13}\text{C}(\alpha, n)^{16}\text{O}$  events and therefore as more events are collected a better fit can be made to the trough at higher energy. Consequentially the background suppression in the low energy region is less impactful and a smaller reduction in the number of signal events is advantageous.

Figure 8.23 shows the sensitivity curves for the three cases outlined, using the optimised classifier cuts for the event classification curve. The horizontal line corresponds to the  $1\sigma$  uncertainties on the measurement reported by KamLAND [36], the current world leading fit. This limit is reached with 3.2 years of livetime assuming a constant rate of  $^{13}\text{C}(\alpha, n)^{16}\text{O}$  events and no event classification. If event classification is included this limit is reached with less data required; 2.6 years. This corresponds to the limit being reached with seven fewer months of livetime. As a reference, the limit is reached in 2.4 years if the  $^{13}\text{C}(\alpha, n)^{16}\text{O}$  rate is reduced by a factor of 10, indicating that the event classification routine is performing as expected given the reduction in background that it achieves.

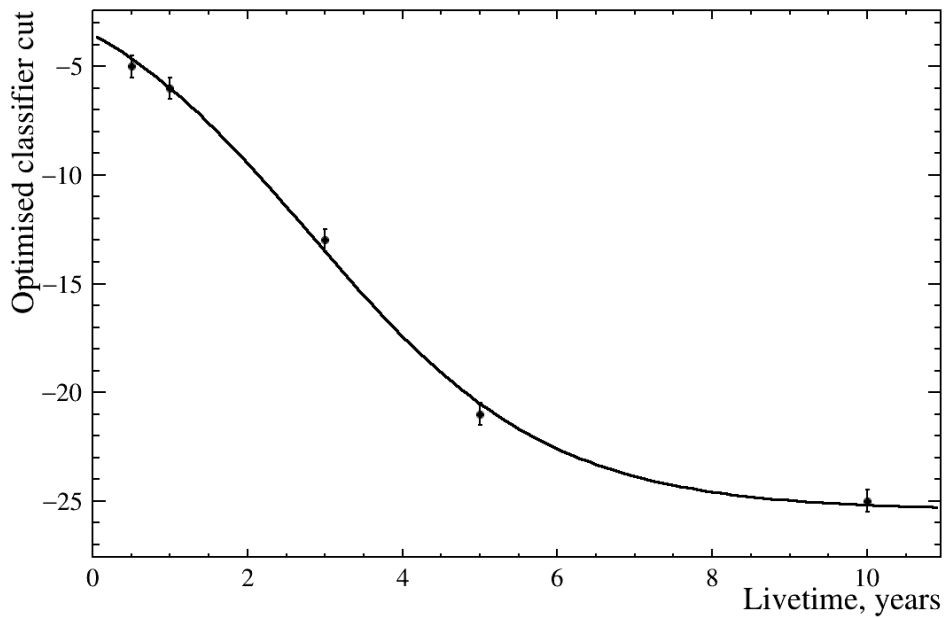


Figure 8.22: The optimised classifier cut value as a function of data taking livetime. The cut value is optimised for 0.5, 1, 3, 5 and 10 years livetime and these points are fit with a sigmoid function. As more data is collected it is more favourable to have a smaller signal sacrifice.

The results shown in Figure 8.23 are validated by repeating the analysis for MC data generated using an alternative value of  $\Delta m_{21}^2$ . The sensitivity curves for the same three outlined cases, using the SNO/Super-Kamiokande joint fit result of  $\Delta m_{21}^2 = 4.84 \times 10^{-5} \text{ eV}^2$ , are shown in Figure 8.24. The uncertainties reported by SNO/Super-Kamiokande are not symmetrical and the lower uncertainty is chosen for evaluation in this analysis. Figure 8.24 shows comparable performance of the event classification routine when compared to Figure 8.23. It is found that the SNO/Super-Kamiokande limit is surpassed after 1.1 years assuming a constant rate of  $^{13}\text{C}(\alpha, n)^{16}\text{O}$  events and no event classification. This is reduced to 0.6 years with the inclusion of the event classification technique. The agreement of the results for MC events generated with two different values of  $\Delta m_{21}^2$  gives more confidence to the validity of the analysis presented.

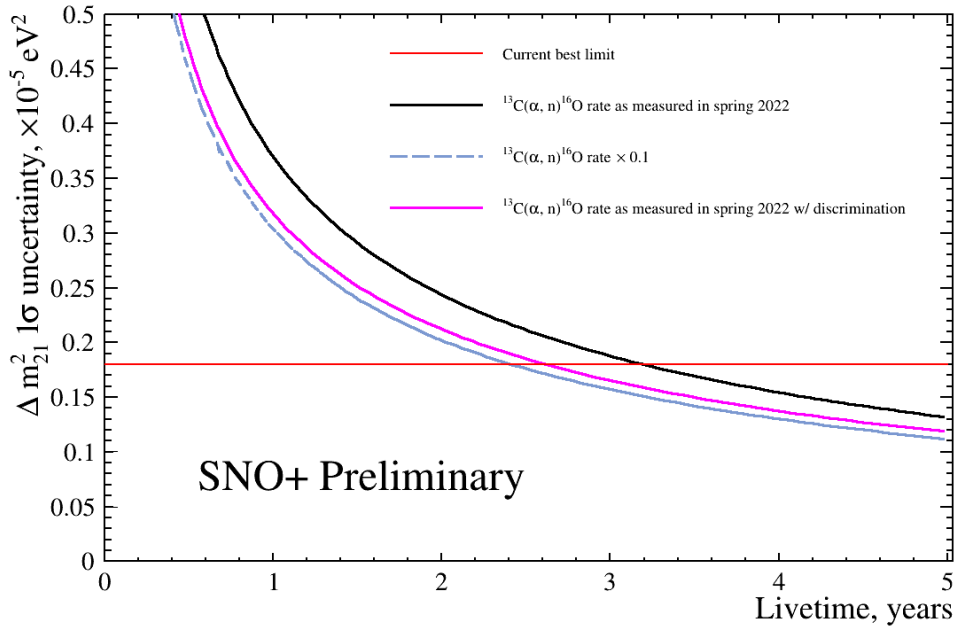


Figure 8.23: The sensitivity of SNO+ to  $\Delta m_{21}^2$  as a function of livetime in the scintillator phase. The MC data is generated assuming  $\Delta m_{21}^2 = 7.54 \times 10^{-5} \text{ eV}^2$  and the  $^{13}\text{C}(\alpha, n)^{16}\text{O}$  rate is assumed to be constant.

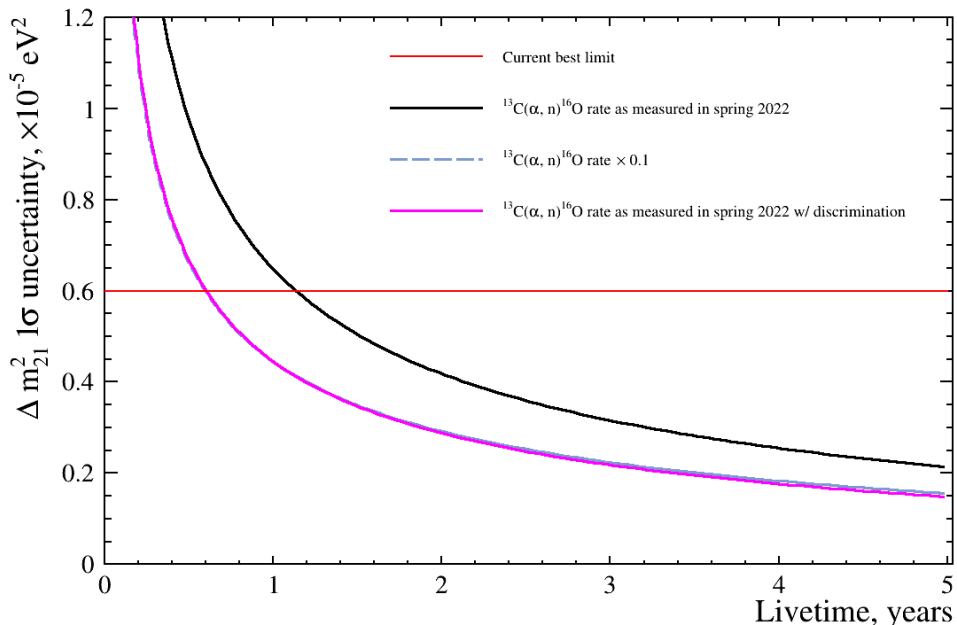


Figure 8.24: The sensitivity of SNO+ to  $\Delta m_{21}^2$  as a function of livetime in the scintillator phase. The MC data is generated assuming  $\Delta m_{21}^2 = 4.84 \times 10^{-5} \text{ eV}^2$  and the  $^{13}\text{C}(\alpha, n)^{16}\text{O}$  rate is assumed to be constant.

## 8.5 Conclusion

In Chapter 7 the  $^{13}\text{C}(\alpha, n)^{16}\text{O}$  rate was shown to significantly impact the oscillation fit result. A technique to suppress this background based on a difference in the scintillation time profiles of  $e^+e^-$  annihilation and recoiling protons is outlined in this chapter. A likelihood ratio test can be performed on IBD candidate events and there is a clear distinction between IBD and low energy  $^{13}\text{C}(\alpha, n)^{16}\text{O}$  events. A chosen fraction of  $^{13}\text{C}(\alpha, n)^{16}\text{O}$  events can then be removed from the data set, improving the signal to background ratio.

Using this technique to remove a fraction of  $^{13}\text{C}(\alpha, n)^{16}\text{O}$  events from the data set was shown to improve the result of the oscillation analysis across the whole phase space and thus improve the sensitivity of the analysis. The technique was applied to a small sample of IBD candidate events identified during the partially filled phase of SNO+ and a small improvement in the fit was observed. Finally, an improved projection of the sensitivity to  $\Delta m_{21}^2$  as SNO+ collects more data was produced and the current best measurement of this parameter is reached with seven fewer months of data collection using the described technique.

# Chapter 9

## Conclusion

The proximity of the SNO+ experiment to various commercial reactor complexes on the North American continent means that it is well placed to detect reactor antineutrinos. The flux of antineutrinos at SNO+ is sufficient to perform a measurement of the neutrino oscillation parameter  $\Delta m_{21}^2$ . Certainly this is one of the prime physics objectives of SNO+ prior to the search for  $0\nu\beta\beta$  in the tellurium loaded scintillator phase.

This thesis introduced the SNO+ detector and the aspects that make it suitable as a reactor antineutrino detector. The importance of optical calibration for analyses was discussed in detail. The recent improvements in analysis techniques using the AMELLIE calibration source, part of the light injection system, were outlined. It was shown that the MC simulation of AMELLIE has been changed such that it better matches what is seen in data. Additionally a proof of concept study was completed to show that AMELLIE can be used to monitor changes in the optical attenuation in the liquid scintillator.

The detection of reactor antineutrinos at SNO+ was then formally introduced, giving context to importance of the analysis in the wider scope of neutrino physics. An overview of the prediction and simulation of the main reactor antineutrino signal was given from emission in the reactor core to detection in SNO+. The same treatment was applied to the significant backgrounds in this analysis, the  $^{13}\text{C}(\alpha, n)^{16}\text{O}$  and geoneutrino IBD interactions. The practical steps for selecting such events from SNO+ data were described.

Finally, a likelihood analysis to extract  $\Delta m_{21}^2$  from the prompt energy spectrum of IBD candidate events was outlined. The flux contribution from nearby nuclear reactors are fit such that the oscillation parameters that produce the best prompt energy spectrum to match the data are extracted. This fitting routine was applied to MC generated data and a small sample of IBD candidate events identified in the SNO+ partially filled phase. The size of the sample was insufficient to produce a central value with  $1\sigma$  errors but the

oscillation analysis was verified to produce a result consistent with expectation.

A technique to identify  $^{13}\text{C}(\alpha, n)^{16}\text{O}$  interactions in the data sample was introduced. This required an in-situ calibration of the scintillation time profile of protons. This calibration was performed using real  $^{13}\text{C}(\alpha, n)^{16}\text{O}$  events and verified with neutrons produced by the  $^{241}\text{Am}^9\text{Be}$  calibration source. A time based likelihood ratio test was developed to distinguish between  $^{13}\text{C}(\alpha, n)^{16}\text{O}$  and IBD events with good performance. In the partially filled phase, 69.46% of  $^{13}\text{C}(\alpha, n)^{16}\text{O}$  events could be removed from the data set with a 6.60% IBD sacrifice. A systematic uncertainty of 18.75% is associated with this event classification. The small sample of IBD candidate events were fit after employing this background suppression and an improved likelihood space was observed.

The impact of the background suppression was evaluated for future data taking periods. It was found that without event classification SNO+ would surpass the current world leading measurement of  $\Delta m_{21}^2$  after 3.2 years of livetime. When the event classification technique is included the same measurement is surpassed after 2.6 years of livetime. The sensitivity of SNO+ to  $\Delta m_{21}^2$  is greatly improved by incorporating event classification.

# Bibliography

- [1] The SNO Collaboration, “Measurement of the Rate of  $\nu_e + d \rightarrow p + p + e^-$  Interactions Produced by  ${}^8B$  Solar Neutrinos at the Sudbury Neutrino Observatory,” *Physical Review Letters*, vol. 87, Jul 2001. 1, 4
- [2] The Super-Kamiokande Collaboration, “Evidence for Oscillation of Atmospheric Neutrinos,” *Physical Review Letters*, vol. 81, pp. 1562–1567, aug 1998. 1, 4
- [3] The DUNE Collaboration, “Long-Baseline Neutrino Facility (LBNF) and Deep Underground Neutrino Experiment (DUNE) Conceptual Design Report Volume 1: The LBNF and DUNE Projects,” 2016. 1, 23
- [4] Hyper-Kamiokande Proto-Collaboration, “Hyper-Kamiokande Design Report,” 2018. 1, 23
- [5] The KamLAND Collaboration, “First Results from KamLAND: Evidence for Reactor Antineutrino Disappearance,” *Physical Review Letters*, vol. 90, jan 2003. 1, 66, 67
- [6] W. Pauli, “Pauli letter collection, letter to Lise Meitner.” CERN Archives. Bldg. 61-S-001 - Safe 3, 1930. <https://cds.cern.ch/record/83282>. 3
- [7] J. Chadwick, “The existence of a neutron,” *Proceedings of the Royal Society of London. Series A, Containing Papers of a Mathematical and Physical Character*, vol. 136, no. 830, pp. 692–708, 1932. 3
- [8] E. Fermi, “Versuch einer Theorie der  $\beta$ -Strahlen. I,” *Zeitschrift für Physik*, vol. 88, pp. 161–177, Mar 1934. 3
- [9] H. R. Crane and J. Halpern, “New Experimental Evidence for the Existence of a Neutrino,” *Phys. Rev.*, vol. 53, pp. 789–794, May 1938. 3

- [10] C. L. Cowan, F. Reines, F. B. Harrison, H. W. Kruse, and A. D. McGuire, “Detection of the Free Neutrino: a Confirmation,” *Science*, vol. 124, no. 3212, pp. 103–104, 1956.  
3
- [11] C. N. Yang and R. L. Mills, “Conservation of Isotopic Spin and Isotopic Gauge Invariance,” *Phys. Rev.*, vol. 96, pp. 191–195, Oct 1954. 3
- [12] C. S. Wu, E. Ambler, R. W. Hayward, D. D. Hoppes, and R. P. Hudson, “Experimental Test of Parity Conservation in Beta Decay,” *Phys. Rev.*, vol. 105, pp. 1413–1415, Feb 1957. 3
- [13] S. L. Glashow, “Partial-symmetries of weak interactions,” *Nuclear Physics*, vol. 22, no. 4, pp. 579–588, 1961. 4
- [14] P. W. Higgs, “Broken Symmetries and the Masses of Gauge Bosons,” *Phys. Rev. Lett.*, vol. 13, pp. 508–509, Oct 1964. 4, 18
- [15] S. Weinberg, “A Model of Leptons,” *Phys. Rev. Lett.*, vol. 19, pp. 1264–1266, Nov 1967. 4
- [16] A. Salam and J. C. Ward, “Weak and electromagnetic interactions,” *Il Nuovo Cimento (1955-1965)*, vol. 11, pp. 568–577, Feb 1959. 4
- [17] G. Danby, J.-M. Gaillard, K. Goulian, L. M. Lederman, N. Mistry, M. Schwartz, and J. Steinberger, “Observation of High-Energy Neutrino Reactions and the Existence of Two Kinds of Neutrinos,” *Phys. Rev. Lett.*, vol. 9, pp. 36–44, Jul 1962.  
4
- [18] The DONUT Collaboration, “Observation of tau neutrino interactions,” *Physics Letters B*, vol. 504, pp. 218–224, apr 2001. 4
- [19] M. Goldhaber, L. Grodzins, and A. W. Sunyar, “Helicity of Neutrinos,” *Phys. Rev.*, vol. 109, pp. 1015–1017, Feb 1958. 4
- [20] R. Davis, D. S. Harmer, and K. C. Hoffman, “Search for Neutrinos from the Sun,” *Phys. Rev. Lett.*, vol. 20, pp. 1205–1209, May 1968. 4
- [21] C. Giunti and C. W. Kim, *Fundamentals of Neutrino Physics and Astrophysics*. 2007. 5, 19
- [22] K. Zuber, *Neutrino Physics*. 2021. 5

- [23] B. Kayser, “On the quantum mechanics of neutrino oscillation,” *Phys. Rev. D*, vol. 24, pp. 110–116, Jul 1981. 5
- [24] B. Pontecorvo, “Inverse beta processes and nonconservation of lepton charge,” *Zh. Eksp. Teor. Fiz.*, vol. 34, p. 247, 1957. 5
- [25] Z. Maki, M. Nakagawa, and S. Sakata, “Remarks on the Unified Model of Elementary Particles,” *Progress of Theoretical Physics*, vol. 28, pp. 870–880, 11 1962. 5
- [26] The KATRIN Collaboration, “Direct neutrino-mass measurement with sub-electronvolt sensitivity,” *Nature Physics*, vol. 18, pp. 160–166, Feb 2022. 7
- [27] B. Kayser, “CPT, CP, and  $C$  phases, and their effects, in Majorana-particle processes,” *Phys. Rev. D*, vol. 30, pp. 1023–1033, Sep 1984. 7
- [28] The SNO+ Collaboration, “The SNO+ experiment,” *Journal of Instrumentation*, vol. 16, p. P08059, Aug 2021. 7, 26, 29, 30, 40, 41
- [29] KamLAND-Zen Collaboration, “First Search for the Majorana Nature of Neutrinos in the Inverted Mass Ordering Region with KamLAND-Zen,” 2022. 7, 21, 22
- [30] The CUORE Collaboration, “Search for Majorana neutrinos exploiting millikelvin cryogenics with CUORE,” *Nature*, vol. 604, pp. 53–58, Apr 2022. 7, 21
- [31] C. Giunti, “No effect of Majorana phases in neutrino oscillations,” *Physics Letters B*, vol. 686, pp. 41–43, mar 2010. 7
- [32] L. Wolfenstein, “Neutrino oscillations in matter,” *Phys. Rev. D*, vol. 17, pp. 2369–2374, May 1978. 9
- [33] S. P. Mikheyev and A. Y. Smirnov, “Resonance Amplification of Oscillations in Matter and Spectroscopy of Solar Neutrinos,” *Sov. J. Nucl. Phys.*, vol. 42, pp. 913–917, 1985. 9
- [34] S. P. Mikheyev and A. Y. Smirnov, “Resonant amplification of  $\nu$  oscillations in matter and solar-neutrino spectroscopy,” *Il Nuovo Cimento C*, vol. 9, pp. 17–26, Jan 1986. 9
- [35] D. Anderson, *Theory of the Earth*. Blackwell Scientific Publications, 1989. 11
- [36] M. Decowski, “KamLAND’s precision neutrino oscillation measurements,” *Nuclear Physics B*, vol. 908, pp. 52–61, 2016. Neutrino Oscillations: Celebrating the Nobel Prize in Physics 2015. 12, 15, 56, 75, 115

- [37] P. Zyla *et al.*, “Review of Particle Physics,” *PTEP*, vol. 2020, no. 8, p. 083C01, 2020.  
and 2021 update. 13, 73
- [38] The Daya Bay Collaboration, “Measurement of the Electron Antineutrino Oscillation with 1958 Days of Operation at Daya Bay,” *Physical Review Letters*, vol. 121, dec 2018. 15
- [39] Y. Nakano, “Recent Solar neutrino Results from Super-Kamiokande,” *Journal of Physics: Conference Series*, vol. 1342, p. 012037, jan 2020. 17, 56
- [40] T. Kajita, “Atmospheric Neutrinos,” *Advances in High Energy Physics*, vol. 2012, p. 504715, Nov 2012. 17
- [41] The Super-Kamiokande Collaboration, “Atmospheric neutrino oscillation analysis with external constraints in Super-Kamiokande I-IV,” *Phys. Rev. D*, vol. 97, p. 072001, Apr 2018. 17
- [42] P. Adamson *et al.*, “The NuMI neutrino beam,” *Nuclear Instruments and Methods in Physics Research Section A: Accelerators, Spectrometers, Detectors and Associated Equipment*, vol. 806, pp. 279–306, jan 2016. 17
- [43] The T2K Collaboration, “Constraint on the matter–antimatter symmetry-violating phase in neutrino oscillations,” *Nature*, vol. 580, pp. 339–344, Apr 2020. 18
- [44] M. Gell-Mann, P. Ramond, and R. Slansky, “Complex Spinors and Unified Theories,” 2013. 19
- [45] M. Goeppert-Mayer, “Double Beta-Disintegration,” *Phys. Rev.*, vol. 48, pp. 512–516, Sep 1935. 20
- [46] A. S. Barabash, “Experiment double beta decay: Historical review of 75 years of research,” *Physics of Atomic Nuclei*, vol. 74, pp. 603–613, apr 2011. 20
- [47] W. H. Furry, “On Transition Probabilities in Double Beta-Disintegration,” *Phys. Rev.*, vol. 56, pp. 1184–1193, Dec 1939. 20
- [48] F. T. Avignone, S. R. Elliott, and J. Engel, “Double beta decay, Majorana neutrinos, and neutrino mass,” *Rev. Mod. Phys.*, vol. 80, pp. 481–516, Apr 2008. 21, 22
- [49] S. D. Biller, “Combined constraints on Majorana masses from neutrinoless double beta decay experiments,” *Phys. Rev. D*, vol. 104, p. 012002, Jul 2021. 21

- [50] F. D. Lodovico, “The Hyper-Kamiokande Experiment,” *Journal of Physics: Conference Series*, vol. 888, p. 012020, sep 2017. 23
- [51] R. Nakamura, H. Sambonsugi, K. Shiraishi, and Y. Wada, “Research and development toward KamLAND2-Zen,” *Journal of Physics: Conference Series*, vol. 1468, p. 012256, feb 2020. 23
- [52] The SNO+ Collaboration, “Current Status and Future Prospects of the SNO+ Experiment,” *Advances in High Energy Physics*, vol. 2016, p. 6194250, Jan 2016. 23
- [53] The LEGEND Collaboration, “The large enriched germanium experiment for neutrinoless double beta decay (LEGEND),” in *AIP Conference Proceedings*, Author(s), 2017. 23
- [54] M. Agostini, G. Benato, and J. A. Detwiler, “Discovery probability of next-generation neutrinoless double-beta decay experiments,” *Physical Review D*, vol. 96, sep 2017. 23
- [55] The JUNO Collaboration, “JUNO physics and detector,” *Progress in Particle and Nuclear Physics*, vol. 123, p. 103927, mar 2022. 24
- [56] The SNO Collaboration, “The Sudbury Neutrino Observatory,” *Nuclear Instruments and Methods in Physics Research Section A: Accelerators, Spectrometers, Detectors and Associated Equipment*, vol. 449, p. 172207, Jul 2000. 25, 29
- [57] The SNO+ Collaboration, “Development, characterisation, and deployment of the SNO+ liquid scintillator,” *Journal of Instrumentation*, vol. 16, p. P05009, May 2021. 26, 60, 74, 104
- [58] V. I. Tretyak and Y. G. Zdesenko, “TABLES OF DOUBLE BETA DECAY DATA AN UPDATE,” *Atomic Data and Nuclear Data Tables*, vol. 80, no. 1, pp. 83–116, 2002. 26
- [59] The SNO+ Collaboration, “Measurement of the  ${}^8\text{B}$  solar neutrino flux in SNO+ with very low backgrounds,” *Physical Review D*, vol. 99, Jan 2019. 27
- [60] The SNO+ Collaboration, “Improved search for invisible modes of nucleon decay in water with the SNO+ detector,” *Physical Review D*, vol. 105, Jun 2022. 27
- [61] The SNO+ Collaboration, “Optical calibration of the SNO+ detector in the water phase with deployed sources,” *Journal of Instrumentation*, vol. 16, p. P10021, Oct 2021. 27

- [62] The SNO+ Collaboration, “Measurement of neutron-proton capture in the SNO+ water phase,” *Physical Review C*, vol. 102, Jul 2020. 27, 40
- [63] The Borexino Collaboration, “Measurement of the solar  $^8\text{B}$  neutrino rate with a liquid scintillator target and 3 MeV energy threshold in the Borexino detector,” *Phys. Rev. D*, vol. 82, p. 033006, Aug 2010. 27
- [64] The KamLAND Collaboration, “Measurement of the  $^8\text{B}$  solar neutrino flux with the KamLAND liquid scintillator detector,” *Phys. Rev. C*, vol. 84, p. 035804, Sep 2011. 27
- [65] R. N. Mohapatra and A. Pérez-Lorenzana, “Neutrino mass, proton decay, and dark matter in TeV scale universal extra dimension models,” *Phys. Rev. D*, vol. 67, p. 075015, Apr 2003. 27
- [66] J. Paton, “Event-by-event direction reconstruction in a liquid scintillator detector.” Publication in preparation. 28
- [67] The Borexino Collaboration, “Final results of Borexino Phase-I on low-energy solar neutrino spectroscopy,” *Physical Review D*, vol. 89, Jun 2014. 29
- [68] R. Bonventre, *Neutron Multiplicity in Atmospheric Neutrino Events at the Sudbury Neutrino Observatory*. PhD thesis, University of Pennsylvania, <https://repository.upenn.edu/edissertations/1213>, 2014. 30
- [69] C. Jackson, “Photographs of aged concentrators.” SNO+ DocDB **3518**, 2016. Accessed May 2022. 30
- [70] S. Biller, N. Jelley, M. Thorman, N. Fox, and T. Ward, “Measurements of photomultiplier single photon counting efficiency for the Sudbury Neutrino Observatory,” *Nuclear Instruments and Methods in Physics Research Section A: Accelerators, Spectrometers, Detectors and Associated Equipment*, vol. 432, no. 2, pp. 364–373, 1999. 31
- [71] S. Seibert and others, “RAT.” <https://rat.readthedocs.io/en/latest/index.html>, 2022. Accessed May 2022. 34
- [72] S. Agostinelli *et al.*, “Geant4a simulation toolkit,” *Nuclear Instruments and Methods in Physics Research Section A: Accelerators, Spectrometers, Detectors and Associated Equipment*, vol. 506, no. 3, pp. 250–303, 2003. 34

- [73] G. Horton-Smith, “GLG4sim page.” <https://www.phys.ksu.edu/personal/gahs/GLG4sim/>, 2007. Accessed Jan 2022. 34
- [74] R. Brun and F. Rademakers, “ROOT An object oriented data analysis framework,” *Nuclear Instruments and Methods in Physics Research Section A: Accelerators, Spectrometers, Detectors and Associated Equipment*, vol. 389, no. 1, pp. 81–86, 1997. New Computing Techniques in Physics Research V. 34
- [75] I. T. Coulter, *Modelling and reconstruction of events in SNO+ related to future searches for lepton and baryon number violation*. PhD thesis, Oxford University, UK, 2013. 35
- [76] M. J. D. Powell, “An efficient method for finding the minimum of a function of several variables without calculating derivatives,” *Comput. J.*, vol. 7, pp. 155–162, 1964. 35
- [77] M. Mottram, “Updated functional form energy reconstruction: EnergyRThetaFunctional.” SNO+ DocDB **3488**, 2015. Accessed Jan 2022. 36
- [78] E. Falk, J. Lidgard, M. I. Stringer, and E. Turner, “Commissioning of ELLIE for SNO+,” 2017. 40
- [79] J. Waterfield, *Optical calibration system for SNO+ and sensitivity to neutrinoless double-beta decay*. PhD thesis, University of Sussex, UK, 2017. 42
- [80] R. Alves *et al.*, “The calibration system for the photomultiplier array of the SNO+ experiment,” *Journal of Instrumentation*, vol. 10, p. P03002, Mar 2015. 45, 48
- [81] M. Nirkko, “TELLIE fibre position validation.” SNO+ DocDB **4442**, 2017. Accessed Feb 2022. 46
- [82] T. Kroupová, *Improving the Sensitivity to Neutrinoless Double Beta Decay in SNO+*. PhD thesis, University of Oxford, UK, 2020. 50
- [83] *Nuclear Power Reactors in the World*. No. 2 in Reference Data Series, Vienna: INTERNATIONAL ATOMIC ENERGY AGENCY, 2021. 57, 58, 68, 141
- [84] I. Morton-Blake, *First measurement of reactor antineutrinos in scintillator at SNO+ and study of alternative designs for large-scale liquid scintillator detectors*. PhD thesis, University of Oxford, UK, 2021. 59, 78, 79, 80, 91, 96

- [85] R. Arevalo, W. F. McDonough, and M. Luong, “The K/U ratio of the silicate Earth: Insights into mantle composition, structure and thermal evolution,” *Earth and Planetary Science Letters*, vol. 278, no. 3, pp. 361–369, 2009. 59
- [86] S. Z. L. Ludhova, “Studying the Earth with Geoneutrinos,” *Advances in High Energy Physics*, vol. 2013, no. 425693, 2013. 59
- [87] Tosaka, “Decay chain(4n+2, Uranium series).” [https://en.wikipedia.org/wiki/Decay\\_chain](https://en.wikipedia.org/wiki/Decay_chain), 2014. Accessed Apr 2022. 61
- [88] E. Bellotti, C. Broggini, G. Di Carlo, M. Laubenstein, and R. Menegazzo, “Precise measurement of the  $^{222}\text{Rn}$  half-life: A probe to monitor the stability of radioactivity,” *Physics Letters B*, vol. 743, pp. 526–530, 2015. 60
- [89] G. Audi, F. G. Kondev, M. Wang, W. Huang, and S. Naimi, “The NUBASE2016 evaluation of nuclear properties,” *Chinese Physics C*, vol. 41, p. 030001, mar 2017. 60, 61
- [90] K. J. R. Rosman and P. D. P. Taylor, “Isotopic compositions of the elements 1997 (Technical Report),” *Pure Appl Chem.*, vol. 70, pp. 217–235, 1998. 62
- [91] The Daya Bay Collaboration, “New measurement of  $\theta_{13}$  via neutron capture on hydrogen at daya bay,” *Phys. Rev. D*, vol. 93, p. 072011, Apr 2016. 63, 79
- [92] P. Huber, “Determination of antineutrino spectra from nuclear reactors,” *Phys. Rev. C*, vol. 84, p. 024617, Aug 2011. 66, 67
- [93] T. A. Mueller, D. Lhuillier, M. Fallot, A. Letourneau, S. Cormon, M. Fechner, L. Giot, T. Lasserre, J. Martino, G. Mention, A. Porta, and F. Yermia, “Improved predictions of reactor antineutrino spectra,” *Physical Review C*, vol. 83, may 2011. 66, 67
- [94] M. James, “Energy released in fission,” *Journal of Nuclear Energy*, vol. 23, no. 9, pp. 517–536, 1969. 66
- [95] M. Cribier, “Reactor monitoring with Neutrinos,” *Nuclear Physics B - Proceedings Supplements*, vol. 221, pp. 57–61, 2011. The Proceedings of the 22nd International Conference on Neutrino Physics and Astrophysics. 68
- [96] *Operating Experience with Nuclear Power Stations in Member States*. Operating Experience with Nuclear Power Stations in Member States, Vienna: INTERNATIONAL ATOMIC ENERGY AGENCY, 2021. 68

- [97] IESO, “IESO Data Directory.” <https://www.ieso.ca/en/Power-Data/Data-Directory>, 2022. Accessed Apr 2022. 68, 70
- [98] M. Matsumoto and T. Nishimura, “Mersenne Twister: A 623-Dimensionally Equidistributed Uniform Pseudo-Random Number Generator,” *ACM Trans. Model. Comput. Simul.*, vol. 8, p. 330, jan 1998. 70
- [99] J. A. Formaggio and G. P. Zeller, “From ev to eev: Neutrino cross sections across energy scales,” *Rev. Mod. Phys.*, vol. 84, pp. 1307–1341, Sep 2012. 71
- [100] K. Scholberg, “Coherent elastic neutrino-nucleus scattering,” *Journal of Physics: Conference Series*, vol. 606, p. 012010, apr 2015. 71
- [101] P. Vogel and J. F. Beacom, “Angular distribution of neutron inverse beta decay,  $\bar{\nu}_e + \vec{p} \rightarrow e^+ + n$ ,” *Phys. Rev. D*, vol. 60, p. 053003, Jul 1999. 72, 73
- [102] A. Czarnecki, W. J. Marciano, and A. Sirlin, “Radiative corrections to neutron and nuclear beta decays revisited,” *Physical Review D*, vol. 100, oct 2019. 72
- [103] D. Wilkinson, “Phase space for neutron beta-decay: an update,” *Nuclear Instruments and Methods in Physics Research Section A: Accelerators, Spectrometers, Detectors and Associated Equipment*, vol. 404, no. 2, pp. 305–310, 1998. 73
- [104] C.-Y. Seng, M. Gorchtein, and M. J. Ramsey-Musolf, “Dispersive evaluation of the inner radiative correction in neutron and nuclear  $\beta$  decay,” *Phys. Rev. D*, vol. 100, p. 013001, Jul 2019. 73
- [105] B. Märkisch, H. Mest, H. Saul, X. Wang, H. Abele, D. Dubbers, M. Klopf, A. Petoukhov, C. Roick, T. Soldner, and D. Werder, “Measurement of the Weak Axial-Vector Coupling Constant in the Decay of Free Neutrons Using a Pulsed Cold Neutron Beam,” *Phys. Rev. Lett.*, vol. 122, p. 242501, Jun 2019. 73
- [106] A. Wright, “Water Update.” SNO+ DocDB **7300**, 2022. Accessed Apr 2022. 74
- [107] T. Kaptanoglu, *Reactor Antineutrinos In The SNO+ Water Phase And Detector R&D For Large-Scale Neutrino Detectors*. PhD thesis, University of Pennsylvania, 2020. 74
- [108] E. Sanshiro, “Geoneutrino spectra.” <https://www.awa.tohoku.ac.jp/~sanshiro/research/geoneutrino/spectrum/index.html>, 2006. Acessed Apr 2022. 75

- [109] O. Šrámek, B. Roskovec, S. A. Wipperfurth, Y. Xi, and W. F. McDonough, “Revealing the Earth’s mantle from the tallest mountains using the Jinping Neutrino Experiment,” *Scientific Reports*, vol. 6, p. 33034, Sep 2016. 75
- [110] I. Semenec, “Geo-neutrinos in SNO+.” Neutrino Geoscience 2019, 2019. <https://indico.cern.ch/event/825708/contributions/3543658/>. 75
- [111] The Borexino Collaboration, “Comprehensive geoneutrino analysis with Borexino,” *Physical Review D*, vol. 101, jan 2020. 75
- [112] A. Rytz, “Energies of Natural Alpha Radiators,” in *Nuclidic Masses* (W. H. Johnson, ed.), (Vienna), pp. 221–228, Springer Vienna, 1964. 76
- [113] B. von Krosigk, *Measurement of proton and particle quenching in LAB based scintillators and determination of spectral sensitivities to supernova neutrinos in the SNO+ detector*. PhD thesis, Technische Universität Dresden, 2015. 76, 77
- [114] S. Ricetto, “Partial fill 210 Po.” SNO+ DocDB **6794**, 2021. Accessed Apr 2022. 76
- [115] V. Lozza, “Background summary.” SNO+ DocDB **7312**, 2022. Accessed Apr 2022. 76
- [116] K. J. R. Rosman and P. D. P. Taylor, “Isotopic compositions of the elements 1997 (Technical Report),” *Pure and Applied Chemistry*, vol. 70, no. 1, pp. 217–235, 1998. 76
- [117] J. F. Ziegler, “Stopping Range of Ions in Matter.” <https://www.srim.org>, 2013. Accessed Apr 2022. 76
- [118] T. Murata, H. Matsunobu, and K. Shibata, “Evaluation of the ( $\alpha$ , xn) reaction data for JENDL/AN-2005,” tech. rep., Japan, 2006. JAEA-Research-2006-052. 76, 77
- [119] K. K. Sekharan, A. S. Divatia, M. K. Mehta, S. S. Kerekatte, and K. B. Nambiar, “ $^{13}\text{C}(\alpha, n)^{16}\text{O}$  Reaction Cross Section between 1.95 and 5.57 MeV,” *Phys. Rev.*, vol. 156, pp. 1187–1190, Apr 1967. 77, 87
- [120] J. K. Bair and F. X. Haas, “Total Neutron Yield from the Reactions  $^{13}\text{C}(\alpha, n)^{16}\text{O}$  and  $^{17,18}\text{O}(\alpha, n)^{20,21}\text{Ne}$ ,” *Phys. Rev. C*, vol. 7, pp. 1356–1364, Apr 1973. 77, 87
- [121] JANIS, “JANIS web:  $\alpha$ -induced cross sections.” <https://www.oecd-nea.org/janisweb/book/alphas/C13/MT4/renderer/554>, 2022. Accessed Apr 2022. 77

- [122] J. Zhao, Z.-Y. Yu, J.-L. Liu, X.-B. Li, F.-H. Zhang, and D.-M. Xia, “ $^{13}\text{C}(\alpha,\text{n})^{16}\text{O}$  background in a liquid scintillator based neutrino experiment,” *Chin. Phys. C*, vol. 38, no. 11, p. 116201, 2014. 77
- [123] The Daya Bay Collaboration, “A side-by-side comparison of Daya Bay antineutrino detectors,” *Nuclear Instruments and Methods in Physics Research, Section A: Accelerators, Spectrometers, Detectors and Associated Equipment*, vol. 685, pp. 78–97, Sept. 2012. 77
- [124] M. Febbraro *et al.*, “New  $^{13}\text{C}(\alpha,n)^{16}\text{O}$  Cross Section with Implications for Neutrino Mixing and Geoneutrino Measurements,” *Phys. Rev. Lett.*, vol. 125, p. 062501, Aug 2020. 77, 87
- [125] B. Liggins, *Cosmic muon-induced neutrons in the SNO+ water phase*. PhD thesis, Queen Mary, University of London, 2020. 78, 137
- [126] S. Riccetto, “Detector response vs PPO loading.” SNO+ DocDB **7296**, 2022. Accessed Apr 2022. 78
- [127] S. S. Wilks, “The Large-Sample Distribution of the Likelihood Ratio for Testing Composite Hypotheses,” *The Annals of Mathematical Statistics*, vol. 9, no. 1, pp. 60 – 62, 1938. 84
- [128] The Daya Bay Collaboration, “Improved measurement of the reactor antineutrino flux and spectrum at Daya Bay,” *Chinese Physics C*, vol. 41, p. 013002, jan 2017. 87
- [129] S. Harissopoulos, H. W. Becker, J. W. Hammer, A. Lagoyannis, C. Rolfs, and F. Strieder, “Cross section of the  $^{13}\text{C}(\alpha,\text{n})^{16}\text{O}$  reaction: A background for the measurement of geo-neutrinos,” *Phys. Rev. C*, vol. 72, p. 062801, Dec 2005. 87
- [130] The KamLAND Collaboration, “Constraints on  $\theta_{13}$  from a three-flavor oscillation analysis of reactor antineutrinos at KamLAND,” *Phys. Rev. D*, vol. 83, p. 052002, Mar 2011. 88
- [131] G. Cowan, K. Cranmer, E. Gross, and O. Vitells, “Asymptotic formulae for likelihood-based tests of new physics,” *The European Physical Journal C*, vol. 71, feb 2011. 89
- [132] T. Bezerra, “IBD Selection for Partial Fill.” SNO+ DocDB **7216**, 2022. Accessed May 2022. 91

## Appendix A

### List of acronyms

- 0νββ** Neutrinoless double beta decay  
**2νββ** Two neutrino double beta decay  
**AECL** Atomic Energy of Canada LTD  
**AMELLIE** Attenuation module of ELLIE  
**AV** Acrylic vessel  
**BSM** Beyond the standard model  
**BWR** Boiling water reactor  
**CTC** Crate Trigger Card  
**DAQ** Data acquisition  
**DB** Daughterboard  
**DCR** Deck clean room  
**ELLIE** Embedded LASER/LED Light Injection Entity  
**FEC** Front End Card  
**FIFO** First-in-first-out  
**FOM** Figure of merit  
**GT** Global trigger  
**GTID** Global trigger identification number  
**HV** High voltage  
**IAEA** International Atomic Energy Agency  
**IBD** Inverse beta decay  
**IESO** Independent Energy Systems Operator  
**LAB** Linear alkylbenzene  
**LF** Load factor  
**MTC/A+** Master Trigger Card Analog

- MTC/D** Master Trigger Card Digital
- PDF** Probability density function
- PDG** Particle data group
- PHWR** Pressurised heavy water reactor
- PMT** Photomultiplier tube
- PMTIC** PMT Interface Card
- PPO** 2,5-Diphenyloxazole
- PSUP** PMT support structure
- PWR** Pressurised water reactor
- RAT** Reactor analysis tool
- SM** Standard model
- SMELLIE** Scattering module of ELLIE
- SNO** Sudbury Neutrino Observatory
- TELLIE** Timing module of ELLIE
- TUBii** Trigger Utility Board II
- UPW** Ultra-pure water

## Appendix B

# Run selection

The first step for any physics analysis to produce reliable and trustworthy results is the verification that the data used is of the highest quality. In SNO+ this verification is performed by the run selection group. The process to ensure the quality of the data is largely automated thanks to efforts of the group in recent years. This Appendix will outline the checks that each hour long sample of data (runs) are subjected to.

### B.1 Checks

The run selection criteria is formed in a modular fashion. There are nine modules that each contain their own checks. All checks must be passed for the data to be deemed good for analysis. Each individual check is composed of a parameter and a threshold. If the parameter crosses the threshold then the check is failed and the data is not used in analysis.

The nine modules are: High Level Data Quality (DQHL), Detector State, Ping Crates, Trigger Clock Jumps, Channel Flags, Muons, Run State, Deck Activity and Shifter Opinion. The Shifter Opinion module is an informational module and the result has no impact on the outcome of run selection. This is so that detector operators can notify the run selection group of anything unusual without immediately throwing away data. Three of the remaining modules are so called "purgatory" checks. These modules are: Trigger Clock Jumps, Channel Flags and Deck Activity. If any check fails in one of these modules then the run is flagged for closer inspection by a member of the run selection group.

The checks that are present in each module are outlined in the following sections.

### B.1.1 Run state

The Run State module checks that the general run settings are as expected and that the run is of sufficient length. A run that is cut short likely indicates a problem identified by the detector operator. The checks are summarised in Table B.1. In this context  $\Delta t$  is the difference in run length reported by the run control software (via the machine it is running on) and the DAQ hardware (via the detector clocks). These values can disagree considerably in the case of network instability which leads to a loss of confidence that data has been recorded correctly by the event builder software.

Table B.1: The run state checks.

Check	Threshold	Note
Minimum run length	1800 s	
$\Delta t$	3000 s	The difference in run length as calculated by run control software and DAQ database
Run type	Physics	

### B.1.2 Detector State

The Detector State module is the largest set of data quality checks. This module parses the log files generated by the SNO+ event builder and the DAQ server to check for any errors when collecting data, as shown in Table B.2.

#### B.1.2.1 Alarms

The Detector State module also checks whether there are any active alarms during the run. The alarms are posted to inform detector operators of any issues on a short timescale. If any of the alarms in Table B.3 are active during a run then the data is not used for analysis.

### B.1.3 DQHL

The High Level Data Quality module was the first set of automated data quality checks to be implemented. This module is concerned with trigger rates, event timing and PMT

coverage to ensure that there are no abnormalities in the data collection. The rate of each individual physics trigger, along with the total event rate, must be greater than 5 Hz and less than 7000 Hz. Rates that are outside of these values indicate that the triggers are not operating as expected and the data cannot be trusted. Considering the events in a run, the time of the first event in the run must be no later than 1 second after the run start time. This ensures there is not a large portion of dead time between physics runs which could be symptom of a wider problem. Additionally, all events should have an associated global trigger identification number (GTID). Finally, the timestamps associated with each event should increment chronologically. A small tolerance is given on this check to account for trigger clock jumps, as described in Section B.1.5.

This module also verifies that the PMT coverage is sufficient. This check is performed using three different metrics. Firstly, more than 70% of the total number of PMTs must be online. Secondly, all crates must be on and at high voltage (HV). Finally, each panel of the PSUP must have 80% of its PMTs online. The PSUP is an icosahedral structure and is composed of 20 faces upon which the PMTs are mounted. This check ensures that there is not a geometrical blind spot in the detector.

#### B.1.4 Ping Crates

Ping Crates is a process that runs at the start of each run. Various aspects of the trigger signals are checked to ensure that the triggers are in nominal working order. Each slot (32 channels associated with a single PMTIC/FEC) is triggered sequentially from software to emulate a PMT pulse causing the discriminator threshold to be crossed. The following properties of the trigger signals are checked: the trigger peak (in ADC counts), the width, the rise time and the fall time of the trigger signal. This process is performed for both the N100 and N20 trigger. If any of the values are outside of the predefined thresholds then the run is not used in analysis.

#### B.1.5 Trigger Clock Jumps

The Trigger Clock Jumps module counts the number of times a bit-flip occurs on either clock (10 MHz or 50 MHz), causing a large jump in the reported time of subsequent events. An example of a bit flip between three events is 114A91 → 116A92 → 114A93, whereby the bit flip was corrected for the third event. As SNO+ has two clocks and a bit flip on both clocks for the same event is extremely rare, the bit flips can be corrected. Hence the Trigger Clock Jump module is a purgatory check, as a large amount of clock jumps may

indicate an issue with the MTC.

### B.1.6 Channel Flags

The Channel Flags module identifies channels (PMTs and electronics) that are out of sync. These channels are removed from analyses and hence this module is a purgatory check. If too many channels are out of sync it may indicate a problem with the DAQ hardware, compromising the quality of the data collected.

### B.1.7 Muons

The Muon module checks that there is not an excessive amount of high  $N_{\text{hits}}$  events present in the run which could indicate an issue with PMTs or the dry end electronics. The cosmic muon rate at SNO+ is approximately three per hour [125] and are identifiable in data due to their high  $N_{\text{hits}}$  and correlated hits by PMTs looking outward into the external cavity. If more than 100 events of this type are identified during a run then it is not used in analysis.

### B.1.8 Deck activity

The Deck Activity module checks whether any person had registered being on deck or in the DCR during a run. Electronic noise and pickup can be introduced by people working near the crates and therefore runs for which this has occurred should be scrutinised more closely. A tablet is mounted outside the entrance to the deck and people are required to log their activity using the electronic form. This data is then accessed by run selection to determine if a run should be flagged for closer inspection.

## B.2 Monitoring

The automated nature of the data quality checks leads to the creation of tools to visualise the results over time. Figure B.1 show an example of run selection results for a typical week of data collection. The first plot shows the overall pass/fail statistics as a function of time, whereby the pass/fail time is integrated on the y axis. This plot is useful for showing the general state of data quality at any given time. The second plot shows only the failed runs with the modules that failed also displayed. This is used to determine exactly why runs are not passing data quality to help inform the detector maintenance group. This can help to diagnose problems with the detector, leading to faster turnaround times for maintenance.

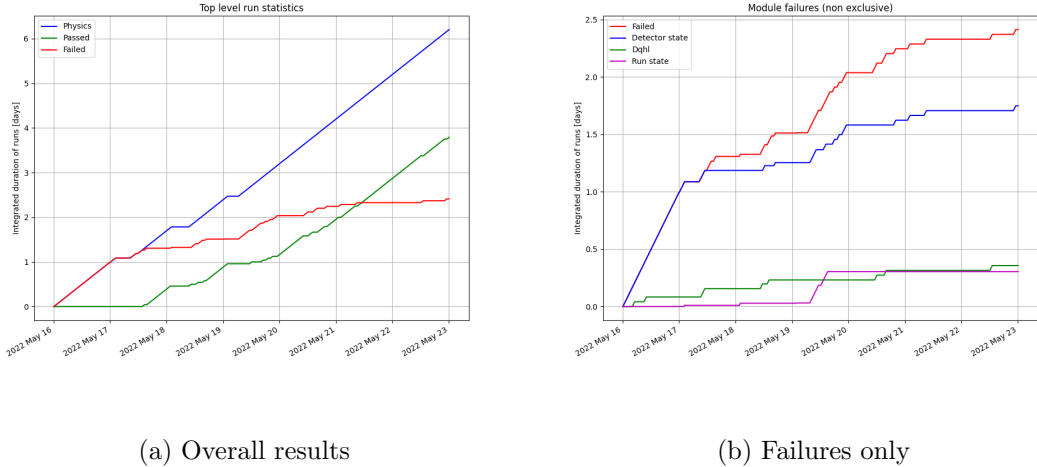


Figure B.1: The run selection results for a typical week of data collection. The failures can be broken down by module which helps inform the maintenance team of any potential issues.

Table B.2: The detector state checks.

Check	Threshold	Note
Nominal settings	32	Number of channels with incorrect trigger settings
MTC settings	True	MTC is correctly initialised
Crate settings	True	Crates are correctly initialised
Crate HV status	True	Crates are on at nominal voltage
TUBII settings	True	TUBII is correctly initialised
Blind flashers	1	Number of PMTs at nominal voltage without triggers
Missing CAEN sync	1	CAEN digitiser missing sync signal
FEC FIFO overflow	1	Data lost due to FIFO buffers becoming full
Sync 16 / Sync 24	8	Number of channels reporting sync errors
Invalid CAEN data length	1	CAEN digitiser missing data
Bad data	1	Number of FECs reporting bad data
Queue head change (MTC, CAEN, TUBII)	1	The size of the queue of events waiting to be built has had an abnormally large increase due to a problem with the MTC, CAEN or TUBII

Table B.3: The alarm checks.

Alarm	Note
Failed to read CAEN event	
CAEN event too big	
Failed to send data to builder	
XL3 crate [0-19] disconnected - LWIP error communicating with the server over TCP/IP - Bus error	Data is not being transferred correctly over the network
(Timing) Rack (1-11) voltage alarming	Each rack houses one or two crates
Cavity water temperature	
Cavity water level	
Deck temperature	
Deck humidity	
Bad data	
High rate of warnings in the builder log	5 Hz of warnings over a period of five seconds
Crate (0-18) Supply A/B - Current near zero - Ramp/Setpoint discrepancy - Over current/voltage	Crate HV has tripped off or there is a problem with the HV supply
HV panic down sent to crate (0-19)	

## Appendix C

# Reactor core information

Table C.1: Information for the reactor cores located within 1000 km of SNO+. The average power per core is calculated using the information provided by the IAEA [83].

Complex	No. of cores	Type	Distance (km)	Average design power per core (MW <sub>Th</sub> )
Bruce	8	PHWR	240.21	2673
Pickering	6	PHWR	340.36	1744
Darlington	4	PHWR	349.15	2776
Ginna	1	PWR	469.50	1775
Nine Mile Point	2	BWR	500.01	2919
Fitzpatrick	1	BWR	500.60	2536
Perry	1	BWR	519.24	3758
Fermi	1	BWR	527.36	3486
Point Beach	2	PWR	552.25	1800
Davis Besse	1	PWR	562.53	2817
Palisades	1	PWR	615.01	2565
Beaver Valley	2	PWR	652.71	2900
Cool	2	PWR	657.78	3386
Susquehanna	2	BWR	722.68	3952
Three Mile Island	1	PWR	789.61	2568
Dresden	2	BWR	799.88	2957
Byron	2	PWR	807.79	3645
Braidwood	2	PWR	809.06	3645
Indian Point	2	PWR	819.85	3216
Limerick	2	BWR	829.27	3515
Lasalle	2	BWR	834.25	3546
Peach Bottom	2	BWR	846.11	3951
Quad Cities	2	BWR	898.23	2957
Hope Creek	1	BWR	904.00	3840
Salem	2	PWR	904.44	3459
Seabrook	1	PWR	910.05	3648
Millstone	2	PWR	923.40	3175
Oyster Creek	1	BWR	931.63	1930
Clinton	1	BWR	932.84	3473
Duane Arnold	1	BWR	971.72	1912
Calvert Cliffs	2	PWR	973.79	2737
North Anna	2	PWR	974.72	2940
Pilgrim	1	BWR	984.74	2028
Monticello	1	BWR	987.48	2004

## Appendix D

# Analysis blindness

### D.1 Introduction

The blinding of data in particle physics experiments is a common technique employed in many analyses. This involves hiding some (or all) of the data while developing an analysis framework. The full data set is only revealed at the very last step. This is typically done to avoid introducing any bias into the results or tuning of the results based on the data collected.

An important point of consideration is the effectiveness of blindness in a statistically limited analysis. In the absence of a large number of events the biasing and/or tuning of results is less likely to occur since the largest uncertainties in an analysis are statistical. Additionally, it may be harder to develop analyses that have a small number of events due to difficulties in tuning MC simulations and validating predictions. This effect may be compounded if some fraction of the data is blinded.

A blinding scheme for the SNO+ antineutrino analysis is proposed to keep results unbiased and untuned while also not hiding any IBD candidate events. This is achieved by scrambling the MC prediction such that the maximum likelihood fit for the oscillation parameters is biased away from the expected result. Therefore analysers can evaluate the quality of the full data set in the early stages of an analysis. The analysis frameworks are also simplified and there is no longer a requirement of “good faith” that analysers are applying blindness conditions as agreed.

### D.2 Methodology

The blindness scheme takes advantage of the fact that the thermal power output of the nuclear reactor cores is applied as a corrective factor to the MC simulation, as described

in Chapter 6. To summarise, the MC simulation is run assuming that all reactor cores generate 120% of their specified design thermal power. The antineutrino flux originating from each reactor core is then scaled down according to the load factors provided by the IESO and IAEA for the Ontario reactors and rest of world reactors respectively. It is this scaling that is scrambled to introduce a bias into the analysis for the purpose of blindness.

The MC simulation is used to generate the predicted number of IBD events for each reactor complex. This is possible since the reactor core at which an antineutrino was created is saved in the MC truth information. The blinding scheme proceeds by scrambling the origin core for the antineutrinos created. To illustrate; an antineutrino created at Bruce could be reassigned such that it appears as though it was created at Three Mile Island. The total number of IBD events is preserved, but the number of IBD events created at individual reactor cores is not. This leads to a vastly different likelihood space that is produced when performing the oscillation parameter fit.

The effectiveness of such a blinding scheme is tested by performing the oscillation analysis on Asimov data sets generated using the PDG oscillation parameters.

### D.2.1 Removing Bruce

An initial test of the blindness scheme is to simply remove and redistribute all events from the Bruce reactor cores. Bruce contributes approximately 40% of the reactor antineutrino flux at SNO+ and therefore redistributing these events should significantly distort the likelihood space. Figure D.1 shows the fit result for Asimov data sets generated using both the PDG value and the Super-Kamiokande/SNO value for  $\Delta m_{21}^2$ . The data sets assume one year of live time in the full scintillator phase.

It is seen in Figure D.1 that the likelihood space is sufficiently biased. The best fit points for  $\Delta m_{21}^2$  are far away from the true value in both cases, while the true value is excluded at greater than  $1\sigma$  confidence. However, turning off Bruce in this way is a predictable method and it is noted that analysers could account for this in their analysis. This would remove the intended blindness from the analyses.

### D.2.2 Removing Ontario reactors

A solution to the problem posed in the end of Section D.2.1 is to extend the event distribution to include those created at the other two Ontario nuclear reactor cores: Darlington and Pickering. Additionally, not all events would be removed and redistributed. A frac-

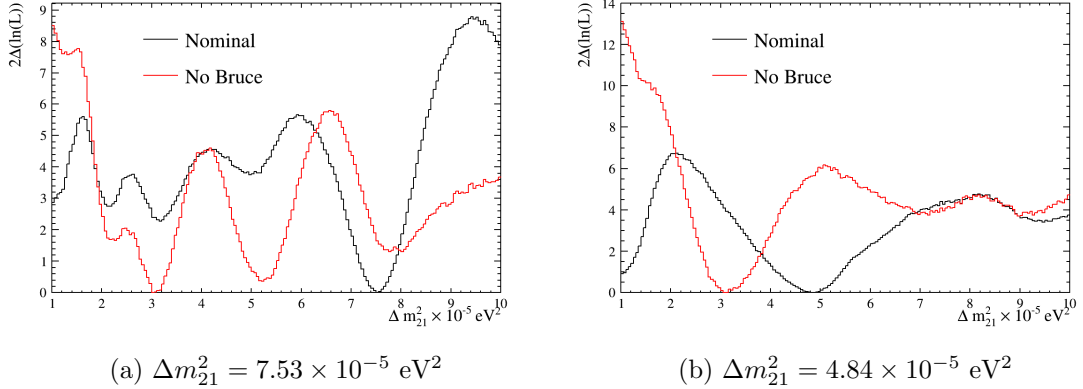


Figure D.1: The result of the oscillation fit for Asimov data sets corresponding to one year of live time. When Bruce is turned off, the "missing" events are redistributed to other reactor cores.

tion of events from the three reactor cores, unknown to analysers, would be redistributed to the rest of world reactors. This introduces an extra layer of blindness that is difficult for analysers to predict and account for in their analyses.

Figure D.2 shows the impact of selecting a different scaling factor for Bruce and for Darlington and Pickering, while keeping the other constant. Darlington and Pickering are assigned the same scaling factor as they are located approximately the same distance away from SNO+. The impact of changing the scaling factor for Darlington and Pickering significantly distorts the likelihood space and produces different minima from that of the true value. The same conclusion can be reached when varying the Bruce scaling factor, although the fraction in Figure D.2 is varied less than that of Darlington and Pickering.

### D.3 Proposal

A blinding scheme based on the results shown in Section D.2.2 is chosen. This sufficiently biases the likelihood fit results while keeping all data open to analysers. In practical terms, a member of the collaboration is nominated to select scale factors to apply to Bruce, Darlington and Pickering for the purposes of blindness. When a MC production campaign is undertaken the chosen fractions of events are redistributed from the Ontario reactors and new updated MC files generated. Analysers will then use these new MC files to create the reactor PDFs and predictions used in the oscillation analysis. To unblind the analysis, the scrambled MC files are replaced by the original MC files and the PDFs and predictions are regenerated.

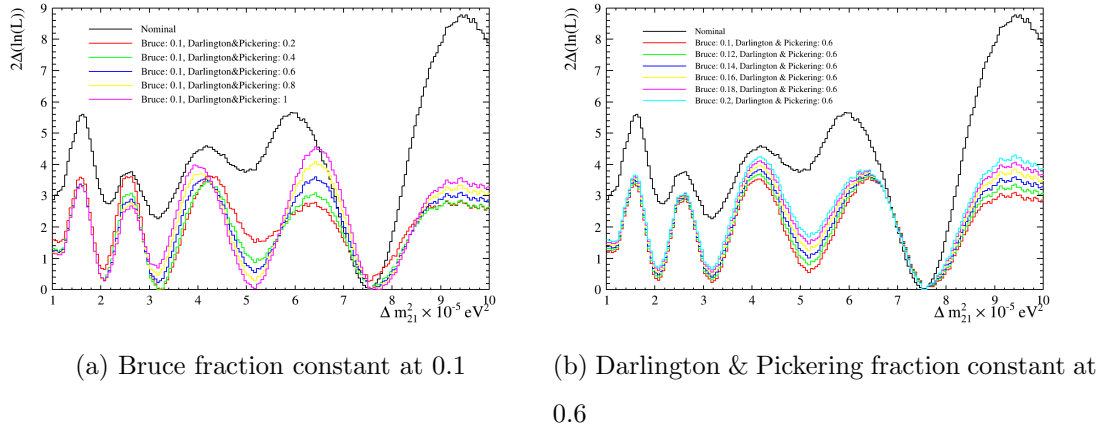


Figure D.2: The result of the oscillation fit for Asimov data sets corresponding to one year of live time in the full scintillator phase assuming  $\Delta m_{21}^2 = 7.53 \times 10^{-5} \text{ eV}^2$ . The fraction quoted in the legend is a reflection of how "on" the reactor is.